

Resilient Coordinated Control of AC Microgrids

Xiao, J.

DOI

[10.4233/uuid:e9284b2c-a65b-488e-b33b-3c23eca059e3](https://doi.org/10.4233/uuid:e9284b2c-a65b-488e-b33b-3c23eca059e3)

Publication date

2025

Document Version

Final published version

Citation (APA)

Xiao, J. (2025). *Resilient Coordinated Control of AC Microgrids*. [Dissertation (TU Delft), Delft University of Technology]. <https://doi.org/10.4233/uuid:e9284b2c-a65b-488e-b33b-3c23eca059e3>

Important note

To cite this publication, please use the final published version (if applicable). Please check the document version above.

Copyright

Other than for strictly personal use, it is not permitted to download, forward or distribute the text or part of it, without the consent of the author(s) and/or copyright holder(s), unless the work is under an open content license such as Creative Commons.

Takedown policy

Please contact us and provide details if you believe this document breaches copyrights. We will remove access to the work immediately and investigate your claim.

RESILIENT COORDINATED CONTROL OF AC MICROGRIDS

RESILIENT COORDINATED CONTROL OF AC MICROGRIDS

Dissertation

for the purpose of obtaining the degree of doctor
at Delft University of Technology,
by the authority of the Rector Magnificus prof. dr. ir. T.H.J.J van der Hagen,
chair of the Board for Doctorates,
to be defended publicly on
Monday 13 January 2025 at 10:00 o'clock

by

Junjie XIAO

Master of Science in Electrical Engineering, Xi'an Jiaotong University, China
born in Sichuan, China.

This dissertation has been approved by the promotor.

Composition of the doctoral committee:

Rector Magnificus,	chairperson
Prof. dr. ir. P. Bauer,	Delft University of Technology, promotor
Dr. Z. Qin,	Delft University of Technology, promotor

Independent members:

Dr. L.M. Ramirez Elizondo,	Delft University of Technology
Prof. dr. ir. M. Popov,	Delft University of Technology
Prof. dr. ir. Z. Lukszo,	Delft University of Technology
Dr. A.I. Stefanov,	Delft University of Technology
Prof. dr. T. Dragicevic,	Technical University of Denmark



An electronic version of this dissertation is available at
<http://repository.tudelft.nl/>.

Copyright © 2025 by Junjie Xiao

CONTENTS

Summary	vii
Samenvatting	ix
1 Introduction	1
1.1 Background and Motivation	1
1.2 Thesis Objective and Research Questions.	3
1.3 Major Contributions	5
1.4 Outline of the Thesis	5
2 Resilience Enhanced Secondary Frequency Control	7
2.1 Introduction	8
2.2 Cooperative Secondary Control Strategy in Microgrid	10
2.2.1 Communication Network Configure	10
2.2.2 Primary Droop Control.	10
2.2.3 Distributed Secondary Control	11
2.3 Cyber Attack on DSC	12
2.3.1 Modeling of the Cyber Attack	12
2.3.2 Control Problem Statement.	13
2.4 Proposed Control and Stability Analysis	14
2.5 Experimental Verification	17
2.6 Conclusion.	21
3 Distributed Control for Power Regulation with Low Vulnerability	23
3.1 Introduction	24
3.2 Island Microgrid Analysis	27
3.2.1 Primary Droop Control.	27
3.2.2 Reactive Power Sharing Analysis under IDF	28
3.2.3 Active Power Sharing Analysis under RDF	29
3.2.4 Harmonic Power Analysis	29
3.2.5 Bus Voltage Compensation Analysis	30
3.2.6 Harmonic Extract and Power Calculation	31
3.3 The Resilient PI-consensus Law for Power Regulation	31
3.3.1 Distributed Virtual Impedance under Inductive Feeder	31
3.3.2 Distributed Virtual Impedance under Resistive Feeder	36
3.4 The Distributed Model Predictive Control	39
3.4.1 Power Transfer Equations	40
3.4.2 Discrete Time Models	41
3.4.3 State Observer	41
3.4.4 Cost Function	42

3.4.5	Relief to Communication Issues	42
3.5	Experiment results	44
3.5.1	The Proposed DVI under IDF Verification	45
3.5.2	The Proposed DVI under RDF Verification	49
3.5.3	The Proposed DMPC-based Virtual Impedance Verification	53
3.6	Conclusion.	58
4	Multi-VSGs Grid: Active Power Oscillation in Circuit Perspective	61
4.1	Introduction	62
4.2	VSG Oscillation Analysis.	64
4.2.1	Review on Traditional Droop and VSG Control.	65
4.2.2	Active Power Oscillation with VSG control.	67
4.3	Equivalent Impedance Circuit of VSG	69
4.3.1	Single-VSG Equivalent	69
4.3.2	Multi-VSG Equivalent	71
4.4	Proposed Control Design.	73
4.4.1	Power Oscillation Mitigation in SA Mode	73
4.4.2	Power Oscillation Mitigation in GC model	74
4.5	Verification.	75
4.5.1	Simulation Result	75
4.5.2	Experiment Result	77
4.6	Conclusion.	79
5	Resilience-Oriented Communication Network Design	81
5.1	Introduction	82
5.2	Distributed Secondary Control in Microgrid	85
5.3	Communication Network Design.	85
5.3.1	Convergence Performance	86
5.3.2	Robustness to Communication Delay.	87
5.3.3	Communication Cost.	87
5.3.4	Invulnerability Design of Communication Network	88
5.3.5	Optimal Communication Graph Design	91
5.4	Verification.	92
5.5	Conclusion.	98
6	Conclusion	99
	Bibliography	103
	List of Publications	115
	Acknowledgments	117

SUMMARY

The integration of renewable energy resources has seen a marked increase in recent decades, driven by the need to address the growing severity of the global energy crisis. Distributed generators, which incorporate renewable energy sources alongside energy storage systems, present a viable pathway toward achieving substantial economic and environmental benefits.

In the context of microgrids, maintaining frequency and voltage amplitude within prescribed limits is essential for stable operation. Furthermore, the proper distribution of power—including active, reactive, and harmonic components—among interconnected converters is critical to achieving balanced performance under steady-state conditions. During dynamic transitions, it is equally important for voltage and power levels to evolve smoothly, ensuring a seamless adjustment to the steady-state operating point.

VOLTAGE FREQUENCY AND AMPLITUDE RESTORATION

Droop control provides voltage support when the microgrid operates in stand-alone mode. However, it can lead to deviations in frequency and voltage amplitude.

Secondary control restores the state of islanded AC microgrids to their set points. This thesis proposes a graph theory-based secondary control approach for frequency and voltage recovery. This method does not require prior knowledge of the microgrid, such as control parameter values and line parameters. Instead, each converter adjusts its state based on information from its neighbors. By treating each converter as an autonomous node and leveraging communication technology, all nodes involved can reach a consensus, regardless of differences in their initial states.

STEADY-STATE POWER AND AC BUS VOLTAGE REGULATION

The key performance indicators of microgrids include proportional power sharing and AC bus voltage. Due to mismatched feeder impedances in AC microgrids, it is challenging to accurately share active, reactive, and harmonic power while maintaining AC bus voltage quality. Frequency and voltage amplitude compensation can achieve power-sharing goals; however, this method requires continuous communication, increasing the communication burden. Inserting sizeable virtual impedance offers another approach to compensating for feeder impedance differences. Nevertheless, it results in a significant voltage drop, which degrades AC bus voltage quality. Due to the conflicts between these performance indicators, it is essential to consider both in the design of distributed controllers.

This thesis proposes a virtual impedance method based on graph theory to address the challenges of power sharing and voltage quality. The proposed approach regulates both fundamental and harmonic impedance to desired values by exchanging information with neighboring inverters. Additionally, a distributed model predictive control-based virtual impedance is investigated, offering improved dynamic performance. Furthermore,

the influence of different feeder characteristics is analyzed, as these significantly impact controller design.

This distributed approach eliminates the need for a central controller and reduces the communication burden. Experimental results validate the effectiveness of the proposed method in improving both power sharing and voltage quality.

DYNAMIC POWER CONTROL

The transition from droop control to VSG control can introduce oscillatory dynamics that complicate the system, potentially leading to significant frequency and active power oscillations during the dynamic process. These oscillations occur in grid-connected mode and when multiple VSGs operate in stand-alone mode. The large instantaneous currents associated with these oscillations can trigger overcurrent protection mechanisms, exacerbating system stability issues. Consequently, the design of active power dynamics must be approached with caution. In the stand-alone mode, the interaction among the involved converters causes oscillation because of the difference between the VSG's control parameter and feeder impedance. When connected to the utility grid, the output active power should accurately track the power reference. Therefore, the VSG can be modeled as a second-order system to explain the oscillations in grid-connected mode.

This thesis proposes the equivalent circuit models of a converter with VSG control in both modes, which intuitively reveals the root cause of active power oscillations. Accordingly, a distributed virtual impedance is introduced to harmonize parameters among involved VSGs, eliminating oscillations in stand-alone mode. As for the grid-connected mode, the active power oscillations are attenuated through the proposed adaptive inertial coefficient, which is dynamically tuned via a feed-forward loop. Simulation and experimental results verify the improvements of the proposed control.

CYBER ATTACK DEFENSE

Communication-based distributed secondary control is widely used to achieve consensus in stand-alone AC microgrids. However, these microgrids become susceptible to cyber-attacks with limited global information. These attacks compromise the confidentiality, integrity, and availability of information within the microgrid, disrupt control objectives, and destabilize the system.

In this thesis, the resilient algorithms are investigated to counter these threats. One approach involves blocking corrupted signals to prevent false data from affecting the entire system, though this may degrade convergence. Another method reconstructs the attacked signal from normal data, limiting the impact on infected units. Additionally, optimally weighting the signal ensures that corrupted signals are exponentially attenuated when they deviate from the norm, even under multiple attacks. Experimental results demonstrate that these resilience strategies do not adversely affect normal microgrids. Moreover, the communication network design for secure microgrid operation is studied. This approach involves designing the communication network to enhance security before attacks occur, while the existing network design ignores it. New metrics are introduced to quantify the impact of various cyber-attacks effectively. It then employs a multiobjective optimization method to design the communication network, considering the quantified attack impacts, convergence, time-delay robustness, and communication costs.

SAMENVATTING

De penetratie van hernieuwbare energiebronnen is de afgelopen decennia aanzienlijk toegenomen om de toenemende ernst van de energiecrisis aan te pakken. Gedistribueerde generatoren, waarin hernieuwbare energiebronnen en energieopslagsystemen worden geïntegreerd, bieden veelbelovende economische en milieutechnische voordelen.

In microgrids moeten frequentie en spanningsamplitude binnen specifieke grenzen blijven. Daarnaast moeten het actieve, reactieve en harmonische vermogen in de stationaire toestand proportioneel worden verdeeld over de betrokken omvormers. Tijdens dynamische aanpassingen wordt verwacht dat zowel de spanning als het vermogen geleidelijk naar een stabiele toestand evolueren.

HERSTEL VAN FREQUENTIE EN SPANNINGSAMPLITUDE

Droop-regeling biedt spanningsondersteuning wanneer de microgrid in een stand-alone modus werkt, maar kan leiden tot afwijkingen in frequentie en spanningsamplitude. Om de toestand van eilandbedrijf-microgrids terug te brengen naar de ingestelde waarden, is secundaire controle nodig. In dit onderzoek wordt een op grafentheorie gebaseerde secundaire regeling voorgesteld om frequentie en spanning te herstellen. Deze aanpak vereist geen voorkennis van de ontwerpdetails van de omvormers, zoals de waarden van de regelparameters of lijnimpedanties. Elke omvormer past zijn toestand aan op basis van informatie van naburige eenheden. Door elke omvormer te beschouwen als een autonoom knooppunt en communicatietechnologie in te zetten, kunnen alle knooppunten een consensus bereiken, ongeacht de initiële toestand. Voor nauwkeurige regelbeslissingen moet de secundaire lus worden ontworpen met inachtneming van de bandbreedte van de primaire lus. Dit garandeert dat frequentie en spanning effectief worden hersteld.

REGELING VAN VERMOGEN EN AC BUS-SPANNING IN STATIONAIRE TOESTAND

Belangrijke prestatie-indicatoren van microgrids zijn onder andere proportionele vermogensdeling en de kwaliteit van de spanning op het AC bus-voltage. Door ongelijke lijnimpedanties in AC-microgrids is het lastig om actief, reactief en harmonisch vermogen nauwkeurig te verdelen en tegelijkertijd de AC bus-spanningskwaliteit te behouden. Frequentie- en spanningsamplitudcompensatie kan helpen bij het bereiken van een evenwichtige vermogensverdeling, maar dit vereist continue communicatie, wat de communicatielast vergroot. Virtuele impedantie biedt een alternatieve oplossing, maar veroorzaakt een significante spanningsval die de AC bus-spanning kan aantasten. Daarom is het essentieel om deze prestatie-indicatoren in een gedistribueerde regelaar in balans te brengen.

In dit onderzoek wordt een op gedistribueerde filosofie gebaseerde virtuele impedantie voorgesteld om de problemen rond vermogensdeling en spanningskwaliteit op te lossen. De methode reguleert de fundamentele en harmonische impedantie door informatie uit

te wisselen met naburige omvormers. Daarnaast wordt een op modelpredictieve controle gebaseerde virtuele impedantie onderzocht, wat zorgt voor betere dynamische prestaties. De verschillende karakteristieken van lijnimpedanties worden bestudeerd, omdat deze een grote invloed hebben op het ontwerp van de regelaar. Deze gedistribueerde aanpak maakt een centrale regelaar overbodig en vermindert de communicatielast. Experimentele resultaten bevestigen de effectiviteit van de voorgestelde methode.

DYNAMISCHE VERMOGENSREGELING

De overgang van droop-regeling naar VSG kan oscillaties introduceren, wat kan leiden tot aanzienlijke frequentie- en vermogensschommelingen tijdens dynamische processen. Dergelijke oscillaties treden zowel op in netgekoppelde modus als wanneer meerdere VSG's in eilandbedrijf werken. Hoge piekstromen als gevolg van deze oscillaties kunnen overbelastingsbeveiligingen activeren, waardoor de systeemstabiliteit verder wordt aangetast. Voorzichtigheid is daarom geboden bij het ontwerpen van de dynamiek van actief vermogen.

In eilandbedrijf veroorzaken interacties tussen omvormers oscillaties door verschillen in de VSG-regelparameters en lijnimpedanties. In netgekoppelde modus moet het uitgangsvermogen nauwkeurig de referentiewaarde volgen. Dit onderzoek introduceert equivalente schakelingen van omvormers met VSG-regeling, die de oorzaken van actieve vermogensoscillaties verduidelijken. Voor eilandbedrijf wordt een gedistribueerde virtuele impedantie voorgesteld om parameters te harmoniseren en oscillaties te elimineren. In netgekoppelde modus wordt een adaptieve inertiecoëfficiënt gebruikt, die dynamisch wordt aangepast via een feedforward-lus om schommelingen te dempen. Simulaties en experimenten tonen aan dat de voorgestelde regelingen effectief zijn.

WEERBAARHEID TEGEN CYBERAANVALLEN

Gedistribueerde secundaire regeling, die op communicatie gebaseerd is, wordt vaak gebruikt in eilandbedrijf-AC-microgrids om consensus te bereiken. Deze microgrids zijn echter kwetsbaar voor cyberaanvallen, wat de betrouwbaarheid, integriteit en beschikbaarheid van informatie kan schaden en de controle- en stabiliteitsdoelen in gevaar brengt.

Dit onderzoek onderzoekt weerbare algoritmen tegen dergelijke bedreigingen. Eén aanpak blokkeert corrupte signalen, wat voorkomt dat foutieve data het systeem beïnvloeden, maar dit kan de convergentie vertragen. Een andere methode reconstrueert aangetaste signalen op basis van normale data, zodat de impact op geïnfecteerde eenheden beperkt blijft. Daarnaast worden geoptimaliseerde gewichten toegepast om afwijkende signalen exponentieel te verzwakken, zelfs bij meerdere aanvallen. Experimentele resultaten tonen aan dat deze strategieën geen negatieve effecten hebben op normale microgrids. Bovendien wordt een ontwerp voor communicatie-infrastructuur voorgesteld dat de veiligheid van microgrids verbetert vóórdat aanvallen plaatsvinden. Hierbij worden nieuwe maatstaven geïntroduceerd om de impact van cyberaanvallen te kwantificeren. Deze aanpak gebruikt een multi-objectieve optimalisatie om het netwerk te ontwerpen met aandacht voor de gequantificeerde effecten van aanvallen, robuustheid bij vertragen en communicatiekosten.

1

INTRODUCTION

1.1 BACKGROUND AND MOTIVATION

Global sustainability is confronted with significant challenges that threaten the long-term health of our planet, its ecosystems, and its inhabitants [1]. Climate change, primarily driven by greenhouse gas emissions, stands out as one of the most pressing issues. It results in extreme weather events, rising sea levels, ocean acidification, and severe disruptions to ecosystems and agriculture [2]. Furthermore, the over-exploitation of natural resources—including fossil fuels, minerals, water, and arable land—exacerbates these challenges. Unsustainable practices in resource extraction and consumption not only contribute to resource scarcity but also place additional stress on our environmental systems.

Microgrids (MGs) facilitate the integration of renewable energy sources such as solar, wind, and hydropower into the energy mix, where the communication technology is usually adopted for coordination, as shown in Fig.1.1. In the event of a power shortage in the main grid, these renewable energy sources can supply power to the main grid through the feeder. Managing distributed energy resources within microgrids provides a flexible platform to address the variability inherent in renewable energy generation [3]. Additionally, by incorporating energy storage systems, microgrids can store excess renewable energy for later use, reducing dependence on fossil fuels and promoting the transition to a low-carbon future.

Microgrids are self-sufficient electrical systems that generate, store, and distribute electricity to serve localized communities. They can support the utility grid during peak demand periods and are especially useful in remote regions where the primary power grid may be absent or unreliable, allowing for the import or export of electricity as required. In developing nations, microgrids provide a cost-effective and sustainable energy solution for communities lacking access to reliable electricity.

Moreover, microgrids enhance energy independence and resilience by reducing the risk of power outages and disruptions that affect centralized energy systems. Central power grids are often severely impacted by natural disasters such as hurricanes, earthquakes, and floods, leading to extended outages and significant damage to essential infrastructure. In a major blackout, microgrids can automatically detach from the main grid and operate independently, utilizing distributed energy resources (DERs) to generate, store, and distribute

electricity locally [4]. This functionality ensures that critical facilities, including hospitals, data centers, and emergency response centers, continue to receive power [5].

In summary, the microgrid system offers several advantages over traditional power systems:

- **Enhanced reliability:** Microgrids can function autonomously, ensuring power supply even if the main grid experiences failures.
- **Lower energy costs:** Microgrids can decrease energy expenses and boost efficiency by integrating renewable energy sources and energy storage.
- **Greater energy security:** Microgrids offer a dependable power supply in regions where the main grid is either unreliable or costly.
- **Environmental advantages:** Using renewable energy sources in microgrids helps lower carbon emissions, contributing to climate change mitigation.
- **Increased flexibility:** Microgrids can be tailored to address the unique needs of local communities and can be expanded or adjusted as required.
- **EV integration:** Microgrids can support electric vehicle (EV) charging stations with a localized and flexible power supply, alleviating pressure on the main grid and enhancing the efficiency of the charging process.

When a microgrid is connected to the main grid, the main grid controls the microgrid's frequency and voltage, while the power supplied to the grid is regulated by a power reference. However, when the microgrid operates independently from the utility grid, it is the responsibility of distributed generators (DGs) to maintain the frequency and voltage. This process is heavily reliant on the coordination among the DG converter interfaces. Because power electronics-based DGs have low inertia, maintaining control accuracy and system stability in an isolated microgrid becomes more complex and challenging.

Effective control is critical to ensure the reliable operation of a microgrid where several key challenges exist:

1. **Cybersecurity Risks:** As the deployment of microgrids becomes more prevalent, the potential for cyber-attacks poses a growing threat to their availability, integrity, and confidentiality. Notable incidents, such as the 2003 cyber-attack on the Davis-Besse nuclear plant in Ohio, USA [6], and the 2016 attack on Ukraine's power system [7], highlight the critical vulnerabilities in power systems. These examples underscore the urgent need for developers to adopt approaches to enhance cyber security in the design and operation of microgrid systems.
2. **Energy Storage Challenges:** While battery storage is becoming more cost-effective and reliable, it remains a significant upfront cost for many microgrid projects. Improper power distribution can overload small-capacity inverters, potentially leading to reduced equipment life.
3. **Harmonics and Power Quality:** Harmonics are high-frequency distortions in voltage and current that can occur in electrical systems due to non-linear loads such as

electronic devices and power electronic converters. These distortions can cause problems such as power loss, increased equipment heating, and reduced power factor.

4. **Microgrid Stability:** The stability of a microgrid is its ability to return to normal operation after a disturbance. There are two types of stability to consider: steady-state and dynamic. Steady-state stability involves maintaining voltage and frequency within acceptable limits under both normal and abnormal conditions. Renewable energy sources, such as photovoltaic systems and wind turbines, are particularly sensitive to weather variations, which can result in unstable power generation. In addition, the load profile can vary due to the varying number of users. Dynamic stability refers to the ability of the system to return to a steady state after disturbances such as changes in load or generation. Unlike conventional synchronous generators, which provide substantial inertia to stabilize large power systems, microgrids often rely on power converter-interfaced distributed generation, which has low inertia. This low-inertia characteristic can lead to challenges with frequency stability, making dynamic frequency stability a critical concern for microgrid operation.

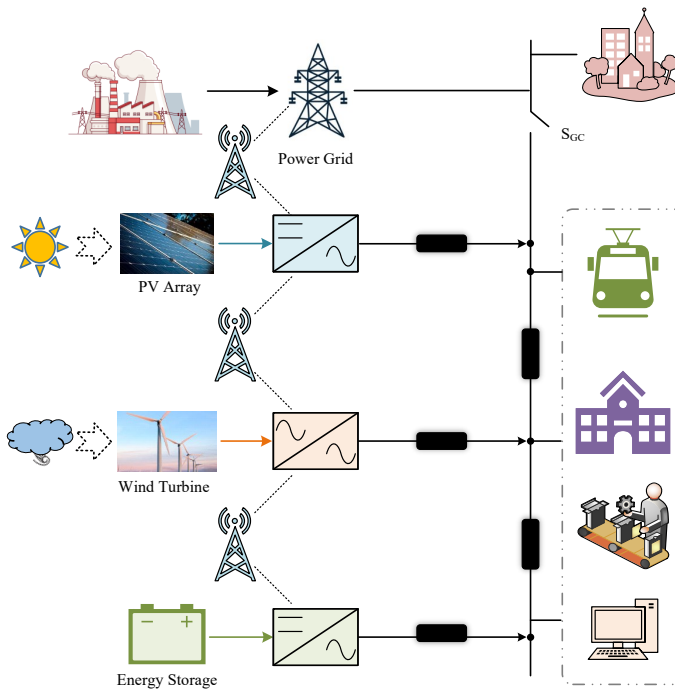


Figure 1.1: A typical power system includes renewable energy and energy storage.

1.2 THESIS OBJECTIVE AND RESEARCH QUESTIONS

As indicated previously, the research objective of this thesis is as follows.

"Addressing the voltage and power regulation issues in microgrids while considering various communication challenges."

To reach the objective leads to several research questions, which are as follows:

Q1 *What are the key design and implementation strategies for distributed secondary control to achieve effective frequency and voltage restoration in microgrids?*

- Investigate the necessity of the secondary control.
- Review and compare recent advancements in secondary control strategies, focusing on their efficacy and robustness.
- Design and implement the distributed secondary control in the microgrids.
- Stability and limitation analysis.
- Validate the proposed secondary control by experiment.

Q2 *How to achieve power-sharing without degrading the AC bus voltage quality in the absence of prior system knowledge?*

- Comprehensive literature review of existing power regulation methods to understand the current approaches and their limitations.
- Analyze the underlying causes of inadequate power sharing, focusing on factors that may lead to both poor distribution and compromised voltage quality.
- Identify and resolve the contradictions between achieving effective power-sharing and maintaining high voltage quality. Develop new methods that balance these conflicting requirements.
- Examine the characteristics of various feeder types and determine how to apply the proposed method in different scenarios.
- Perform experimental validation to assess the efficacy of the proposed method.

Q3 *How to enhance the resilience of secondary control of microgrids against cyber attacks?*

- Review existing methods for defending against cyber attacks.
- Develop models of the cyber-attacks and identify how they hack the microgrid
- Analyze the impact of cyber attacks on stability.
- Design resilient algorithms to be integrated into secondary control systems to enhance the microgrid's resistance to cyber threats.
- Validate the effectiveness of the proposed resilient methods through experimental testing.

Q4 *How can oscillations be dampened for multiple virtual synchronous generators?*

- Review and evaluate existing methods for analyzing and mitigating power oscillations in multi-VSG systems.
- Develop a new circuit model to reassess oscillation behavior and dynamics.
- Design novel strategies to suppress oscillations effectively.
- Test and validate the proposed methods through experimental evaluation.

Q5 *How to optimize the communication network for distributed control?*

- Survey current communication network designs used for coordinating microgrid operations.
- Analyze the advantages and disadvantages of various network design methods.
- Develop an optimization algorithm for designing communication networks that consider cyberattack resilience.
- Evaluate the effectiveness of the proposed communication graph optimization algorithm in improving the dynamic and stable requirements.

1.3 MAJOR CONTRIBUTIONS

As indicated previously, the major contribution of this thesis is as follows.

Targeting to give answers to the aforementioned research questions, the thesis has the contributions as follows.

- A resilience-enhanced distributed secondary frequency control is proposed for AC microgrids, considering communication disturbances and cyber attacks (Chapter 2).
- Distributed strategies for accurate power regulation in various microgrid structures without relying on feeder impedance are investigated while improving the quality of the AC bus voltage (Chapter 3).
- The dynamic active power oscillation is studied, and the oscillation is an analogy to an impedance circuit for clear physical interpretation (Chapter 4).
- An optimization method is proposed for designing the communication network used for distributed control, considering control objectives and vulnerabilities to communication issues (Chapter 5).

1.4 OUTLINE OF THE THESIS

The thesis outline is presented in Fig.1.2.

Chapter 1 introduces the evolution of distributed generation and microgrid technologies, highlighting the critical role of inverter control in enabling efficient microgrid operation. This chapter also outlines the research objectives, major contributions, and the overall structure of the thesis.

Chapter 2 delves into the challenges of frequency restoration in microgrids. It begins by introducing a graph-theory-based distributed secondary control framework for restoring voltage frequency and amplitude. The chapter addresses vulnerabilities to cyber-attacks in microgrid control systems and proposes a resilient secondary control strategy to mitigate these threats. The proposed methodology is validated through simulations and experimental results, demonstrating its robustness and effectiveness.

Chapter 3 examines the complexities of active, reactive, and harmonic power sharing under mismatched impedance conditions while ensuring the PCC voltage quality. Additionally, this chapter includes discussions on PI-consensus and DMPC-consensus-based virtual impedance strategies.

Chapter 4 provides a detailed analysis of active power oscillations in virtual synchronous generator-based microgrids. An impedance circuit model is proposed to investigate the underlying mechanisms of these oscillations. Building on this model, the chapter focuses on mitigating dynamic power oscillations in multi-VSG systems through novel control strategies. Additionally, it delves into the interactions among distributed generators, highlighting how their differing properties influence system dynamics.

Chapter 5 focuses on the optimization of communication networks for distributed control in microgrids. It considers the impact of cyber-attacks, convergence rates, time-delay robustness, and communication costs. Building on the communication-based control approaches from previous chapters, this chapter proposes strategies to enhance cyber security and operational efficiency.

Chapter 6 concludes the thesis by summarizing the key findings and contributions and answering the research questions.

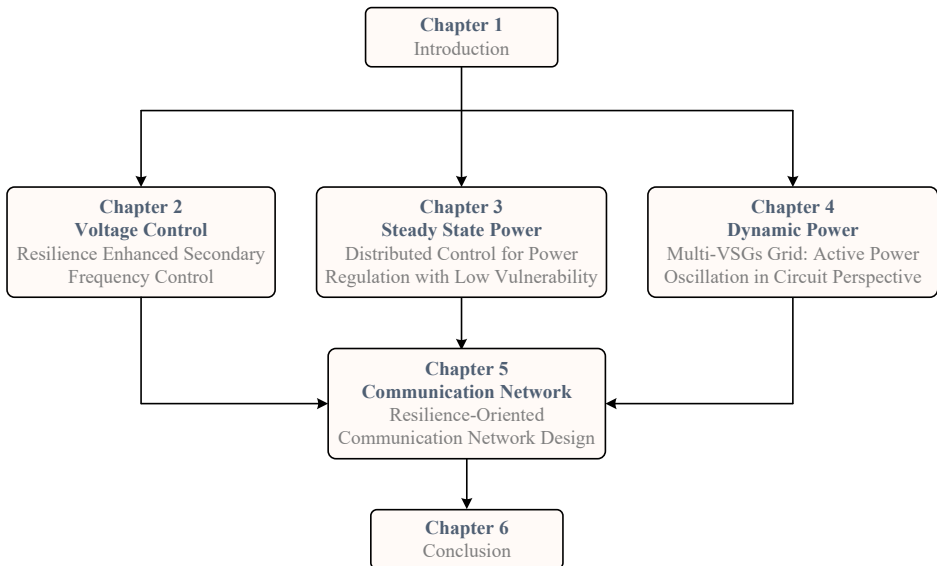


Figure 1.2: Outline of the thesis.

2

RESILIENCE ENHANCED SECONDARY FREQUENCY CONTROL

Communication-based distributed secondary control is deemed necessary to restore the state of islanding AC microgrids to set points. As it limited global information, the microgrids become vulnerable to cyber-attacks, which, by falsifying the communicating signals, like the angular frequency, can disturb the power dispatch in the microgrids or even induce blackout by pushing the microgrids beyond the safe operation area and trigger the protection. To make the microgrids more cyber secure, adaptive, resilient control for the secondary frequency regulation is proposed. It assumes that each converter is communicating with its adjacent converters. With the proposed control, the weight of the communication channel being attacked is automatically reduced, and the more the communicating signals are falsified, the further the weight of that communication channel is weakened. Besides, it still works when challenged by a combination of multi-attack signals. Moreover, it applies to multiple communication lines getting attacked cases. Finally, the effectiveness and feasibility of the proposed resilient control scheme are validated by both simulations and experimental results.

This chapter is based on:

-J. Xiao, L. Wang, Z. Qin and P. Bauer, "A Resilience Enhanced Secondary Control for AC Micro-Grids," IEEE Transactions on Smart Grid, vol. 15, no. 1, pp. 810-820, 2024.

2.1 INTRODUCTION

In microgrid control, the droop law is typically used for power regulation. However, it may cause frequency and voltage amplitude to deviate from their nominal values. To address this issue, the secondary control is introduced to restore the voltage. Moreover, the distributed secondary control (DSC) is gaining popularity for higher precision, with the set point of a converter based on information from neighboring converters to regulate the voltage. By avoiding a centralized secondary control, the AC microgrid is immune to single-point failures in the controller [8]. However, limited global information makes it vulnerable to cyber attacks, which may affect control accuracy and system stability [9].

Among different kinds of cyber attacks, false data injection attacks (FDIAs) [10] and denial of service (DoS) attacks [11] are the two most widely discussed cyber-attacks relevant to microgrids. These attacks jeopardize the confidentiality, integrity, and availability of information in the microgrid, disrupt control objectives, and deserve attention. Moreover, a series of recent cyber attack security incidents have demonstrated that the existing technology is insufficient to defend against hackers' elaborate virus data [12]. A review of the previous work suggests that the responses to cyber attacks fall into three types of mechanisms [13]: a) prevention, to avoid directing cyber attacks onto the system; b) resilience, to endure the most significant of an attack and to operate as close to normality as possible, and c) attack detection and isolation, recognize the target of the attack, isolate the damaged subsystem, and recover the usual pattern as efficiently as possible.

In reality, it is impossible to establish a communication infrastructure that avoids all cyber attacks. Therefore, the microgrid must possess resilience to operate under cyber-attacks and mitigate their impact. Once the microgrid gets attacked, the attack will be detected and classified, and then the resilient scheme should be employed to make the system survive. Then, the controller should isolate the severely infected unit immediately to protect the overall system. Therefore, to meet data privacy demands and microgrid stability, cyber security deserves additional investigation [14].

A resilience-enhanced controller equipped with a detector is a traditional way to mitigate cyber-attacks. Different cyber-attack detection methods can be broadly classified into two types. Model-based methods, like the Kalman filter-based detector in [15] and [16], serve to identify FDIA in power systems. Nevertheless, a well-designed cyber attack with in-depth knowledge of the system is likely to hinder state estimation [17]. In [18], sliding mode control compensates for the attack signal and removes adverse effects. However, the attack signal reconstruction results in a slower controller response. Moreover, this model-based method relies on the systematic model's correctness, making it less effective in practical implementations because of its inevitable mismatch with complicated real-world power electronic systems. In addition, some kinds of intelligent attacks can evade detection by traditional methods, which are pretty challenging to diagnose [19]. Model-free approaches such as AI-based algorithms [20] have also been proven to be prospective methods for cyber-attack detection. However, it increases the computational burden [21]. Obviously, these detection schemes impose an additional computational burden on the participating units. Inevitably, the dependence on these sophisticated detection algorithms causes the controller to respond slowly to attacks, which is not applicable under demanding case [22],[23].

A further problem concerns the current work focusing on resilient control-related

projects in microgrid systems, mainly considering only a single attack. For example, the stability conditions of microgrids under DoS attacks have been studied in some detail [24], [25]. Nonetheless, it is also indispensable to consider a combination of DoS and FDIA owing to the different features of various attacks. Besides, in [26],[27], an adaptive law-based approach is presented to promote microgrid resilience by adaptively modifying the consensus gain among the related agents. In [28], the information picked up from the attacked unit is dropped by turning off the corresponding network link as a basic method to avoid spreading attacks to the local controller. However, directly dropping the information the communication network propagates will disrupt the convergence theories.

Another pending issue is that applied resilient schemes restrict the number of infected agencies. To increase the resilience of the microgrid, an event-trigger resilient control is proposed [29]. The rationale behind such an approach is that a carefully designed event triggers judges' decision to perform a defense mechanism. The corrupted data is reconstructed from the healthy channel data, and intuitively, this method fails when all channels are under attack. In [30], the defense mechanism will not work if over half of the units are under attack. The mitigation scheme proposed in [31] ensures that the grid system remains operational when $n-1$ out of n units are attacked in a system. This framework generally limits its ability to be resilient to worst-case attacks.

From the above literature review, four significant research gaps of interest can be summarized as follows. (1) The reliance on attack detectors slows down the suppression of attack vectors by controllers [15],[18],[20]; (2) Insufficient research on the combination of cyber attacks [24], [25]; (3) Blocking attacked channels disrupts the convergence law [26], [27], [28]; (4) The resilience method limits the number of infected units [29], [30], [31].

Motivated by the above gaps, this chapter proposes an adaptive control method that achieves resilience to implement output voltage restorations and output power sharing of inverters in AC microgrids. The contributions of this chapter are listed as follows: 1) The method proposed in this chapter is not dependent on detecting cyber-attacks and, therefore, responds fast to attack signals; 2) Two types of attacks and their combination are formulated, and their impacts on MG system performance are demonstrated. In the presence of these attacks, the proposed mechanism can quickly restore optimal operational objectives (i.e., proportional active power sharing and frequency restoration); 3) The proposed method dispatches a relatively healthy communication line for propagating information. Thus, it will not stop convergence law in the communication network; 4) The proposed method will not limit the number of attacked units. It still works when all channels are attacked; 5) The proposed defense strategy provides timely mitigation for corrupted participants in a distributed manner without impeding the regular operation of the microgrid, and Lyapunov Criteria verify its stability. The adaptability of the proposed control strategy is also tested in various attacks, including load variations.

The chapter is structured as follows: Section 2.2 introduces the microgrid structure and the implementation of distributed secondary control. Section 2.3 examines the impact of cyber attacks on the performance of the DSC. Section 2.4 presents the proposed resilience enhancements to mitigate the effects of cyber attacks. Section 2.5 verifies the effectiveness of the proposed methods through experimentation. Finally, Section 2.6 concludes the chapter.

2.2 COOPERATIVE SECONDARY CONTROL STRATEGY IN MICROGRID

The typical micro-grid can be reconsidered as shown in Fig.2.1, where the inverter can be modeled as a voltage in series with an output impedance $Z_{o,i}$ and feeder impedance $Z_{L,i}$ of i -th inverter. A sparse communication network connecting different agencies propagates reference information to share the state of each inverter unit. The controller's significant goals are voltage regulation and proportional power-sharing, while the object of the communication control is to realize the optimal operation.

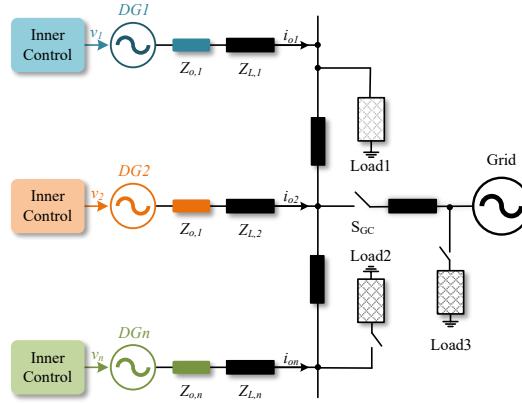


Figure 2.1: A typical microgrid configuration consisting of n DGs.

2.2.1 COMMUNICATION NETWORK CONFIGURE

The research object in this chapter is a microgrid system with n inverters operating in islanded operation mode, which regulates the frequency and amplitude of the voltage to maintain the power balance.

An undirected cyber graph of the communication network is considered to show how the involved converters share data with their neighbors. For the i -th converter in the microgrid, the communication graph with j -th converters can be written as an undirected via edges and links via communication adjacency matrix $A = (a_{ij})_{n \times n}$. The communication weight $a_{ij} = 1$ if the i th unit and the j th unit are in regular communication; otherwise, $a_{ij} = 0$. The degree of vertex ζ_i is given as $d_i = \sum_{j=1}^n a_{ij}$. $D = \text{diag}(d_1, \dots, d_n)$ is the corresponding degree matrix. Further, the Laplacian matrix L of the communication network L is defined as $L = D - A$.

With the sparse communication network outlined above, distributed generation units can communicate with each other to propagate reference information.

2.2.2 PRIMARY DROOP CONTROL

Droop control is a widely used primary control strategy for islanded AC microgrids for power sharing and keeping the voltage at an accepted range. Here, we investigate the output angular frequency ω_i , filter voltage amplitude V_i , inverter output active power

P_i , and reactive power Q_i . With the traditional droop control in [32] under inductive feeder, proportional active power sharing can be achieved. The P - ω and Q - V droop control mechanism can be written as (2.1) and (2.2):

$$\omega_i = \omega_0 + m_i(P_{ri} - P_i) \quad (2.1)$$

$$V_i = V_0 + n_i(Q_{ri} - Q_i) \quad (2.2)$$

where the m_i and n_i are droop coefficients for active power and reactive power loop, respectively, determined by the maximum output capacity of the inverter. ω_0 and V_0 are the nominal frequency and voltage set points. P_{ri} and Q_{ri} denote the reference for the active and reactive power controllers, respectively.

Notably, the active and reactive power are expected to be proportionally shared in the steady state according to their droop coefficient ratio. At the same time, the voltage and frequency are restored to the nominal value. The control objective for the microgrid can be represented as follows:

$$\lim_{t \rightarrow \infty} \omega_i(t) = \omega_0; \lim_{t \rightarrow \infty} m_i P_i(t) = \lim_{t \rightarrow \infty} m_j P_j(t) \quad (2.3)$$

$$\lim_{t \rightarrow \infty} V_i(t) = V_0; \lim_{t \rightarrow \infty} n_i Q_i(t) = \lim_{t \rightarrow \infty} n_j Q_j(t) \quad (2.4)$$

2.2.3 DISTRIBUTED SECONDARY CONTROL

The droop control method suffers from frequency and voltage amplitude deviation. Therefore, the secondary control strategy [28],[33] is employed to restore the frequency and voltage amplitude as follows:

$$\omega_i = \omega_0 + m_i(P_{ri} - P_i) + \omega_{si}. \quad (2.5)$$

$$V_i = V_0 + n_i(Q_{ri} - Q_i) + V_{si}. \quad (2.6)$$

where ω_{si} and V_{si} are the frequency and voltage amplitude compensation terms, respectively, the outcome of the secondary control.

Differentiating the droop characteristic in (2.5) yields:

$$\dot{\omega}_i = \dot{\omega}_{si} - m_i \dot{P}_i. \quad (2.7)$$

$$\dot{\omega}_{si} = \int \vartheta dt = \int (\dot{\omega}_i + \dot{\delta}_i) dt = \int (\vartheta_i^\omega + \vartheta_i^\delta) dt \quad (2.8)$$

where $\delta_i = m_i P_i$ and ϑ_i are the auxiliary control input for adjusting the secondary control set-points.

$$\vartheta_i^\omega = K_\omega \left[\sum_{j \in N_i} a_{ij} (\omega_j - \omega_i) + g_i (\omega_0 - \omega_i) \right] \quad (2.9)$$

$$\vartheta_i^\delta = K_\delta \sum_{j \in N_i} a_{ij} (\delta_j - \delta_i) \quad (2.10)$$

where the loop gain $g_i=1$ is a pinning gain in island mode when the secondary control is enabled; The convergence coefficient $K_\omega > 0$, and we will give the detail of parameter

selection in the later section; ω_0 is the nominal amplitude-frequency which is predefined, used as the reference; ϑ_i^ω is employed to maintain the frequency synchronized among different agencies and promise frequency coverage to ω_0 at last. With ϑ_i^δ , the active power during the whole process of microgrid operation is proportionally shared by all converters.

The research objective of this chapter is an inverter-connected island microgrid, and the control diagram of each converter is shown in Fig.2.2. It should be noticed that this chapter focuses on frequency set-point ω_{si} . The voltage set-point V_{si} comes from a voltage-reactive power control loop and is ignored here.

2

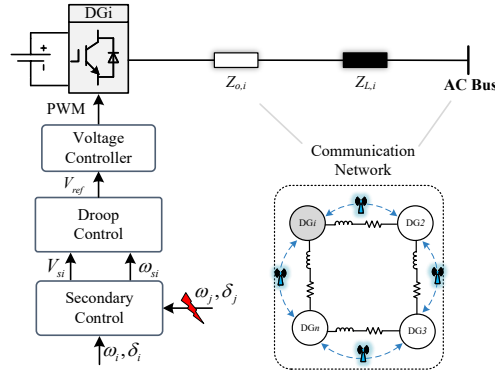


Figure 2.2: An AC microgrid with distributed secondary control strategy consisting of n converters.

With the proposed distributed secondary control algorithm, the microgrid in islanding mode can recover the frequency and share the power proportionally among the participant converters as denoted in (2.3) and (2.4).

2.3 CYBER ATTACK ON DSC

The distributed secondary control can maintain synchronizing frequency and active power as discussed. However, the malicious attack can destabilize the AC microgrids depending on the attack intensity. This section introduces and models the false data injection attack and the denial of service attack. Then, we formulate the secondary resilience synchronization problem for island AC microgrids in the presence of FDIA and DoS attacks. Herein, we only consider the modeling of the secondary frequency control and cyber-attacks model in the frequency data exchanging process in this chapter. It should be noted that this procedure can also be extended to the active power control loop and secondary reactive-voltage control loop.

2.3.1 MODELING OF THE CYBER ATTACK

The proposed distributed control framework given by (2.9) and (2.10) relies heavily on exchanging $\varphi_j = \{\omega_j, \delta_j\}$ among different converters, which makes the cyber-physical system vulnerable to cyber-attacks. FDIA and DoS attacks are typical cyber-attacks. FDIA can be modeled as false data injection [18], while DoS attacks can be considered failing to get the information of the neighboring converters [34]. Cyber attacks on the frequency

propagation channel from the neighboring agent can be modeled in (2.11).

$$\omega_{a,j} = K_j[\omega_j + \eta_j \varepsilon(t)] \quad (2.11)$$

where $\omega_{a,j}$ denotes the frequency information corrupted by cyber attack. ω_j represents the real frequency signal of the j th agent. η_j and K_j are binary variables that indicate the existence of FDIA and DoS attacks. Specifically, $\eta_j = 0$ and $K_j = 0$ indicate there is only a DoS attack; $\eta_j = 0$ and $K_j = 1$ manifest the microgrid system works in the normal state without any cyber-attack; $\eta_j = 1$ and $K_j = 0$ represent the system is challenged by DoS attack and FDIA at the same time; while $\eta_j = 1$ and $K_j = 1$ denote the presence of FDIA with the malicious element $\varepsilon(t)$.

In the presence of cyber attacks, (2.9) can be rewritten as (2.12).

$$\dot{\omega}_i = K_\omega \left[\sum_{j \in N_i} a_{ij}(\omega_{a,j} - \omega_i) + g_i(\omega_0 - \omega_i) \right] \quad (2.12)$$

The state error e_i , which is expected to be 0, is the error between the i th inverters' frequency and the nominal frequency, i.e., $e_i = \omega_i - \omega_0$. The dynamics of state errors with attacks on communication links are stated as follows:

$$\dot{e}(t) = -K_\omega(L + G)e(t) + B_a \varepsilon(t) \quad (2.13)$$

where L is the Laplacian matrix of the communication network. $G = \text{diag}(g_1, \dots, g_N)$ denotes the enabling of secondary control. $K_\omega(L + G)$ characterizes the algebraic connectivity of the augmented communication graph, which suggests the convergence rate of distributed control strategies. Obviously, a large $K_\omega(L + G)$ value results in more efficient communication between the involved inverters, and thereby, information can propagate faster in the neighbor-neighbor communication network. Since the L and G are demonstrated by the communication network, K_ω is the only factor we can adjust the convergence rate of the distributed control strategy in (2.8), which also affects the speed of frequency synchronization in an islanded ac microgrid. So, nonzero values of K_ω are chosen to be sufficiently high. On the other hand, the limitation for K_ω choosing is that the secondary is compensation for the power loop. Thus, the responding speed of the secondary control loop should be lower than the power loop. As the cutoff angular frequency of the power loop's filter is 100 rad/s, K_ω is chosen to be 50 rad/s, half of the inner loop bandwidth. B_a is the communication network incidence matrix between the cyber attack vector and the state error.

2.3.2 CONTROL PROBLEM STATEMENT

According to the described system (2.13), the state error vector can be represented as:

$$e(t) = e^{-K_\omega(L+G)t} e(t_0) + \int_0^t e^{K_\omega(L+G)(\tau-t)} B_a \varepsilon(\tau) d\tau \quad (2.14)$$

If no cyber attacks exist in the microgrid system. In this case, $e(t)$ will gradually reduce to a value that is close to zero since the matrix $-K_\omega(L + G)$ is negative-definite and invertible [28]. When there is a cyber-attack, we assume that the attack signal can be expressed

as $\varepsilon(t)$ as we discussed in (2.11). Furthermore, for a time instant, the fake data can be considered a constant denoted as ε_0 . The error will converge to a non-zero value decided by $\varepsilon(t)$ as stated in (2.15):

$$\begin{aligned} \lim_{t \rightarrow \infty} e(t) &= \int_{t_0}^t e^{-K_\omega(L+G)(t-\tau)} B_a \varepsilon(\tau) d\tau \\ &= \lim_{t \rightarrow \infty} \frac{1 - e^{-K_\omega(L+G)(t-t_0)}}{K_\omega(L+G)} B_a \varepsilon_0 \\ &= [K_\omega(L+G)]^{-1} B_a \varepsilon_0 \end{aligned} \quad (2.15)$$

As shown in (2.15), the state error fails to converge to zero with false data infecting the system, which implies that the cyber-attack would impede the synchronization of frequencies. The proposed secondary cooperative control approach expressed as (2.13) can also be rewritten as follows:

$$\dot{\omega}_i = -K_\omega(L+G)[\omega_i - \underbrace{(\omega'_0 - \Delta\omega_L)}_{\omega_0}] + B_a \varepsilon(t) \quad (2.16)$$

From (2.16) we can find that there is a $\Delta\omega_L$ which makes $-K_\omega(L+G)\Delta\omega_L + B_a \varepsilon = 0$. In this case, the state error space equation can be written as follows:

$$\dot{e}_a = -K_\omega(L+G)e_a \quad (2.17)$$

where $e_a = \omega_i - \omega'_0$. As shown in (2.17), the output frequency would converge to ω'_0 , but not the nominal frequency ω_0 . As the FDIA is bounded false data, the state error will not diverge. It converges to a non-optimal point determined by the inserted fake data $\varepsilon(t)$.

When the communication channel is under DoS attack, neighboring converters become unavailable. In this case, the output of the secondary controller may continuously decrease over time due to the use of the integrator in (2.9). Accordingly, the output of the i th unit will converge to an abnormal value.

In summary, the cyber-attack signals in communication links would propagate through the sparse communication network, distorting the microgrid operating points and driving the microgrid system away from the optimal operating conditions.

2.4 PROPOSED CONTROL AND STABILITY ANALYSIS

In this chapter, we employ adaptive philosophy to configure the controller in a manner that can automatically adjust to the varying conditions of cyber attacks. As is shown in Fig.2.3, to accomplish attack mitigation in AC microgrids, the following adaptive control framework composed of four terms is proposed (2.18)-(2.20):

$$\lambda_{ij} = \kappa |\omega_i - \omega_{a,j}| \quad (2.18)$$

where λ_{ij} is an auxiliary state of the controller of the i th unit. (2.18) is the term for measuring the attack severity, which is used to calculate the level of the malicious signal. At this moment, we suppose that $\omega_{a,j}$ is the output of various state estimators, as the Kalman filter in [15] since the effect of noise is excluded. κ is the gain of the cyber attack

measure term, which should be designed large enough so that a slight attack contributes significantly to adjusting the communication weight. Intuitively, a larger κ increases the sensitivity of the proposed approach towards attacks. Under the satisfaction of this chapter on the cyber attack suppression accuracy, $\kappa = 6$.

$$\Omega_{ij} = e^{-\lambda_{ij}} \quad (2.19)$$

In this resilience-enhanced scheme, by (2.19), the negative relationship between cyber attacks and communication weights is developed. With this term, a more significant attack vector will cause a smaller communication weight. This way, the infected data will not be picked up, and cyber attacks will be rejected. The exponential function is adopted to decrease communication weights because it's more sensitive to attacks than other correlation functions.

$$\rho_{ij} = \Omega_{ij} / (\Omega_{ij} + \dots + \Omega_{iN}) \quad (2.20)$$

In (2.20), a comparing algorithm is proposed to identify the severity of the attacks on each communication line. It is adopted to choose an optimal communication line when all the neighbors are infected. With this term, the less infected line would be chosen to propagate information.

$$\dot{a}_{ij} = \xi \rho_{ij}(t) - \xi a_{ij} \quad (2.21)$$

The term (2.21) is essentially a low pass filter, which is added to prevent unexpected oscillations in the frequency response of converters. ξ demonstrates the cutoff frequency of the low pass filter. A response speed that is too slow will restrict the mitigation speed of the proposed defense strategy. By trade-off between the filter's noise suppression effect and the proposed strategy's response speed, we take $\xi = 100$.

By using the proposed controller, the communication weight inputs previously defined in (2.9) are updated with cyber-attacks as shown in Fig.2.3.

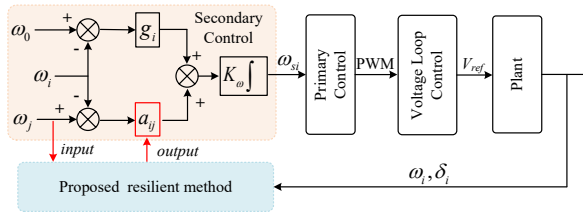


Figure 2.3: Proposed resilience scheme for cyber attacks.

The algorithm below presents the details of the proposed procedures for mitigating cyber attacks when communication channels are invaded.

To analyze the stability of the proposed method, the following Lyapunov candidate is chosen:

$$v(e) = \frac{1}{2} e^T e \quad (2.22)$$

Algorithm 1. Implementation of the Proposed Mechanism**Real-time calculation procedure**

Conventional droop control in (2.1) and (2.2)

Input: Adjacent frequency $\omega_{a,j}$.**Output:** Communication weight a_{ij} .**Step1 :** Attack measure in (2.18).If $|\omega_i - \omega_{a,j}| = 0$.For all adjacent converters, $a_{ij} = 1$.

Else execute Step 2 to Step 4

Step2 : Communication weight generation in (2.19).**Step3 :** Attack severity comparison in (2.20).**Step4 :** Low Pass Filter in (2.21).**End****End** a_{ij} is updated in distributed secondary control in (2.12).

The time derivative of $v(e)$ along the trajectories (2.22) is obtained as follows:

$$\begin{aligned} \dot{v}(e) &= e^T \dot{e} \\ &= -K_\omega(\omega_i - \omega_0)^T [(L + G)(\omega_i - \omega_0) + B_a \varepsilon(t)] \end{aligned} \quad (2.23)$$

According to the adaptive law, when one line gets attacked, the communication weight of the corrupted line is sufficiently low, so the cyber attack's impact is almost zero, denoted as $B_a \varepsilon(t) \approx 0$. Since the matrix $-K_\omega(L + G)$ is negative-definite and inevitable, as discussed. $\dot{v}(e) < 0$ and $\forall e \neq 0$. Hence, the origin in (2.14) is globally asymptotically stable. This way, $v(e)$ would eventually converge to zero, meaning the frequency would remain 50Hz.

When all communication lines are attacked, according to the rule of (2.20), the severe attacks would be disregarded, while the less infected line will cause $B_a \varepsilon(t)$ to be kept at a relatively small value. The origin in (2.14) is Lyapunov stable. This way, the error between the real frequency and the nominal point will also be small. In other words, the small error will not affect the operation of the microgrid. This implies that the control objectives in (2.3) and (2.4) can be reached relatively satisfactorily even in the presence of a cyber-attack vector.

Table 2.1: Attack signals and mitigate the effects of different cases in simulations

Case	attack link	false data	with attack		with defense	
			frequency	power ratio	frequency	power ratio
1	DG2-DG1	1	50.05Hz	3.3:1:1.6	50Hz	1:2:3
2	DG3-DG1	DoS	Oscillation	Oscillation	50Hz	1:2:3
3	DG2-DG1	0.1	50.06Hz	3.8:1:1.7	50.01Hz	1:1.3:1.9
	DG3-DG1	1				
4	DG2-DG1	0.1	Oscillation	Oscillation	50.01Hz	1:1.3:1.9
	DG3-DG1	DoS				

2.5 EXPERIMENTAL VERIFICATION

The proposed adaptive control strategy has been tested by the experiment of a distributed AC microgrid with three inverters connected in parallel to validate its effectiveness. The experiment setup is shown in Fig.2.4. The test plant and control parameters of the microgrid are provided in Table 2.2. In this microgrid system, the output side of the inverters is connected to the AC bus through an LC filter and line impedance. In this chapter, the inverters' output active power rate follows the maximum capacity proportion set as 1:2:3. To investigate the influence of the proposed strategy on the load switch, the load is initially set as 720W and then increased by 240W.

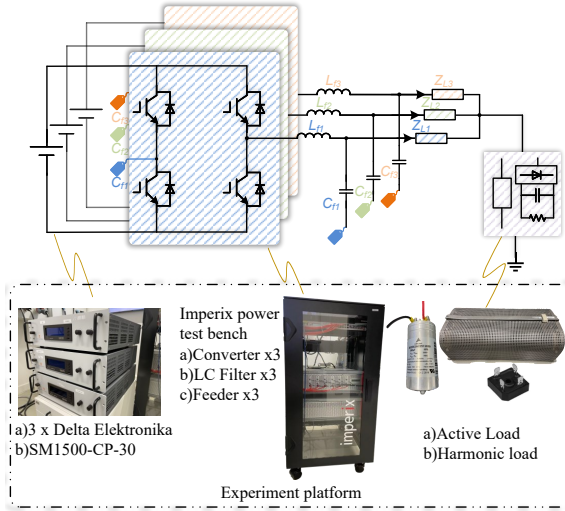


Figure 2.4: Verification setup.

Table 2.2: Parameters of the microgrid for the experiment verification.

Symbol	Description	Value	Symbol	Description	Value
L_{line}	Feeder impedance	$47\mu\text{H}$	m_2	Droop coefficient of DG2	1/600
L_f	LC filter Inductor	2.2mH	m_3	Droop coefficient of DG3	1/900
C_f	LC filter Capacitor	$12\mu\text{F}$	K_ω	Convergence coefficient	50
P_{r1}	DG1 active power reference	300	κ	Gain of attack detection term	6
P_{r2}	DG2 active power reference	600	ξ	Coefficient of resilient term filter	100
P_{r3}	DG3 active power reference	900	ω_0	Nominal angular frequency	314rad/s
m_1	Droop coefficient of DG1	1/300	V_0	Nominal voltage amplitude	190V

Following the structure in Fig.2.4, an analysis to investigate the impact of different cyber attacks on active power sharing and frequency convergence of microgrids is carried out. The simulation plant and control parameters of the microgrid are provided in Table 2.2. The following procedures occur in the microgrid successively:

- (1) Starting the microgrid;
- (2) Activating the secondary control algorithm;
- (3) Launching the cyber attack;
- (4) Enabling the defense mechanism;
- (5) Switching the Load;

To verify the effectiveness of the proposed adaptive control scheme against FDIA and DoS attacks, four cyber-attack cases are conducted in this chapter, as provided in Fig.2.5, including:

Case 1: Single FDIA is launched;

Case 2: Single DoS attack is launched;

Case 3: A combination of different levels of FDIA invading all communication lines;

Case 4: A combination of FDIA and DoS attack to invade all communication lines;

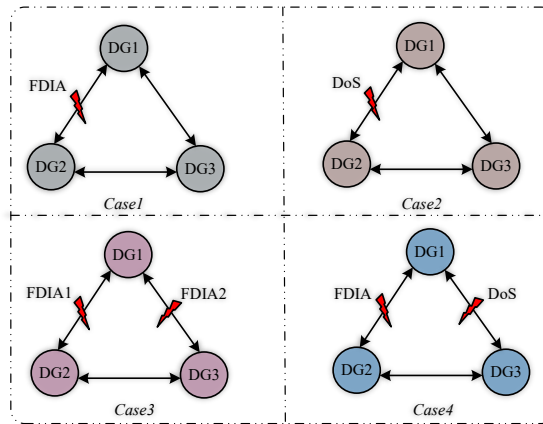


Figure 2.5: The illustration of different cases.

As shown in Fig.2.5, Case 1 and Case 2 demonstrate the effectiveness of mitigating the cyber attack when one of the communication lines is attacked. Case 3 and Case 4 illustrate all communication lines are aggrieved situations. It should be noted that for all cases, initially, the output frequency of the microgrid system is around 50.14 Hz as we apply the droop control to provide the proportional active power sharing with the pre-set ratio among participating inverters.

CASE 1: SINGLE FDIA CORRUPTION

In this case, the communication line 2 to 1 is attacked at $T1, case1$ by FDIA. Fig.2.6 shows the impact of the FDIA attack in terms of active power and frequency, where the designed FDIA can be modeled as frequency offset. It also shows the performance of the proposed strategy for FDIA mitigation.

In Fig.2.6, the active power is proportionally shared among participating inverters at the start stage, and frequencies are restored at the rated 50 Hz after the distributed secondary control method is enabled at $T1, case1$. During the recovering frequency period, the active power will stay output smoothly because of the active power synchronization

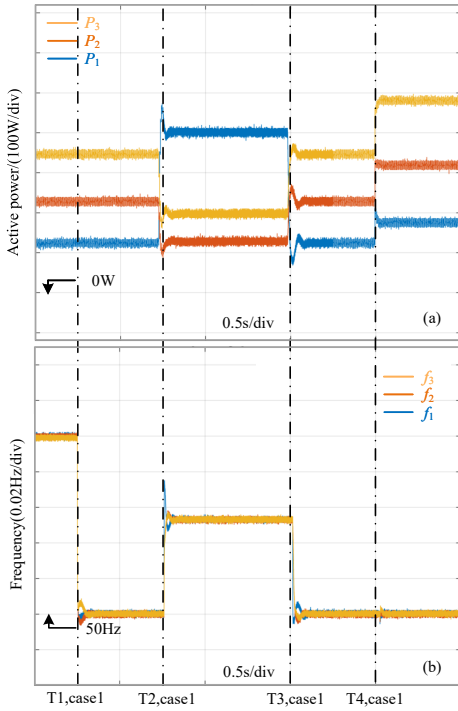


Figure 2.6: The proposed strategy under single FDIA: a) Active power sharing. b) Frequency.

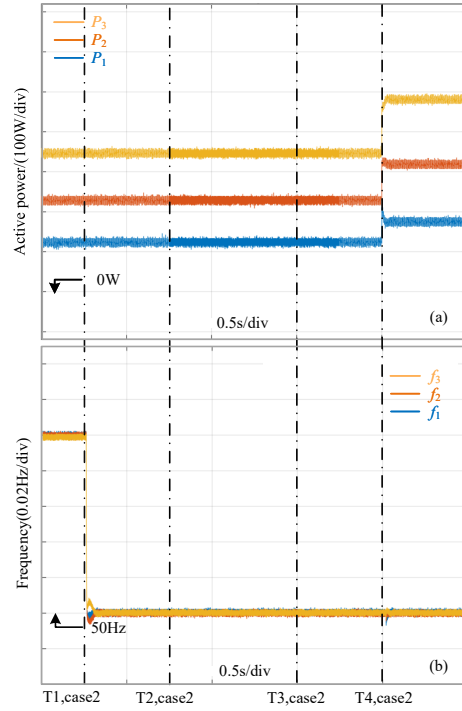


Figure 2.7: The proposed strategy under single DoS: a) Active power sharing. b) Frequency.

term in the distributed secondary control. At $T2,case1$, the information in the network is corrupted by injecting false data $\varepsilon_{2,1}(t) = 1$ on communication line 2-1, which shifts the frequency to about 50.05Hz, and the proportionally active power sharing is interrupted. This implies that the inverter system will not perform at the default nominal frequency point. The inverters cannot share the active power as the capacity ratio. At $T3,case1$, the adaptive scheme is triggered, after which the communication weight of the attacked line is automatically reduced, thus preventing the propagation of the compromised signal. As a result, the frequency will return to 50 Hz, and the active power-sharing ratio will recover from 3.3:1:1.6 to 1:2:3. The present proposed control strategy is also implemented in the load-switching scenario. We add 240W load at $T4,case1$, and the frequency shows regular fluctuations, which will quickly return to the nominal value. In other words, activating the proposed defenses will not affect the load-switching features of the microgrid.

CASE2:SINGLE DoS ATTACK CORRUPTION

In this case, The single DoS hacks the communication line 2 to 1 at $T2,case1$. Fig.2.7 shows the effect of the DoS attack on the output active power and frequency and then indicates the effect of the proposed defense mechanism against the DoS attack. With the cooperation of droop control and distributed secondary control algorithms from $T1,case1$, the frequency

and power dispatch of the microgrid are both desirable.

It should be noted that the implementation of the DoS attack will lead to a severe power oscillation since the frequencies among different DGs are different during the dynamic process, as shown in simulation results in [35], which will trigger the over-current protection of the platform. To avoid this problem, We change the order of the experiment procedure, first enabling the defense mechanism at $T2,case2$ and then imposing the DoS attack at $T3,case2$ in Case 2 and Case 4.

According to [35], the proposed strategy is enabled for attenuating the DoS attack effect so that the corrupted signal cannot compromise the overall microgrid system. Subsequently, the frequency is gradually restored to 50Hz. The active power-sharing ratio also returns to 1:2:3. It is notable that with the defense measure, the adverse effect of cyber attacks is eliminated as the system is restored to its normal state.

CASE3:A COMBINATION OF FDIAs CORRUPTION

Fig.2.8 shows the waveforms of the output frequency and active power of inverters when different levels of FDIA invade all communication lines. Before $T2,case3$, when the system is not subject to any cyber attack, the output frequency and active power are managed by the conventional distributed secondary control to track the reference. False data $\varepsilon_{2,1}(t) = 1$ upon communication line 2-1 is launched at $T2,case3$.

In this case, there would be a frequency deviation from the optimal point because the fake data injected into the communication network leads to a devastating frequency convergence performance. The malicious signals in the attacked communication also disrupt the proportional active power sharing among participating inverters. At $T2,case3$, Another FDIA $\varepsilon_{3,1}(t) = 0.1$ on communication line 3-1 is imposed, which will further deteriorate frequency convergence performance to 50.06Hz from 50.05Hz and active power sharing ratio to 3.8:1:1.7 from the ratio of 3.3:1:1.6. At $T4,case3$, the proposed adaptive strategy is activated. The microgrid performance will be restored satisfactorily as the proposed resilient controller almost blocks the more serious infected signal.

CASE4:A COMBINATION OF FDIA AND DoS CORRUPTION

In Fig.2.9, a combination of DoS and FDIA attacks infests all communication lines. The details of the offensive and defensive performance are analyzed as follows. The defense mechanism is enabled at $T2,case4$, which will not affect the normal operation. At $T3,case4$, the DoS attack on communication line 3-1 and FDIA on communication line 2-1 are imposed at the same time. In this stage, the DoS attack would be disregarded as defensive measures take effect. In this case, the microgrid system would keep a relatively normal state where the frequency is 50.01 Hz, and the active power sharing ratio can be recovered to 1:1.3:1.9. At $T4,case4$, and we add 240W load into the inverters system. It is illustrated that the adopted adaptive strategy will not affect the regular load switch operation for all communication line-attacked scenarios.

In summary, the single attack or combination of attacks on communication links would disrupt the participating inverters' proportional active power sharing and frequency restoration. By using the proposed control strategy, the corrupted links are damped. As a result, a microgrid's optimal control objectives will be satisfied under various scenarios, including load switching, hackers invading by a single attack, or a combination of attacks.

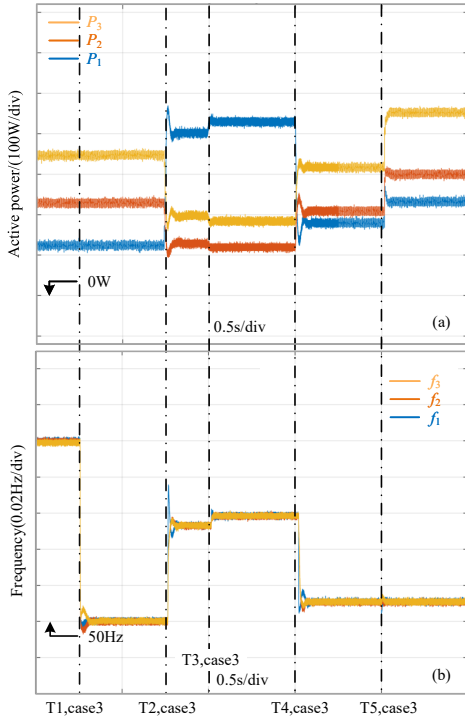


Figure 2.8: The proposed strategy under a combination of FDIA: a) Active power sharing. b) Frequency.

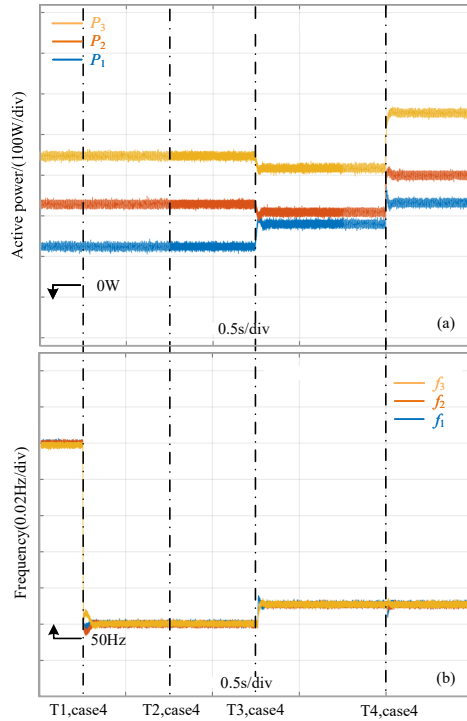


Figure 2.9: The proposed strategy under FDIA and DoS combination: a) Active power sharing. b) Frequency.

2.6 CONCLUSION

This chapter presents a control scheme for FDIA and DoS attacks in the secondary-frequency layer of AC microgrids. It assumes there is communication between two neighbor units. With the proposed control, the signals from the attacked communication channel will be weighted lower. The more the signal deviates from the average, the lower it is weighted. The effect of the corrupted signal will be exponentially attenuated when the signal deviates from the norm. In this way, even if all the communications to a unit are corrupted, the signals from each communication line are optimally weighted depending on how much the signals are falsified. As a result, the proposed control significantly enhances the resilience of AC microgrids under cyber-attack.

3

DISTRIBUTED CONTROL FOR POWER REGULATION WITH LOW VULNERABILITY

In microgrids, alongside frequency and voltage amplitude restoration, achieving proper power regulation is a key challenge. Accurately sharing active, reactive, and harmonic power while maintaining low bus voltage distortion is particularly difficult in AC microgrids with mismatched feeder impedances. This chapter presents a distributed virtual impedance (DVI) control strategy to address this issue in microgrids with both inductive and resistive feeders. The approach adjusts fundamental and harmonic impedance to desired values by exchanging information among neighboring inverters. To enhance dynamic performance, a distributed model predictive control (DMPC) scheme is introduced to regulate virtual impedance. This distributed strategy eliminates the need for a central controller and improves resilience against communication failures by carefully designing the communication matrix. The proposed methods are robust against communication delays, failures, and cyber-attacks while also reducing communication requirements. The effectiveness of the approach is demonstrated through experiments conducted under various scenarios, including communication disruptions and plug-and-play operations.

This chapter is based on:

-J. Xiao, L. Wang, P. Bauer and Z. Qin, "A Consensus Algorithm-Based Secondary Control with Low Vulnerability in Microgrids," IEEE Transactions on Industrial Informatics, Early Access, 2024.

-J. Xiao, L. Wang, P. Bauer and Z. Qin, "Virtual Impedance Control for Load Sharing and Bus Voltage Quality Improvement in Low-Voltage AC Microgrid," IEEE Transactions on Smart Grid, vol. 15, no. 3, pp. 2447-2458, 2024.

-J. Xiao, L. Wang, Y. Wan, P. Bauer and Z. Qin, "Distributed Model Predictive Control-Based Secondary Control for Power Regulation in AC Microgrids," IEEE Transactions on Smart Grid, vol. 15, no. 6, pp. 5298-5308, 2024.

3.1 INTRODUCTION

In medium/high voltage microgrids, feeders are usually inductance-dominated (IDF), and the droop method is often used to regulate active power [36–39]. However, this method struggles to address issues like harmonic power and reactive power-sharing discrepancies. These problems arise because, in practice, controller parameters and feeder impedances often vary between different distributed generators [40]. On the other hand, in low-voltage microgrids, the droop control method ($Q-\omega$ and $P-V$) is widely applied due to the resistance-dominated nature of the feeders (RDF) [41]. While frequency, being a global variable, allows reactive power to be shared proportionally [42], accurate sharing of active power is still difficult. Additionally, sensitive loads in microgrid systems are mostly nonlinear [43, 44], which makes it necessary to share the harmonic power generated by these loads properly among DG units—which the traditional droop method does not address.

Different power regulation schemes have been developed to address this issue. Intuitively, designing an accurate virtual impedance [45], [46] or properly tuning droop coefficient [47] can contribute to accurate power sharing; however, it is generally impossible to acquire the actual physical line impedance of each feeder in practice. A sizeable virtual impedance is suggested in [48], [49] to smoothen out the impedance mismatch. However, this may make the bus voltage highly distorted. The methods proposed in [50] and [51] can be utilized to compensate for bus voltage, While it is not easily measured. As a critical technology for cyber-physical systems [52], communication technology merits adoption to address the power-sharing concerns of microgrids. A centralized microgrid central controller (MGCC) is adopted in [53, 54]. The controller modifies the virtual impedance in real-time. However, it relies on the reliability of the center controller.

To cope with the "single point of failure" in MGCC, the distributed philosophy has been used in the microgrid to improve its reliability. In [55][32], consensus algorithm-based distributed secondary control has recently been proposed in parallel inverter systems. The distributed averaging proportional-integral (DAPI) scheme suggested uses the proportional-integral-based secondary control to adjust the voltage and frequency compensation terms to compensate for active and reactive power consumption [33, 56]. However, this method is characterized by a large amount of data exchange among the inverters because it requires periodic data exchange with the neighbor. Unfortunately, the limited communication resources may result in poor performance of the distributed system [57]. Alternatively, a discrete-time communication mechanism is proposed in [58] to alleviate the need for communication to some extent.

The event-triggered control (ETC) framework has drawn increasing interest recently within the multi-agent systems (MAS) field [59]. Compared to the typical periodic approach, its main advantage is that communication is conducted non-periodic, and therefore, the communication dependency between individual units can be further reduced. It has been applied in the microgrid field [60]. Most recently, a dynamic ETC architecture was introduced to reduce communication demands while keeping power sharing. In the hypothesis, the convergence law is only activated when the output power varies [61]. In practice, the huge traffic demands placed on the communication network are not relieved because many loads on the AC bus can change frequently.

Besides the communication dependency issues, the reliance on communication technology of distributed control makes the system vulnerable to cyber-attacks and communication

disruption, which can degrade the control accuracy and cause system instability [27, 35].

To cope with the abovementioned issues, in this chapter, we investigate the proportional sharing of the harmonic, active, and reactive power while promising voltage quality under inductive and resistive feeders, respectively. Moreover, it allows the communication to be switched off once the communicated signal is constructed, which reduces the communication dependency in [27, 32, 35, 51, 55, 57, 58, 60, 61] and vulnerability further. Considering the cyber attack, different resilient controls are equipped in the secondary control layer, including the corrupted signal block and reconstruction.

A comparison between the proposed method for power regulation and previous research is shown in Tab.3.1. It demonstrates a gradual improvement in control performance, as indicated by the increasing trend of $\circ \bullet \ominus \ominus$, while the symbol \backslash denotes an inapplicable evaluation index.

Table 3.1: Comparison of the proposed PI-consensus-based virtual impedance with references.

Ref	Line info	PCC info	Accuracy	Voltage Quality	Distributed Manner	Com Delay	Com Cost	Com Exit	Resilient
[40]	●	●	○	●	○	●	○	◐	○
[45, 46]	●	○	◐	○	\	\	\	\	\
[48, 49]	●	●	◐	○	\	\	\	\	\
[50, 51]	●	○	◐	◐	\	\	\	\	\
[53, 54]	●	●	●	●	○	○	○	○	○
[32, 55]	●	●	●	●	●	●	○	○	○
[58]	●	●	●	●	●	●	◐	○	○
[60, 61]	●	●	●	●	●	●	◐	○	○
[27, 35]	●	●	●	●	●	●	○	◐	◐
Proposed	●	●	●	●	●	●	●	●	●

Moreover, the mentioned traditional DAPI-based approach predominantly employs PI controllers with fixed control laws, which do not guarantee optimal solutions [62]. Additionally, the DAPI-based approach fails to account for practical constraints in real-world applications [9, 35]. When uncertainty is introduced into the information transmission, these methods may yield irregular secondary control outputs, reducing the overall robustness of the system. To that end, the model predictive control (MPC) algorithm emerges as a viable solution, addressing the challenges associated with DAPI-based control by utilizing the predictive models to anticipate future system behavior [63, 64]. It benefits physical limitation under uncertainty and optimal secondary layer output. The distributed model predictive control has been reported to compensate the voltage for power sharing [63–69]. Each inverter autonomously addresses the local voltage optimization problem through a fully distributed approach, utilizing its forecasted actions and information from adjacent units.

Notably, the introduction of DMPC algorithms raises two main concerns. First, when continuous prediction is needed, their prediction mechanisms may impose computational

burdens that may be untenable in practical scenarios, especially when computational resources are limited [67]. Second, the distributed philosophy of DMPC emphasizes information propagation within the communication network, which may face challenges such as limited bandwidth, time delays, and traffic congestion. These communication constraints can significantly compromise the system's responsiveness [57]. The primary concern with DMPC arises from the continuous communication and computation requirements of traditional methods. In these approaches, controllers operate in a time-triggered manner, performing data acquisition and control operations periodically [58]. As a result, this can lead to inefficient use of computational and communication resources since much of the data exchange and computation may not be necessary to achieve the desired overall system response.

To alleviate the communication and computational burden, event-triggered control using non-periodic communication is used in DMPC-based secondary control [63]. With the event-triggered mechanism [70], secondary control is activated only when the preset condition is triggered, achieving a relatively better control performance with limited communication resources. Furthermore, the integration of virtual impedance (VI) control further reduces communication dependency. Compared to the voltage compensation (VC) method in secondary control in [67], it features less communication dependency since extra computation is no longer needed once the virtual impedance is appropriately adjusted [71–73].

Table 3.2: Comparison of different distributed secondary controls.

Control Reference	Description	Performance	Control Reference	Description	Performance
DAPI	-Suboptimal solution	●	DMPC	-Comms burden	●
	VC [33, 35, 56] -No physical constraint			VC [63–69] -Optimal solution	
VI	-Comms burden	●	VI Proposed	-Physical constraint	●
	-Suboptimal solution			-Optimal solution	
	VI [32, 61, 73] -No physical constraint			-Comms relaxation	
	-Comms relaxation			-Physical constraint	

However, existing virtual impedance controls are based on DAPI [32, 73], limiting their ability to offer optimal adjustments and account for physical constraints in the secondary layer, as stated. A comparative study is conducted in Table 3.2, showcasing the different features of various distributed secondary controls. To the best of the authors' knowledge, the distributed model predictive control-based virtual impedance control of the secondary layer has not been addressed in the existing research.

To address the limitations of conventional DAPI-based control, which does not consider physical constraints, and the communication burden and failures experienced by existing DMPC-based methods, this chapter further presents a novel DMPC-based virtual impedance approach for secondary control in AC microgrids with resistive feeders. This algorithm optimizes both fundamental and harmonic virtual impedance to enhance active

and harmonic power sharing. The main benefits of the proposed DMPC scheme are outlined as follows:

1. Unlike previously reported DMPC-based secondary control techniques, the proposed scheme is the first to explore DMPC for virtual impedance control. This allows for integrating fundamental and harmonic impedance regulation into a single multi-input, multi-output distributed controller, facilitating power sharing.
2. Leveraging the DMPC mathematical model, which considers local voltage, frequency, power equations, and neighboring information, the proposed DMPC controller can predict microgrid behavior and optimize secondary layer output.

The chapter is structured as follows: Section.3.2 discusses the control and power-sharing issues of islanding microgrids. Section.3.3 presents the resilient consensus algorithm for active, reactive power, and harmonic power sharing. Section.3.4 introduces the distributed model predictive control for power sharing. Section.3.5 shows the experimental evaluation of the suggested control methods. Subsequently, Section.3.6 concludes the chapter.

3.2 ISLAND MICROGRID ANALYSIS

This section addresses key performance indices in microgrids, including active power, reactive power, harmonic power sharing, and PCC voltage quality. It explains why traditional droop control methods struggle to achieve accurate power sharing and maintain voltage quality at the PCC. These limitations highlight the need for the proposed PI-consensus algorithm, which offers a more effective solution to these challenges.

3.2.1 PRIMARY DROOP CONTROL

Under the inductive feeder, the P- ω and Q-V droop law is shown in (2.1) and (2.2). As ω_i is a global variable, suggesting that active power can naturally be shared proportionally. Reactive power sharing, in contrast, becomes more complex given the mismatched feeder impedance and varying droop factors.

Under resistive feeder, the P-V and Q- ω droop laws are extensively utilized for power flow regulation, as demonstrated in equations (3.1) and (3.2):

$$\omega_i = \omega_0 + n_i Q_i. \quad (3.1)$$

$$V_i = V_0 - m_i P_i. \quad (3.2)$$

Similarly, ω_i is the global variable, which means the output frequencies among the participating converters are the same, the active power could be proportionally shared, $n_1 Q_1 = n_2 Q_2 = \dots = n_i Q_i$. However, it is challenging to reach active power sharing because the V_i is different for different units.

The reference for the inner controller that manages the actual output voltage of the filter capacitor is derived from the outcome of the droop control. It can be written as (3.3):

$$V_{d,i} = V_i \sin\left(\int \omega_i dt\right) \quad (3.3)$$

The inner control is usually composed of a voltage controller and a current controller, in which the reference is the output of the droop controller, denoted as $V_{ref,i} = V_{d,i}$. The control block diagram of the inner loop controller can be equivalent to (3.4).

$$V_{c,i} = V_{ref,i} \cdot G_v(s) - Z_{o,i}(s) \cdot i_{o,i} \quad (3.4)$$

where $G_v(s)$ denotes the voltage gain of the inner controller, which should be 1 for a well-designed converter, and $Z_{o,i}(s)$ indicates the equivalent impedance of the inverter is determined jointly by the controller's parameters [74] and the droop coefficient.

3

3.2.2 REACTIVE POWER SHARING ANALYSIS UNDER IDF

Under inductive feeder, the voltage drop [61] across the transmission line can be expressed as (3.5):

$$\Delta V_i \approx \frac{X_i Q_i + R_i P_i}{V_{c,i}} \quad (3.5)$$

where X_i and R_i describe the inductance and resistance of the physical feeder. ΔV_i represents the voltage drop and $V_{c,i}$ indicates the filter capacitor voltage.

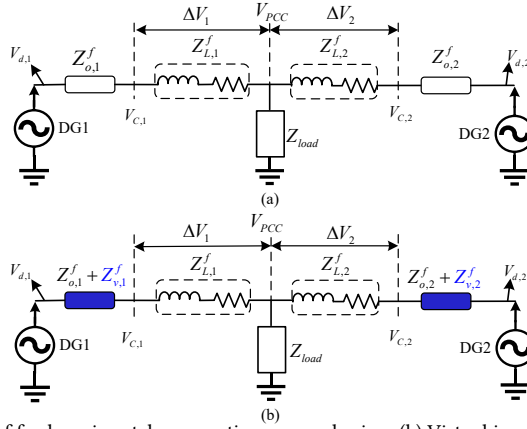


Figure 3.1: (a) The effect of feeder mismatch on reactive power sharing. (b) Virtual impedance on reactive power control.

The effect of feeder and inverter output impedance on reactive power sharing can be illustrated in a simplified microgrid with two inverters, as shown in Fig.3.1. Herein, the V_{PCC} represents the voltage point of common coupling. The transfer functions under the fundamental frequency and the h th harmonic frequency are denoted by the upper corners f and h , respectively. $Z_{o,i}^f$, $Z_{L,i}^f$ and $Z_{v,i}^f$ in indicate the output fundamental impedance, fundamental line impedance, and virtual fundamental impedance of DG_i , respectively. $V_{d,i}$ is the output of the droop controller. $Z_{o,i}^h$, $Z_{L,i}^h$ and $Z_{v,i}^h$ in Fig.3.3 denotes the corresponding harmonic components.

It is apparent that the resistive component of the feeder, combined with the mismatched inductive impedance, can result in an incorrect share of reactive power. Nevertheless, when

the feeder features inductance, which means $R_i \leq X_i$. It is reasonably assumed that the line is inductive, which allows for the restatement of (3.5) as (3.6).

$$\Delta V_i \approx \frac{X_i Q_i}{V_{c,i}} \tag{3.6}$$

3.2.3 ACTIVE POWER SHARING ANALYSIS UNDER RDF

Notably, in the resistive feeder systems, $R_i \gg X_i$ [71]. As a result, the power flow through the line resistance leads to the voltage drop, which is expressed as (3.7).

$$\Delta V_i \approx \frac{R_i P_i}{V_{c,i}} \tag{3.7}$$

Therefore, the voltage drop between the participating units is regulated, and proportionate sharing of active power is achieved by appropriately modulating the individual virtual impedance to maintain proportionality. Based on (3.6) and (3.7), there are two primary approaches for modifying the output active power. Taking IDF as an example, the first approach involves adjusting the voltage drop, ΔV , across the feeder, as shown in Fig.3.1. This adjustment is typically accomplished by altering the voltage reference of the filter capacitor. The second approach involves tuning the feeder’s impedance, which can equivalently be achieved by modifying the virtual impedance, represented as $i_o \cdot Z_v(s)$ in Fig.3.2. In this research, the virtual impedance method is adopted due to its minimal reliance on communication links.

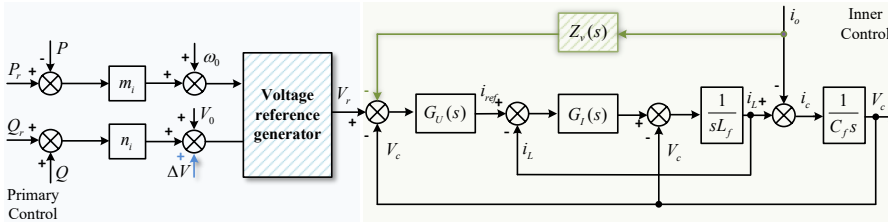


Figure 3.2: The implementation of the voltage compensation and virtual impedance control for power sharing.

3.2.4 HARMONIC POWER ANALYSIS

The following prerequisites must be satisfied for the proportional sharing of harmonic power with its maximum output harmonic power rate.

$$b_1 H_1 = b_2 H_2 = \dots = b_i H_i \tag{3.8}$$

where b_i is the inverse of the maximum output harmonic power of i th DG. H_i denotes the h -th harmonic power. Fig.3.3(a) indicates the equivalent circuit of the inverter system at h th-order harmonic frequency with a nonlinear load. Note that the nonlinear load can be regarded as a current source i_{load}^h [73]. Where $Z_{o,1}^h$ and $Z_{o,2}^h$ indicate the harmonic output impedance in (3.4). $Z_{L,1}^h$ and $Z_{L,2}^h$ denote the harmonic line impedance of feeder 1 and feeder 2, respectively, in Fig.3.3.

The mismatch of harmonic impedance between $DG1$ and $DG2$ leads to incorrect harmonic power sharing, as illustrated in Fig.3.3(a) and Fig.3.3(b) as the h th-order load harmonic impedance Z_{load}^h is significantly bigger than the equivalent impedance Z_{eq}^h of DGs. Nonetheless, the parallel converter's voltage is the same, and harmonic power sharing could be achieved for selected frequencies by constructing the appropriate virtual harmonic impedance $Z_{v,1}^h$ and $Z_{v,2}^h$, as illustrated in (3.9).

$$i_{o,1}^h(Z_{o,1}^h + Z_{v,1}^h + Z_{L,1}^h) = i_{o,2}^h(Z_{o,2}^h + Z_{v,2}^h + Z_{L,2}^h) \quad (3.9)$$

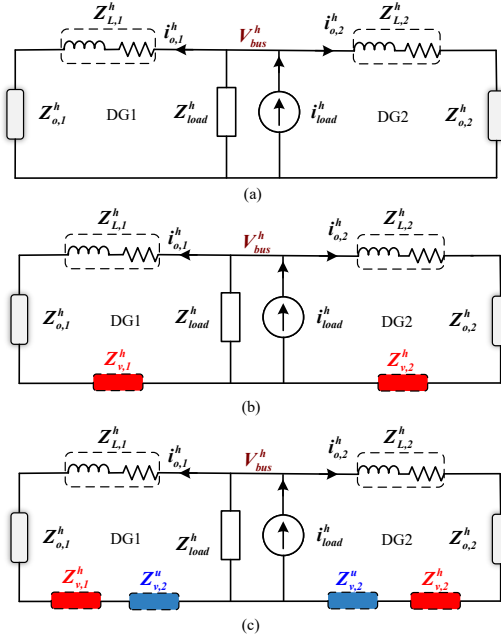


Figure 3.3: (a) The effect of feeder mismatch on harmonic current sharing. (b) Virtual impedance on harmonic current control. (c) Virtual impedance on harmonic voltage control.

3.2.5 BUS VOLTAGE COMPENSATION ANALYSIS

The bus voltage is determined by a combination of the harmonic currents produced by the nonlinear load and the equivalent impedance of each inverter. The h -th bus harmonic voltage is expressed as (3.10).

$$V_{bus}^h = i_{o,1}^h Z_{eq,1}^h = i_{o,2}^h Z_{eq,2}^h \quad (3.10)$$

where $Z_{eq,1}^h$ and $Z_{eq,2}^h$ represent the equivalent impedance of $DG1$ and $DG2$, including output impedance, line impedance and virtual impedance under h -th harmonic current, denoted as $Z_{eq,i}^h = Z_{o,i}^h + Z_{v,i}^h + Z_{L,i}^h$. (3.10) demonstrates that it is possible to attenuate the

bus voltage harmonic V_{bus}^h by adjusting the DGs virtual impedance for harmonic voltage compensation $Z_{v,i}^u$ as shown in Fig.3.3(c).

3.2.6 HARMONIC EXTRACT AND POWER CALCULATION

In this chapter, we use the multi-second-order generalized integrator (SOGI) in [75] to extract fundamental current $i_o^f(t)$, harmonic current $i_o^h(t)$ and harmonic voltage $V_{bus}^h(t)$ as shown in Fig.3.4.

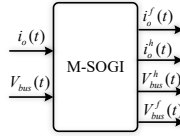


Figure 3.4: The employed second-order generalized integrator (SOGI) in [75].

The h th harmonic power of the i th inverter is calculated based on the root mean square (RMS) value $V_{i,rms}^f$ of the fundamental voltage, the RMS value of harmonic current $i_{o,irms}^h$ and its conjugated signal $i_{o,d}^h$ as [76, 77] which can be denoted as (3.11).

$$H_i = V_{i,rms}^f i_{o,irms}^h = \frac{1}{2} V_i \sqrt{(i_{o,i}^h)^2 + (i_{o,id}^h)^2} \quad (3.11)$$

where $V_{i,rms} = V_i / \sqrt{2}$.

3.3 THE RESILIENT PI-CONSENSUS LAW FOR POWER REGULATION

The PI-consensus algorithm is utilized to facilitate power sharing and mitigate PCC voltage distortion in microgrids dominated by either inductive or resistive feeders. However, the algorithm is vulnerable to cyber-attacks and communication disruptions due to its reliance on transmitted information. This section models each potential threat and then proposes resilient controllers designed to counter cyber-attacks and communication failures. Additionally, an auxiliary controller is introduced to conserve communication resources and reduce vulnerability to communication issues by deactivating the communication network when necessary. This approach is justified as the impact of virtual impedance can emulate physical feeder impedance. If the feeder impedance is appropriately configured, communication becomes unnecessary. This enables the microgrid to maintain plug-and-play functionality and robust operation even without continuous communication.

3.3.1 DISTRIBUTED VIRTUAL IMPEDANCE UNDER INDUCTIVE FEEDER

Virtual impedance can be employed to modify the equivalent impedance of DGs, thereby adjusting the power flow within the system. The consensus algorithm replaces the need for a central controller, enhancing the system's reliability and robustness.

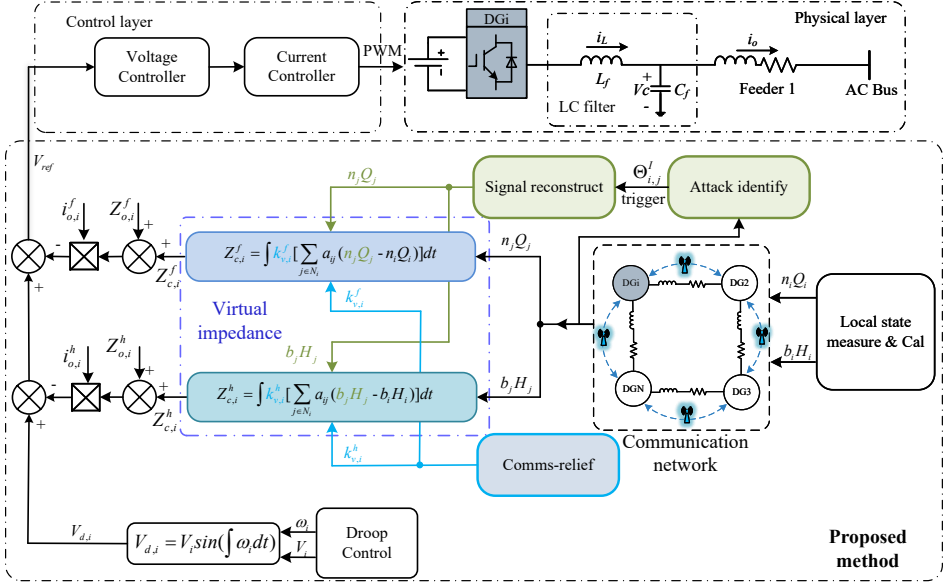


Figure 3.5: The proposed virtual impedance framework under inductive feeder.

CONSENSUS-LAW BASED VIRTUAL IMPEDANCE FOR IDF

In Fig.3.5, the inverters exchange information related to reactive power ($n_1 Q_1^f, \dots, n_n Q_n^f$) and harmonic power ($b_1 H_1^h, \dots, b_n H_n^h$) with their adjacent units to achieve a consensus state. The reshaped consensus algorithm-based virtual fundamental impedances are expressed as (3.12) and (3.13).

$$Z_{v,i}^f = Z_{0,i}^f + Z_{c,i}^f \quad (3.12)$$

$$Z_{c,i}^f = \int k_{v,i}^f \left[\sum_{j \in N_i} a_{ij} (n_i Q_i^f - n_j Q_j^f) \right] dt \quad (3.13)$$

The harmonic impedance can be modulated as (3.14) and (3.15).

$$Z_{v,i}^h = Z_{0,i}^h + Z_{c,i}^h \quad (3.14)$$

$$Z_{c,i}^h = \int k_{v,i}^h \left[\sum_{j \in N_i} a_{ij} (b_i H_i^h - b_j H_j^h) \right] dt \quad (3.15)$$

The fixed virtual inductors $Z_{0,i}^f$ and $Z_{0,i}^h$ are initial virtual impedance values used to improve the impedance's inductive response and thus the system's stability. The adaptively adjusted impedance $Z_{c,i}^f$ and $Z_{c,i}^h$ are determined by the neighbor's information and the state of the local unit. The impedance reshaping factors for harmonic and reactive power sharing loops are $k_{v,i}^h$ and $k_{v,i}^f$, respectively. In practice, the transmitted information exhibits time variation, incorporating time delays. The application of integral controllers is necessary

to compensate for harmonic and reactive power-sharing errors. It's noteworthy that the delay in control performance has been detailed in [54]. For brevity, we omitted this aspect in the current presentation.

With distributed virtual impedance control, the voltage reference for the capacitor voltage modifies as (3.16):

$$V_C = V_d - Z_v^f i_o^f - Z_v^h i_o^h - Z_o^f i_o^f - Z_o^h i_o^h \quad (3.16)$$

CYBER ATTACK ON DVI

Here, the false data injection attack is the main concern in the distributed virtual impedance. It can be modeled as in (3.17).

$$x_{a,j} = x_j + \eta_j \varepsilon(t) \quad (3.17)$$

where $x_{a,j}$ denotes the transmitted information corrupted by cyber attack. ω_j represents the real information of the j th agent. η_j is binary variables that indicate the existence of FDIA. $\eta_j = 0$ illustrates the regular communication $\eta_j = 1$ denote the presence of FDIA with the malicious element $\varepsilon(t)$.

For reactive power sharing controller: With the equivalent effect of virtual impedance and feeder impedance, we can intuitively develop an expression for reactive power and fundamental impedance from (3.6), denoted as $Q_i = H_L^f / (Z_{v,i}^f + Z_{o,i}^f + Z_{L,i}^f)$, where $H_L^f = \Delta V_i V_{c,i}$. Given the existence of FDIA on the communication network, the methods proposed can be represented in (3.18).

$$Q_i = \frac{H_L^f}{\int k_{v,i}^f \sum_{j \in N_i} a_{ij} (n_i Q_i - n_j Q_{a,j}) dt + Z_{e,i}^f} \quad (3.18)$$

where $Z_{e,i}^f = Z_{0,i}^f + Z_{o,i}^f + Z_{L,i}^f$, represents the equivalent value of the fixed impedance. The power-sharing error, which is supposed to be 0, is given by the deviation between the reactive power-sharing performance of the i th inverter and its neighbor j th inverter, expressed as $(n_i Q_i - n_j Q_j)$. In a normal situation ($n_1 Q_1 = \dots = n_i Q_i = Q_i^*$), here, Q_i^* describes the average output reactive power sharing ratio among the system. The dynamics of state errors under attacks against communication channels are given below:

$$\dot{Q}_i = \frac{-H_L^f k_{v,i}^f [Ln_i Q_i - B_a \varepsilon(t)]}{\{\int k_{v,i}^f [Ln_i Q_i - B_a \varepsilon(t)] dt + Z_{e,i}^f\}^2} \quad (3.19)$$

where B_a is the cyber attack incidence matrix.

For harmonic power sharing controller: As shown in Fig.3.3, we can also take $H_i = H_L^h / (Z_{v,i}^h + Z_{o,i}^h + Z_{L,i}^h)$, where H_L^h represents the inverse of the impedance and the harmonic power. Combining (3.14) and (3.15), the relationship of harmonic power and transmitted information can be shown as follows:

$$H_i = \frac{H_L^h}{\int k_{v,i}^h [\sum_{j \in N_i} a_{ij} (b_i H_i - b_j H_{a,j})] dt + Z_{e,i}^h} \quad (3.20)$$

where $Z_{e,i}^h = Z_{0,i}^h + Z_{o,i}^h + Z_{L,i}^h$. The state error of harmonic power sharing is $(b_i H_i - b_j H_j)$. In the normal state, $(b_1 H_1 = \dots = b_i H_i = H_i^*)$, where H_i^* represents the average harmonic power-sharing ratio in the system. When the communication channel is subjected to FDIA, the derivative of the harmonic power sharing errors can be written as (3.21):

$$\dot{H}_i = \frac{-H_L^h k_{v,i}^h [L b_i H_i - B_a \varepsilon(t)]}{\{\int k_{v,i}^h [L b_i H_i - B_a \varepsilon(t)] dt + Z_{e,i}^h\}^2} \quad (3.21)$$

3

STABILITY ANALYSIS

To analyze the stability, we consider the Lyapunov function candidate in (3.22).

$$v(x) = \frac{1}{2} x^T L x \quad (3.22)$$

where x is the state $n_i Q_i$ and $b_i H_i$ of the designed control, in an simplified expression. Combining (3.19) and (3.21), the derivative in time of $v(x)$ along the trajectories (3.22) of the two controllers is given by:

$$\begin{aligned} \dot{v}(x) &= x^T L \dot{x} \\ &= x^T L \frac{-k_i H_L k_{v,i} [L x - B_a \varepsilon(t)]}{\{\int k_{v,i} [L x - B_a \varepsilon(t)] dt + Z_{e,i}\}^2} \end{aligned} \quad (3.23)$$

where k_i represents the coefficient n_i and b_i . In eq.(3.23), without any cyber attacks, that is, $B_a \varepsilon(t) = 0$ and $\dot{v}(x) < 0$ for all $x \neq 0$ at the steady state. This implies that the chosen Lyapunov function is globally asymptotically stable. Hence, $v(x)$ ultimately tends to zero, making the state error converge to zero and enabling the reactive and harmonic power to be shared proportionally.

When the grid is subjected to a FDIA with a malicious signal ε , a new state x_p is introduced to clarify the system's dynamics, where $L x_p = B_a \varepsilon$.

Referring to (3.23), if $\dot{v}(x) < 0$ for any state $x \neq x_p$, the Lyapunov function $v(x)$ will ultimately lead the system state to converge to $x = x_p$. In this case, the state error stabilizes at a non-zero value rather than converging to zero. Consequently, the power-sharing ratio deviates from its predefined value, disrupting the expected power-sharing ratio. On the other hand, if $L x_p \neq B_a \varepsilon$ throughout the feasible domain, the Lyapunov function fails to converge to a new equilibrium point. As a result, both the active power and harmonic power are continuously affected by the FDIA signal, leading to sustained effects in the system's operation.

In summary, the presence of FDIA prevents proportional sharing of active and harmonic power as originally intended, compromising the microgrid's performance and stability.

When a communication disruption occurs in the network, the local controller cannot correctly receive information from its neighbors; the result is similar to a Dos attack but not manipulated by the hacker. It can be represented as:

$$x_{f,j} = \kappa_j^d x_j \quad (3.24)$$

where x_j and $x_{f,j}$ represent the original neighboring signal, and the signal arrives at the local controller, respectively. The binary variable $\kappa_j^d = 1$ represents a regular communication,

while $\kappa_j^d=0$ denotes the communication disruption between j th and i th DGs. In this section, it is assumed when the communication failure occurs, the received data from the neighbor is zero, which will contribute to an incorrect command on the local controller.

RESILIENCE ENHANCEMENT AND COMMUNICATION RELIEF

A resilient enhanced controller to mitigate cyber-attacks and communication disruption. As microgrid communication networks are complex and comprise numerous nodes with varying communication types, it is hypothesized that cyber-attacks and communication disruption targeting a selected inverter unit would not simultaneously disrupt all the communication channels through which it communicates with its neighboring nodes. Moreover, The previous section analyzes the communication dependency and identifies it as a challenge in the commutation-based approach. To address this issue, an auxiliary controller is proposed to relieve the communication, before which the virtual impedance has been appropriately modulated to facilitate optimal power-sharing performance.

With the proposed method, the resilient virtual impedance can be rewritten as (3.25).

$$Z_{c,i} = \int k_{v,i} \sum_{j \in N_i} a_{ij} [(1 - \Theta_{i,j}^I)(x_j - x_i) + \Theta_{i,j}^I \Delta x_{i,j}^*] dt \quad (3.25)$$

Herein, $\Delta x_{i,j} = x_j - x_i$, and $\Delta x_{i,j}^* = \min\{|\Delta x_{i,1}|, \dots, |\Delta x_{i,j}|\} \cdot \text{sgn}(\Delta x_{i,j})$, where $\text{sgn}(\cdot)$ represents the selected signal's sign, denoted as $\text{sgn}(z) = z/|z|$. The variable $\Theta_{i,j}^I$ is a binary indicator that denotes whether a cyber attack and communication disruption have occurred.

$$\Theta_{i,j}^I = \begin{cases} 1, & \text{if } |\Lambda_{i,j}^I| \geq Y_i^I \\ 0, & \text{else} \end{cases} \quad (3.26)$$

Here, we utilize $\Lambda_{i,j}^I$ to identify the presence of cyber attack and communication disruption. The variable $\Lambda_{i,j}^I$ represent the difference between the data from the neighbouring j th unit and the local state of i th unit, denoted as $\Lambda_{i,j}^I = a_{ij}(x_j - x_i)$. This identification can be expressed as shown in (3.26). Considering the general disturbance and measure noise, variable Y_i^I serves as the cyber attack and communication disruption measurements threshold and is defined as $Y_i^I = 0.01x_i$. Based on this definition, if $|\Lambda_{i,j}^I| \geq Y_i^I$, we conclude that there is a cyber attack or communication disruption and set $\Theta_{i,j}^I = 1$. Conversely, if $|\Lambda_{i,j}^I| < Y_i^I$, we determine that there is regular communication.

When confronted with FDIA, the neighbor's information is manipulated, introducing deliberate deviation. Differently, during instances of communication disruption, the neighbor's data is intentionally set to zero. This different character enables the system to distinguish between a potential cyberattack and a mere communication breakdown.

If a cyber attack or communication disruption occurs between the j th and i th DG units, a binary signal $\Theta_{i,j}^I$ is sent to the reconstructing controller, thereby, the corrupted communication link which is attacked, is replaced by a healthy signal reconstructed using $\Delta x_{i,j}^*$. This procedure benefits that the proposed communication-based strategy is resilience enhanced.

With the adopted undirected graph, the Laplacian disagreement function of the graph is defined as:

$$\Phi_{G(x)} = x^T Lx = \frac{1}{2} \sum_{j \in N_i} a_{ij} (x_j - x_i)^2. \quad (3.27)$$

In addition, the Laplacian matrix of the graph satisfies the following property:

$$\lambda_2(L) = \min_{x \neq 0, 1^T x = 0} \frac{x^T L x}{\|x\|^2} \quad (3.28)$$

where $\lambda_2(L)$ denotes the algebraic connectivity of the undirect graph, and a larger $\lambda_2(L)$ means stronger connectivity and a faster convergence speed.

Suppose the system is under cyber attack, and the signal on the communication link 2–1 is corrupted, as in Fig.3.6(a). As in Fig.3.6(b), from the reference, it is suggested to block the corrupted link, which may reduce algebraic connectivity. Remarkably, the proposed method shown in Fig.3.6(c) can benefit from greater algebraic connectivity by reconstructing the corrupted method compared to [27, 35]. This can be proved from the Laplace matrix $\lambda_2(L_b) < \lambda_2(L_c)$.

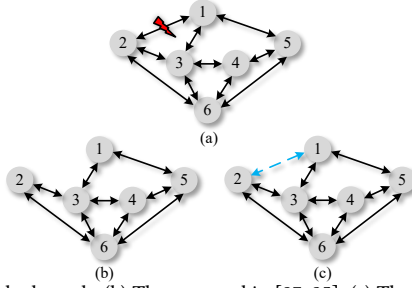


Figure 3.6: (a) The original attacked graph. (b) The proposal in [27, 35]. (c) The proposed method.

With the method, an auxiliary controller utilized to reduce the communication dependency by deactivating communication can be expressed as follows:

$$k_{v,i} = \begin{cases} 0, & \text{if } \Theta_{i,j}^I \cup \Theta_{i,2}^I \cdots \cup \Theta_{i,N}^I = 0 \\ k_{v,i}, & \text{else} \end{cases} \quad (3.29)$$

Assuming that the inverter system has been constructed by using the proposed method, it is expected that the sharing of harmonic and reactive power among all units will be proportional, thus satisfying the "steady state" requirements for all nodes $i \in N_i$ as denoted by $|\Lambda_{i,j}^I| < Y_i^I$. In such a scenario, the auxiliary controller is triggered, assigning a value of 0 to reshape factor, represented as $k_{v,i} = 0$. Consequently, the microgrid becomes independent of the communication network. In other words, the communication relief method implementation involves a two-step process. Initially, the DGs adjust the virtual impedance in response to disparities with their neighbors. Subsequently, the consistent maintenance of power-sharing is achieved by upholding a constant virtual impedance value. This eliminates the need for continual communication, even in case of load change and plug-and-play operation.

3.3.2 DISTRIBUTED VIRTUAL IMPEDANCE UNDER RESISTIVE FEEDER

Based on the last section, in order to investigate the resistive feeder and improve bus voltage quality while guaranteeing proportional harmonic power and active power sharing

in the resistance-dominated system, the distributed virtual impedance control is presented in this section. Fig.3.5 depicts the overall control block diagram, which primarily consists of the communication layer and the virtual impedance of the harmonic power sharing, active power sharing, and harmonic voltage compensation loops. By separately adaptively modulating the virtual impedance, the suggested solution reduces the requirement to identify the line impedance. It assumes that each unit needs to share information with the inverters close to it.

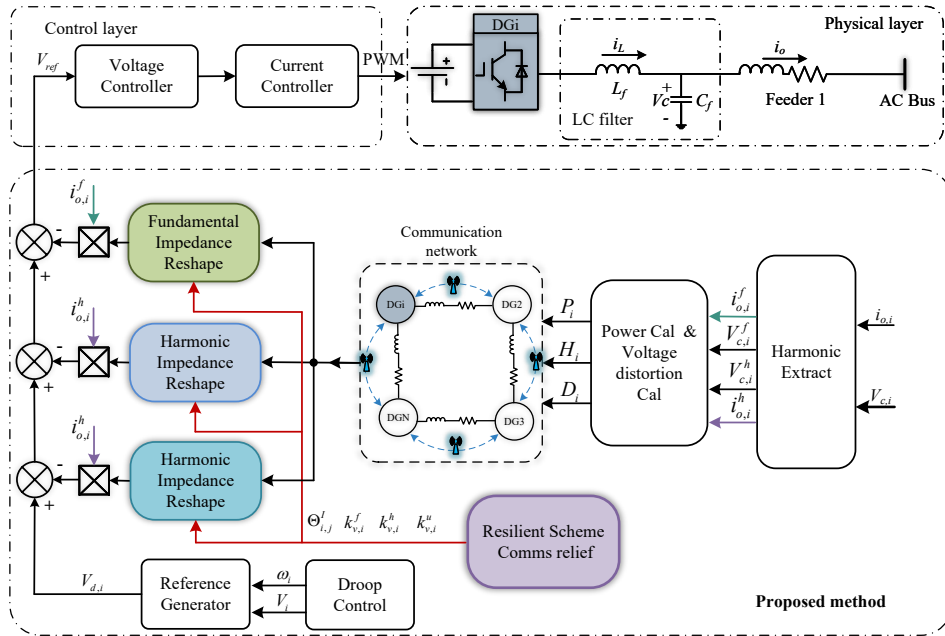


Figure 3.7: The proposed virtual impedance framework under resistive feeder.

CONSENSUS-LAW BASED VIRTUAL IMPEDANCE FOR RDF

In Fig.3.7, the participating inverters use the communication network to transmit information about active power (m_1P_1, \dots, m_nP_n), harmonic power (b_1H_1, \dots, b_nH_n) and bus voltage distortion rate (D_1, \dots, D_n). Additionally, as was previously noted, reasonable harmonic power sharing cannot match the properly active power sharing and the desired bus voltage quality. Therefore, independent design is required for the active power sharing controller, harmonic sharing controller, and bus voltage compensation controller. The active power controller is established as (3.30).

$$Z_{v,i}^f = k_{v,i}^f \int [\sum_{j \in N_i} a_{ij}(m_iP_i - m_jP_j)] dt \tag{3.30}$$

The virtual impedance introduced in (3.31) can be used to share the harmonic power

properly.

$$Z_{v,i}^h = k_{v,i}^h \int [\sum_{j \in Ni} a_{ij}(b_i H_i - b_j H_j)] dt \quad (3.31)$$

Unlikely in [45], decreasing the overall impedance for PCC voltage quality improvement, which potentially causes instability, we have implemented a voltage compensation loop. The bus harmonic voltage compensation controller is written as (3.32).

$$Z_{v,i}^u = k_{v,i}^u \int [\sum_{j \in Ni} a_{ij}(D_j - D_i) + g_i(D_0 - D_i)] dt \quad (3.32)$$

The loop gain $g_i=1$ is a pinning gain for the harmonic voltage compensation controller. $k_{v,i}^f$, $k_{v,i}^h$ and $k_{v,i}^u$ are the impedance reshaping factors for active power sharing, harmonic power sharing, and harmonic voltage compensation, respectively. The D_0 is the maximum allowable harmonic voltage distortion rate. D_i denotes the h th order harmonic distortion of i th unit as (3.33).

$$D_i = \frac{V_i^h}{V_i^f} \quad (3.33)$$

In Fig.3.7, V_i^f and V_i^h represent the fundamental voltage and h -th harmonic voltage, respectively. It is worth noting that the capacitor voltage is used in place of the PCC voltage due to the small line impedance in low-voltage grids. If the harmonic voltage exceeds the permissible distortion limits or the active and harmonic power may not be shared correctly, the virtual impedance is automatically adjusted to be the desired value in such a scenario.

With the virtual impedance reshaping loops, the voltage reference of the double-loop voltage controller is obtained as (3.34):

$$V_{ref} = V_d - Z_v^f i_o^f - Z_v^h i_o^h - Z_v^u i_o^u \quad (3.34)$$

It should be noted that excessively low virtual impedance can lead to unstable operation due to the potential occurrence of circulating current among the inverters involved. Meanwhile, an excessively high virtual impedance can result in poor PCC voltage quality. This study's overall impedance encompasses the line impedance, output impedance, and virtual impedance. The initial impedance is predetermined once the system is established, and they typically exhibit relatively large initial values. Consequently, the adaptive virtual impedance is adjusted to compensate for the initial impedance. It is worth noting that even if the virtual impedance has a negative value, the overall impedance will still be positive and sufficiently large to ensure the system's stability. Furthermore, the feeder investigated in this section is primarily resistive, employing a resistive virtual impedance. Unlike inductive scenarios, this characteristic contributes to the system's enhanced stability as it avoids differential terms. Furthermore, when the sum of the output impedance and line impedance becomes negligibly small, it becomes necessary to introduce an additional fixed virtual impedance to maintain a sufficiently substantial initial impedance, thus preserving system stability [78].

RESILIENCE ENHANCEMENT AND COMMUNICATION RELIEF

In addition, we propose a resilient enhanced auxiliary controller to suppress cyber-attacks by blocking the corrupted link.

The proposed resilience scheme for mitigating cyber attacks that impede virtual impedance convergence can be rewritten as (3.35).

$$Z_{v,i} = k_{v,i} \int \sum_{j \in N_i} a_{ij} \Delta \delta'_{i,j} dt \quad (3.35)$$

where $Z_{v,i}$, $k_{v,i}$ and x_i represent the virtual impedance, reshape factor and state variable in (3.30), (3.31) and (3.32).

If we take $\Delta \delta_{i,j} = x_j - x_i$. $\Delta \delta'_{i,j}$ can be taken as follows to block the original data:

$$\Delta \delta'_{i,j} = (1 - \Theta_{i,j}^I) \Delta \delta_{i,j} \quad (3.36)$$

where $\Theta_{i,j}^I$ is a binary variable representing the presence or absence of a cyber attack, as defined in (3.26).

In this case, if a cyber attack occurs between the j th DG unit and i th DG unit, the binary signal $\Theta_{i,j}^I$ is sent to isolate the corrupted data; thus, the infected data is disregarded. Consequently, the proposed communication-based strategy is immune to cyber-attacks with the procedure in the resilient framework.

For a resistive feeder microgrid, the auxiliary controller described in (3.29) can also be used to disable the proposed method, thereby reducing the communication burden. In the absence of a cyber attack, the reshape factors $k_{v,i}$ determine the convergence speed of the outer loop. Increasing these factors improves communication efficiency among the inverters. However, for the virtual impedance loop, the reshape factors should be set to ensure a slower response compared to the inner loop. Moreover, since virtual impedance is calculated based on power, it converges even slower than the power loop. To achieve this, given that the cutoff angular frequency of the power loop filter is set at 100 rad/s, the reshape factors are chosen as 0.02.

Once the inverter system is established using the proposed method, it is assumed that harmonic and active power can be proportionally shared along with harmonic voltage within an acceptable range. In this scenario, the auxiliary controller is activated, resulting in the impedance reshaping factor $k_{v,i} = 0$, making the microgrid independent of communication.

3.4 THE DISTRIBUTED MODEL PREDICTIVE CONTROL

Secondary control in microgrids typically includes power control and voltage control. While extensive research [64, 67] has focused on voltage frequency and amplitude control using MPC-based methods, this section shifts the focus to power-sharing control by utilizing DMPC. The proposed structure is illustrated in Fig.3.8, structured into four distinct parts: the primary control layer, the distributed model predictive control optimize layer, the virtual impedance layer, and the communication layer. The primary control layer adopts the droop control. The distributed model predictive control is composed of a state observer for power regulation, predictive control, and cost function, and it is used to predict the

3.4.2 DISCRETE TIME MODELS

To obtain estimates of active power and harmonic power, we derive a discrete model from equations (3.37)-(3.41) using the forward Euler method. Given integrators are linked at the output port of the predictive controllers to ensure zero steady-state error. We apply the incremental operator ($\Delta x(k) = [x(k) - x(k-1)]$) as described in equations (3.43)-(3.45). Consequently, the optimization problem is formulated as a function of the variations in control actions ($Z_{v,i}^f, Z_{v,i}^h$).

$$P_i(k+1) = P_i(k) + [V_{c,i}^f(k+1) - V_{c,i}^f(k)]B_i^f \Lambda_i \quad (3.42)$$

where $\Lambda_i = 2V_{c,i}^f(k) - V_{bus}^f(k)$. The dynamic state of bus voltage V_{bus}^f is ignored. Thus, an approximate first-order dynamic model of (3.37) can be discrete as (3.42). The discrete model of (3.38) and (3.39) correspond to (3.43) and (3.44), respectively.

$$\Delta V_{c,i}^f(k+1) = \Delta V_{d,i}(k+1) - i_{o,i}^f(k) \Delta Z_{v,i}^f(k) \quad (3.43)$$

$$V_{d,i}(k+1) = V_{d,i}(k) - m_i [P_i(k+1) - P_i(k)] \quad (3.44)$$

Similarly, the dynamic state of V_{bus}^h is ignored; therefore, (3.40)-(3.41) can be discrete as (3.45)-(3.46).

$$H_i^h(k+1) = H_i^h(k) - B_i^h V_{c,i}^f(k) [V_{c,i}^h(k+1) - V_{c,i}^h(k)] \quad (3.45)$$

$$V_{c,i}^h(k+1) = V_{c,i}^h(k) + i_{o,i}^h(k) \Delta Z_{v,i}^h(k) \quad (3.46)$$

It should be noted that there are prediction errors in these models. For instance, both the dynamic models presented in (3.42) and (3.45) neglect to consider the dynamics of the bus voltage $V_{bus}^f(k)$, $V_{bus}^h(k)$, both of which are influenced by the interconnections among distributed generators. Nonetheless, these prediction errors do not exert a substantial impact on overall system performance when employing the proposed DMPC. This can be elucidated since the prediction errors at the current time step do not accumulate to affect subsequent time steps in MPC, where only the first step data is used for every calculated cycle. Furthermore, the output of the predictive algorithm provides the derivative of the calculated virtual impedance. In essence, the prediction errors only influence the virtual impedance change rate during dynamic processes. With the integrator, these errors are gradually eliminated as the system approaches a steady state, ultimately achieving accurate power sharing.

3.4.3 STATE OBSERVER

The expressions of the dynamic average estimation for active power and harmonic power, which are the reference for the DMPC controller, are given in equations (3.47) and (3.48), respectively, where $\delta_i^p = m_i P_i$, $\phi_i^h = b_i H_i$, denoting the power-sharing coefficient. They are computed exclusively based on local measurements and information communicated from other generators. The adjacency term a_{ij} regulates communication.

$$\bar{\delta}_i^p(t) = \delta_i^p(t) + \int_0^t \sum_{j \in N_i} a_{ij} [\bar{\delta}_j^p(\tau) - \bar{\delta}_i^p(\tau)] \quad (3.47)$$

$$\bar{\varphi}_i^h(t) = \varphi_i^h(t) + \int_0^t \sum_{j \in N_i} a_{ij} [\bar{\varphi}_j^h(\tau) - \bar{\varphi}_i^h(\tau)] \quad (3.48)$$

The operational constraints encompass a set of inequalities designed to guarantee that the performance of the distributed generators remains within physically feasible limits. This particular set of constraints is articulated in equations (3.49) and (3.50). These constraints ensure the virtual impedance is maintained within an appropriate range. When the virtual impedance exceeds the threshold, it can adversely affect the bus voltage. Conversely, if the virtual impedance is too low, it may render the system unstable. Specifically, [79] suggests the secure fundamental voltage band is 0.88 to 1.1 p.u. of its nominal value. This can derive the upper bound of the virtual fundamental impedance. Meanwhile, the PCC harmonic voltage disordered rate is below 5%, which complies with the IEEE 519-1992 standard harmonic distortion rate restriction [80]. This restriction can derive the upper bound of the virtual harmonic impedance. While the lower bound of the virtual fundamental and harmonic impedance should be larger than zero to avoid the circular current of the involved DGs.

$$Z_{v,i,min}^f(k) \leq Z_{v,i}^f \leq Z_{v,i,max}^f(k) \quad (3.49)$$

$$Z_{v,i,min}^h(k) \leq Z_{v,i}^h \leq Z_{v,i,max}^h(k) \quad (3.50)$$

3.4.4 COST FUNCTION

The output of DMPC is determined by a multi-objective cost function (3.51), which is constructed from four terms, each representing a control objective in the microgrid. Here, two terms (3.52) and (3.53) describe the average active power and harmonic power sharing control. While the optimization problem is local for every DG, the control is global for the whole microgrid since they are based on predictions transmitted by communicating. The third and fourth terms (3.54) and (3.55) are used to minimize the control operations that are needed to match the goals. η_i represents the weighting coefficient. Since the automatic parameter selection of MPC is out of the scope of this research, the trial-and-error method is adopted in this section, which considers the power control loop's response speed requirements.

$$\min J_i(k) = J_i^P(k) + J_i^H(k) + J_i^{zf}(k) + J_i^{zh}(k) \quad (3.51)$$

$$J_i^P(k) = \eta_i^p [\bar{\delta}_i^p(k+1) - \delta_i^p(k+1)]^2 \quad (3.52)$$

$$J_i^H(k) = \eta_i^h [\bar{\varphi}_i^h(k+1) - \varphi_i^h(k+1)]^2 \quad (3.53)$$

$$J_i^{zf}(k) = \eta_i^{zf} [\Delta Z_{v,i}^f(k)]^2 \quad (3.54)$$

$$J_i^{zh}(k) = \eta_i^{zh} [\Delta Z_{v,i}^h(k)]^2 \quad (3.55)$$

3.4.5 RELIEF TO COMMUNICATION ISSUES

CONVERGE ANALYSIS

It's worth noting that (3.47) and (3.48), which establish the averages for active power and harmonic power, incorporate the parameter a_{ij} , which indicates necessary communication between the relevant inverters. Besides, the adoption of DMPC imposes computation

requirements. Herein, the average estimation can be simplified as (3.56). The local unit i estimates the average value of the system x_i by the local state and the neighbor's state \bar{x}_j . Then, \bar{x}_i is fed to the MPC optimizer as the reference.

$$\bar{x}_i(t) = x_i(t) + \int_0^t \sum_{j \in N_i} a_{ij} [\bar{x}_j(\tau) - \bar{x}_i(\tau)] \quad (3.56)$$

The microgrid global dynamics can be formulated as (3.57)

$$\dot{\bar{X}} = \dot{X} - L\bar{X} \quad (3.57)$$

where $X = [x_1, x_2, \dots, x_n]^T$ denotes the measurements of the local units. $\bar{X} = [\bar{x}_1, \bar{x}_2, \dots, \bar{x}_n]^T$ represents the estimated global average state of all involved units. It can also be represented as (3.58).

$$s\bar{X} - \bar{X}(0) = sX - X(0) - L\bar{X} \quad (3.58)$$

where \bar{X} and X are the Laplace transforms of \bar{X} and X , respectively. As shown in (3.56), $\bar{X}(0) = X(0)$. The system state can be represented as (3.59).

$$\bar{X} = s(sI_N + L)^{-1}X = G_{obs}X \quad (3.59)$$

where the G_{obs} is the observer transfer function. It is reported that in an undirected graph, all the participated inverters will converge to the average value of the system [81]. It's denoted as (3.60).

$$\bar{X}^{ss} = M \times \lim_{t \rightarrow \infty} X(t) = MX^{ss} \quad (3.60)$$

where $M \in \mathbb{R}^{N \times N}$ is the averaging matrix, with all of the elements are all equal to $1/N$. X^{ss} means the steady-state value of the state.

COMMUNICATION DELAY ANALYSIS

Based on the dynamic average estimation in (3.56), when considering the communication delay, it can be expressed as (3.61).

$$\dot{\bar{x}}_i(t) = \dot{x}_i(t) + \sum_{j \in N_i} a_{ij} [\bar{x}_j(t - t_a) - \bar{x}_i(t - t_l)] \quad (3.61)$$

where t_a is the neighbor's data delay, and t_l is the local measurement delay. It is stated that this dynamic averaging algorithm achieves global consensus even under communication delay. This proof is omitted for brevity, as it was done in [82].

COMMUNICATION FAILURE ANALYSIS

In case of communication failure in the processing of the neighbor's information transfer, the data propagated through this communication link is falsified to be zero, which deteriorates the power-sharing performance. However, it is expected that under normal operating conditions, active power and harmonic power should not assume zero values. This contributes to distinguishing communication failure.

$$a_{ij}^e(k) = \begin{cases} 1 & \text{non-zero data from DG}_j \text{ reaches DG}_i \\ 0 & \text{no data from DG}_j \text{ arrive at DG}_i \\ 0 & \text{data from DG}_j \text{ to DG}_i \text{ is zero} \\ 0 & j = i \end{cases} \quad (3.62)$$

To minimize both communication and computational load, we propose a trigger condition for determining when to deactivate the communication network and MPC computations. Specifically, in (3.63), the parameter Γ^D is introduced to indicate the deactivation of the prediction algorithm and the state observer. This is achieved by setting associate elements of the adjacency matrix A to zero, effectively isolating the system from network interactions. The effect of Γ^D is similar to the loop gain $k_{v,i}$ in (3.29), which governs communication-related dynamics. However, Γ^D extends its influence to include both the MPC optimizer and the state observer, whereas $k_{v,i}$ is confined to managing communication.

When $\Gamma^D = 1$, it signifies that the system has reached a state of sufficient adaptation, rendering neighbor state information redundant. In this condition, propagating information through the communication network and MPC optimization are no longer necessary, as the virtual impedance achieves complete autonomy. This state ensures the system's functionality is maintained independently of the communication network and MPC computations, significantly reducing operational complexity and resource utilization.

$$\Gamma^D = \begin{cases} 1, & \text{if } \Theta_1^D \cap \Theta_2^D \dots \cap \Theta_n^D = 1 \\ 0, & \text{else} \end{cases} \quad (3.63)$$

where Θ_i^D assumes a binary value, representing the if the virtual impedance is appropriately set. Referring to (3.47) and (3.48), if the average power approximates the measured power, it signifies that power sharing is indeed proportionate, where the communication network and MPC can be disabled. To mitigate the potential influence of measurement noise, which can lead to minor power fluctuations, we introduce the condition that $\Theta_i^D = 1$, if the expression $[\bar{x}_i(k) - x_i(k)]/x_i(k) \leq 1\%$ hold true. Or else, Θ_i^D is set to 0.

3.5 EXPERIMENT RESULTS

The efficacy of the proposed adaptive control strategy has been verified through experiments conducted on a distributed AC microgrid consisting of three parallel-connected inverters. The system parameters are provided in Table 3.3. The experimental setup is illustrated in Fig.2.4.

Table 3.3: Parameters of the microgrid for experiment verification.

Symbol	Interpretation	Value
U_{dc}	DC-link voltage	150V
Z_L	Line impedance	2.2 mH
L_f	Inductor of LC filter	2.2 mH
C_f	Capacitor of LC filter	12 μ F
f_s	Switch frequency	20kHz
m_1, n_1	droop coefficient of DG1	1/1000
m_2, n_2	droop coefficient of DG2	1/2000
m_3, n_3	droop coefficient of DG3	1/3000
$k_{v,i}^f$	fundamental impedance reshape factor	0.001
$k_{v,i}^h$	harmonic impedance reshape factor	0.001
ω_0	Nominal angular frequency	314rad/s
V_0	Nominal voltage amplitude	110V

3.5.1 THE PROPOSED DVI UNDER IDF VERIFICATION

In this section, the 3rd harmonic is taken to validate the performance of the harmonic control, and the harmonics and reactive power output of the inverters follow the maximum power ratio, which is set to 1:2:3. To verify the effectiveness of the proposed method, experiments are conducted under several scenarios. The test procedures for the main cases are illustrated in Fig.3.9.

Case A: Investigating the performance of power-sharing mechanisms before and after implementing the proposed communication-based virtual impedance; evaluating the system’s ability to immunize the effects of communication delays and disruption; Validating the benefits of the proposed control under communication disruption with a comparative study; Verifying the robustness of the resilient control to load variations.

Case B: Exploring the potential effects of cyber attacks on power-sharing and assessing how the proposed defense mechanism can mitigate these effects.

Case C: A comparative study with two recent studies is conducted to demonstrate the benefits of this section’s power-sharing performance and plug-and-play capability in no-communication situations. Based on the experimental setup shown in Fig.2.4 and the

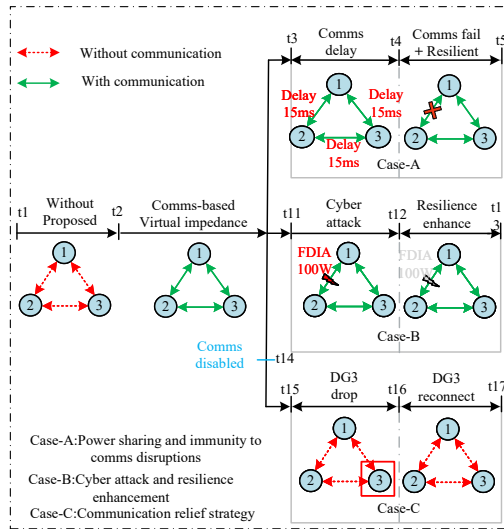


Figure 3.9: Experimental procedure for the IDF microgrid.

proposed adaptive control scheme, we have conducted several experiments with different operations in Fig.3.9 to evaluate the effectiveness of our approach.

Notably, connecting all units to the microgrid may require a significant amount of time, during which a cyber attack may occur through the communication line. Therefore, we consider mitigating cyber attacks and relieving communication burdens simultaneously. Subsequently, disabling the communication once all inverters are connected and proportional share power may alleviate communication dependency and reduce the risk of further cyber attacks and communication disruption.

POWER SHARING UNDER COMMUNICATION DISRUPTIONS

Initially, as shown in Fig.3.10(a) and (b) during the $t1-t2$ stage, reactive and harmonic power sharing is inaccurate due to mismatched droop coefficients and line impedance. It should be noted that the different droop coefficient only affects the fundamental impedance. In contrast, the other control parameters, along with line impedance, remain the same, resulting in the sharing of harmonic power in a 1:1:1 ratio.

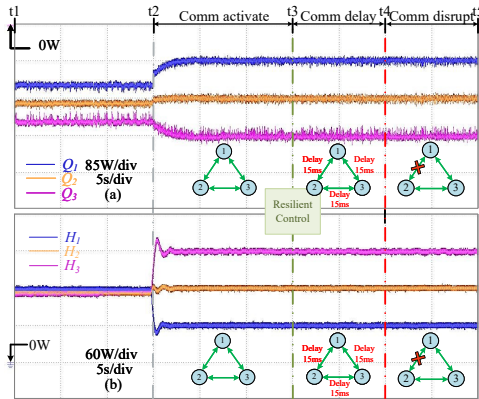


Figure 3.10: Power sharing performance of the proposed controller: (a) Reactive power. (b) 3^{rd} harmonic power.

Subsequently, with the activation of the virtual impedance at $t2$, proportional sharing of reactive and harmonic power is achievable, regardless of the initial condition. Remarkably, at $t3$, the resilient control is enabled, and the power-sharing performance remains unaffected, despite a communication delay of 15ms and communication loss imposed on the communication link from $DG2$ to $DG1$ at $t3$ and $t4$, respectively.

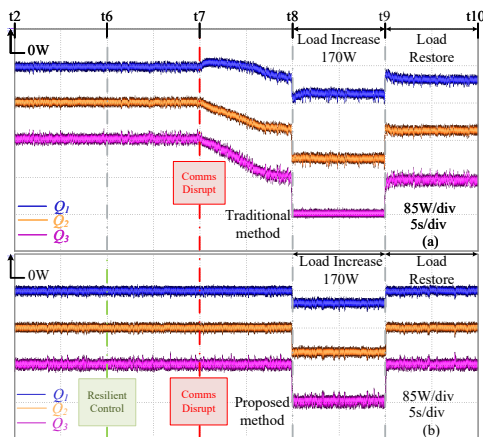


Figure 3.11: Comparison of reactive power performance with different strategies under communication disruption. (a) The distributed virtual impedance control in [32]. (b) The proposed resilient method.

A comparison study with [32] under the communication disruption scenario is illustrated in Fig.3.11. In Fig.3.11(a), the influence of a communication interruption on the output reactive power is visible when applying the virtual impedance proposed in [32]. Specifically, at t_7 , the communication link 3-1 experiences an interruption, resulting in a distortion of the reactive power, subsequently affecting the load switch operation. By contrast, Fig.3.11(b) shows that the proposed method exhibits improved resilience to communication disruption. Resilient control is activated at t_6 in this case, ensuring that reactive power performance stays unaffected by the communication disruption at t_7 . Moreover, during load fluctuations at t_8 and t_9 , where the load increases by 170W and then recovers, the power-sharing ratio remains consistently maintained. This indicates that the suggested resilient control will not degrade the operation of the microgrid during the load change.

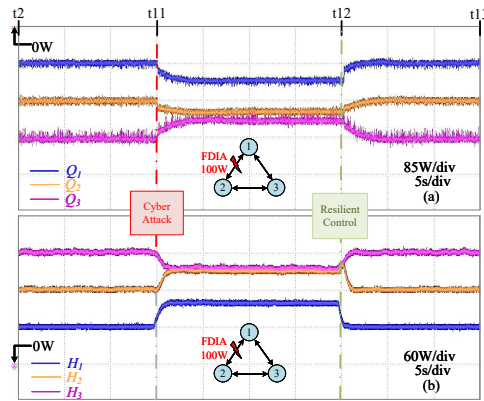


Figure 3.12: Effect of cyber attack and the resilient controller. (a) Reactive power. (b) 3^{rd} harmonic power.

TEST OF RESILIENCE

Fig.3.12(a) and (b) illustrate the effects of cyber attacks as well as the efficacy of the suggested approach for mitigating such attacks. During the t_2 - t_{11} stages, the communication-based virtual impedance is employed. This allows an appropriate distribution of reactive power and harmonic power, and there is no cyber attack on the communication network during this period. Then, the communication channel from DG_2 to DG_1 is attacked by a false data injection attack with $\epsilon(t) = 100$ W for the reactive power and harmonic power controllers at t_{11} . Consequently, the power-sharing ratio moves away from the optimum value. At t_{12} , the suggested resilient framework is activated, removing the distorted data and reconstructing the attacked signal, thereby restoring the power-sharing ratio to 1:2:3. The findings exhibit the proposed approach's resilience to cyber-attacks.

TEST OF COMMUNICATION RELIEF

As stated, the proposed methodology can potentially reduce the communication dependency by deactivating the communication network once all participating inverters are connected and properly adjusted when the reactive and harmonic power can be shared accurately. The figures presented in Fig.3.13 demonstrate that the proposed control method featuring a communication relief strategy outperforms several recent studies.

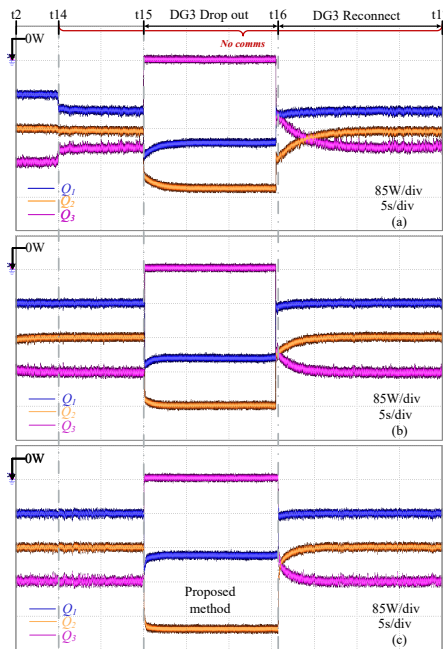


Figure 3.13: Comparison of plug-and-play operation with different controls without communication. (a) Virtual impedance in [32, 55, 61]. (b) Voltage compensation method in [27, 35]. (c) The proposed method.

Fig.3.13 (a) and (b) showcase the reactive power performance of the distributed method in [32, 55, 61] and [27, 35] in no communication scenario, respectively. Meanwhile, Fig.3.13 (c) depicts the reactive power employing the proposed method under the same circumstances.

Notably, the communication network is deactivated at t_{14} , before which distributed control loops are employed to facilitate power-sharing. During the subsequent period from t_{14} to t_{15} , as the communication is disabled, the distributed virtual impedance in [32, 55, 61] promptly loses its effectiveness, resulting in an improper in the power-sharing ratio, which deviates from the expected 1:2:3 distribution. Furthermore, the plug-and-play test in this period becomes unreliable. At t_{15} , as depicted in Fig.3.13(b), (c), and (d), when $DG3$ is unplugged, the method presented in [27, 35] fails to ensure that operational $DG1$ and $DG2$ share reactive power in an accurate 1:2 ratio. The system only promises the desired power-sharing ratio upon the reconnection of $DG3$. This underscores the reliance of the two aforementioned methods on continuous communication networks for seamless plug-and-play operation. In contrast, the proposed method, from t_{14} to t_{17} , maintains a stable expected power-sharing ratio among the participating inverters without the need for continuous communication. This is achieved through an appropriately adjusted and pre-fixed virtual impedance. Consequently, Fig.3.13 demonstrates that the proposed control method imposes significantly lower communication demands than the above two existing methods.

3.5.2 THE PROPOSED DVI UNDER RDF VERIFICATION

The proposed adaptive control under a resistance-dominated feeder has been tested in experiments of a distributed AC microgrid with three inverters connected in parallel to validate its effectiveness, as shown in Fig.2.4. Following the structure in Fig.2.4, several cases are carried out in this section to verify the effectiveness of the proposed adaptive control scheme with different operations. The plant and control parameters of the microgrid are provided in Table 3.3. Notably, the feeder impedance was adjusted from $2.2mH$ to 0.5Ω for resistive feeder verification.

In this section, the 3^{rd} harmonic is still selected as an example for verifying. The inverters' output harmonic and active power rate follows the maximum capacity proportion set as 1:2:3. The PCC harmonic voltage distorted rate is below 5%, which complies with the IEEE 519-1992 standard harmonic distortion rate restriction [80].

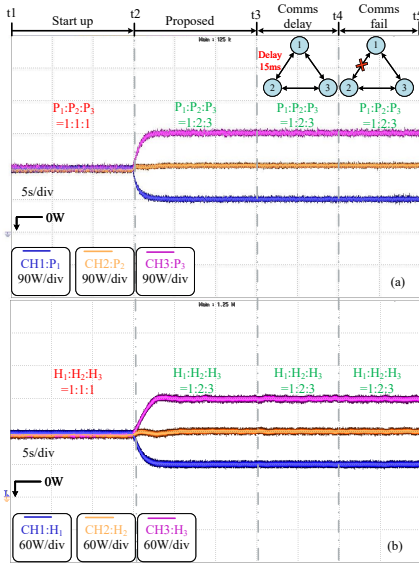


Figure 3.14: Performance of the proposed controller: (a) Active power. (b) 3^{rd} harmonic power.

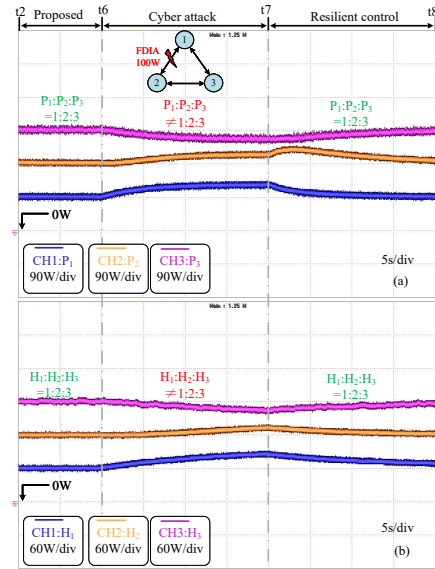


Figure 3.15: Performance of the resilient controller: (a) Active power. (b) 3^{rd} harmonic power.

ACTIVE AND HARMONIC POWER SHARING

Fig.3.14 illustrates the performance of the proposed method. Initially, as shown in Fig.3.14 (a) and (b), conventional droop control is used to regulate the microgrids after the system starts at t_1 , resulting in an improper power-sharing ratio of 1:1:1. At t_2 , the proposed adaptive virtual impedance is activated, contribute to a proportional sharing of active power and 3^{rd} harmonic power with the desired ratio of 1:2:3. The effectiveness of the proposed communication-based virtual impedance is further demonstrated by intentionally imposing communication delays ($15ms$) and interruptions in the communication link from DG_2 to DG_1 at t_3 and t_4 , respectively. Despite these disruptions, the system response exhibits no significant changes during these periods, confirming the proposed method's immunity

to communication delays and interruptions. The determination of an upper bound on communication delay can be achieved through the utilization of Riccati equation-based analysis, as detail demonstrated in [56]. Consequently, the time delay specified in this study amounts to 15ms for the network. However, since the delay analysis is not the main contribution of this section and in the interest of brevity, this analysis has been omitted from the thesis.

CYBER ATTACK AND RESILIENCE ENHANCEMENT

Fig.3.15 (a) and (b) demonstrate the impact of cyber attacks on microgrids and the effectiveness of the proposed method in mitigating such attacks. In the t2-t6 stage, the adaptive virtual impedance is adopted. Therefore, the active and harmonic power can be proportional sharing, and there is no cyber attack in the communication network. Subsequently, the communication line from *DG2* to *DG1* is subject to a false data injection attack with $\epsilon(t) = 100W$ for both active power and harmonic power controllers at t6. As a result, the power-sharing ratio deviates from the optimal point. At t7, the proposed resilient framework is activated, eliminating the corrupted data and recovering the power-sharing ratio to 1:2:3. The results demonstrate the resilience of the proposed method against cyber-attacks, highlighting its potential for enhancing the security and stability of microgrids.

COMMUNICATION RELIEF STRATEGY

The limited communication resource constraints the wide use of distributed control. This section proposes a communication relief control to alleviate the communication burden by disabling the communication-based virtual impedance after the system is built up. Moreover, it is necessary to keep sharing accuracy among the operational units when one DG unit drops. This section tests the active and harmonic power in the plug-and-play operation after the communication-based method exits. Fig.3.16(a),(b) show the performance of active power and fundamental current, while where Fig.3.17(a),(b) show the performance of harmonic power and 3rd harmonic current, respectively.

As shown in Fig.3.16(a) and Fig.3.17(a), the communication-based control strategy terminates at t9, allowing the active and harmonic power to continue to be shared proportionally without communication support. Before t9, the inverter was regulated by the proposed communication-based virtual impedance. At t10, *DG3* disconnects, while the operational *DG1* and *DG2* maintain a power-sharing ratio of 1:2. At t12, *DG2* drops out, and the operational *DG1* and *DG3* maintain a power-sharing ratio of 1:3. In both cases, the system operates reliably and accurately without the need for communication-based control. During periods t11-t12 and t13-t14, the disconnected unit is reconnected, and the system returns to its original configuration with proportional power-sharing.

The fundamental waveform in Fig.3.16(b) demonstrates consistent and accurate fundamental current sharing throughout the operation. Fig.3.17(b) presents the 3rd harmonic current of two dynamic processes. 1) when *DG3* drop out at t9, the harmonic current sharing ratio is changed from 1:2:3 to 1:2:0 among *DG1*:*DG2*:*DG3*. 2) when *DG3* is reconnected to the microgrid at t10. the harmonic output current of *DG3* is increased and, eventually, keeps proportional sharing among the involved inverter.

Following the information exchange during the build-up stage via the communication network, the virtual impedance is modulated to the desired value and remains constant during the whole process due to the integrator effect of the proposed method. As a result,

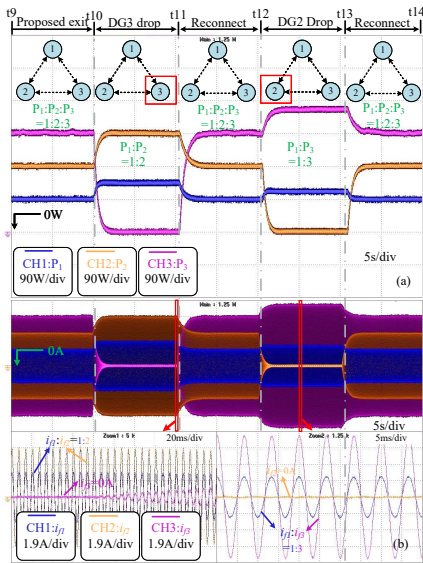


Figure 3.16: The plug-and-play operation for the active power controller after communication is disabled: (a) Active power. (b) Fundamental current.

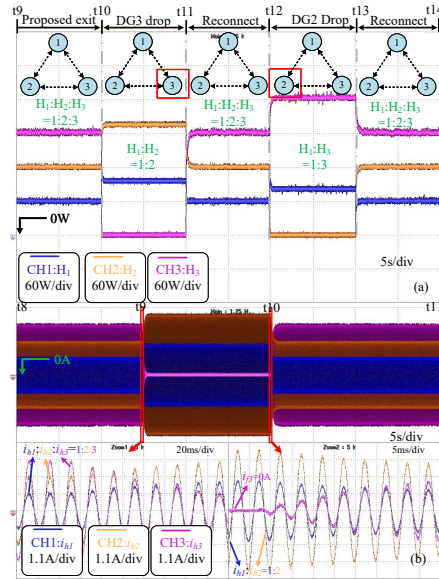


Figure 3.17: The plug-and-play operation for the harmonic controller after communication is disabled: (a) 3^{rd} harmonic power. (b) 3^{rd} harmonic current.

even when the communication network is disabled, the active and harmonic power can still be proportionally shared, and importantly, the microgrid remains the plug-and-play operation at this stage.

HARMONIC VOLTAGE COMPENSATION

To evaluate the effectiveness of the proposed control for compensating harmonic voltage distort rate and the sensitivity of PCC harmonic voltage with respect to virtual impedance, a comparison is developed between the waveforms obtained before and after the implementation of the proposed method, as illustrated in Fig.3.18. In the t1-t15 stage, the harmonic distortion rate, represented by D , is 10%, with the fundamental voltage measured at 98V and the 3^{rd} harmonic voltage at 10V. Subsequently, at t15, the proposed method is employed, attenuating the 3^{rd} harmonic impedance. Consequently, the harmonic distortion rate D decreases to 5%, the 3^{rd} harmonic voltage shifts to 5V, while the fundamental voltage remains unchanged, which validates the effectiveness of the proposed method for harmonic voltage mitigation.

As elaborated in Section II, PCC harmonic voltage exhibits a positive relationship with virtual impedance, as shown in Fig.3.18(b). Therefore, the reduction in harmonic impedance of the involved inverters leads to a decrease in the distorted rate of harmonic voltage as the drop in harmonic voltage diminishes.

COMPARATIVE STUDY

To illustrate the advantages of the proposed method in this section, a comparative analysis was conducted, as depicted in Fig.3.19 and Fig.3.20, showcasing the active power

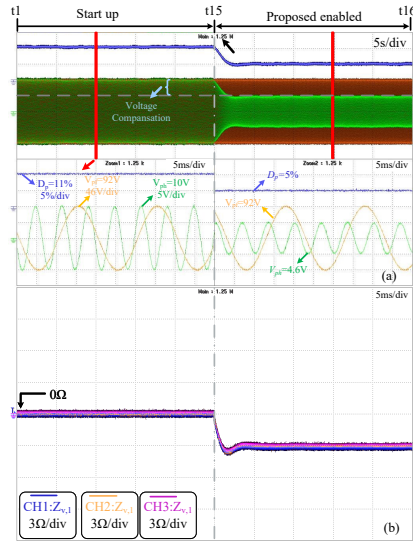


Figure 3.18: The validity of PCC harmonic voltage compensation:(a) PCC voltage. (b) Virtual impedance waveform.

performance.

Fig.3.19 illustrates the active power performance when the communication link fails using the secondary method introduced in [32, 61]. After activating the secondary control mechanism at time t_2 , the power-sharing ratio transitioned from 1:1:1 to 1:2:3. At t_4 , a communication failure occurs within the 2-1 link, inducing a disordered power reference signal and system power output. It should be noted that the persistent steady-state condition observed during the communication failure is attributable to constraints imposed on the system output to protect the experimental setup. Although the power-sharing ratio remains 1:2:3 during this period, the output power is reduced. As indicated in Fig.3.14 and Fig.3.19, it becomes evident that utilizing the secondary control approach proposed in [32, 61] potentially gives rise to power distortions under communication failure scenarios. This distortion, however, can be eliminated by applying the proposed virtual impedance method introduced in this section.

Fig.3.20 indicates the active power performance with the secondary control introduced in [33, 35], under the communication link disabled. It is worth noting that during the period from t_{10} to t_{11} , DG3 drops out, resulting in an active power allocation ratio between DG1 and DG2 inconsistent with the expected 1:2 ratio. In addition, in another period, t_{12} - t_{13} , DG2 drops out, and the active power-sharing correlation between DG1 and DG3 deviates from the expected 1:3 ratio. This illustrates the necessary role of communication in the secondary control described in [33, 35], which imposes a heavy communication burden on the microgrid system. In contrast, the proposed novel approach in this manuscript alleviates the communication burden since the microgrid keeps plug-and-play operation even without communication, as evidenced by the study results in Fig.3.16 and Fig.3.17.

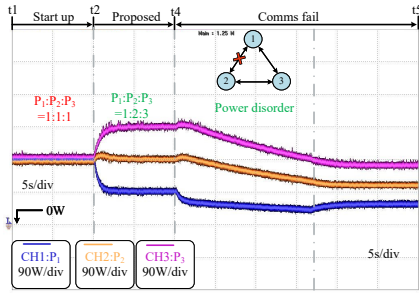


Figure 3.19: Active power sharing performance with the method in [32, 61].

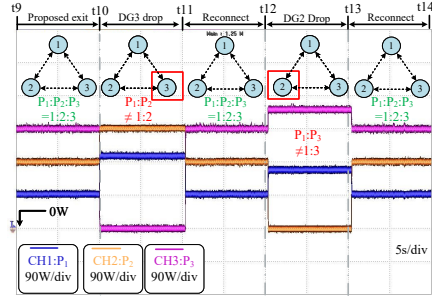


Figure 3.20: Active power sharing performance with the method in [33, 35].

3.5.3 THE PROPOSED DMPC-BASED VIRTUAL IMPEDANCE VERIFICATION

This section presents simulations and experiments to validate the effectiveness of the proposed DMPC-based virtual impedance under a resistive feeder. A comparative study is also included to highlight the advantages of the proposed method over existing approaches.

SIMULATION EVALUATION

To demonstrate the superiority of the proposed method over existing methods, a three-inverter connected system is developed by Matlab/Simulink as depicted in Fig.2.4. In the setup, the output port of the converter is linked to the AC bus through a resistive feeder impedance ($Z_L=0.5\Omega$) and an LC filter ($C_f=12\mu F, L_f=2.2mH$).

Following the structure in Fig.2.4, the microgrid plant and controller parameters for simulation are presented in Table 3.3. Similarly, the third harmonic (3^{rd}) is selected for this study. It should be noted that both inverters' output harmonic and active power ratios adhere to the maximum capacity proportion set at 1:2:3. It is important to note that this ratio is variable and can take any values. Consequently, we can devise an appropriate control methodology to accommodate the expected power-sharing ratio values.

Fig.3.21 provides a comprehensive investigation of the performance of active power sharing with different communication delays using the proposed method. Secondary control is enabled at $ts1$, and a 200W active load is increased and restored at $ts2$ and $ts3$, respectively. It is claimed that the communication technologies used in microgrids generally have a latency of less than 100ms [83], so in this section, we test the power-sharing performance under 70ms and 100ms as shown in Fig.3.21(a) and (b), respectively. It can be seen that when suffering a 70ms delay, the active power exhibits good performance. When the inverter system is challenged by a 100ms delay, a slight oscillation is imposed but later attenuated. Therefore, this test shows that the proposed DMPC can maintain power sharing even under communication delay. Additionally, the influence of delay is mainly about two principal factors [84]: (1) the maximum degree of the graph, which signifies the highest number of connections among the participating converters. Systems characterized by greater interconnectivity are more susceptible to delay. (2) the consensus gain, wherein distributed systems with faster convergence speed requirements are affected

more by delays. Therefore, the number of connections or the convergence gain can be adjusted accordingly when faced with higher communication delays.

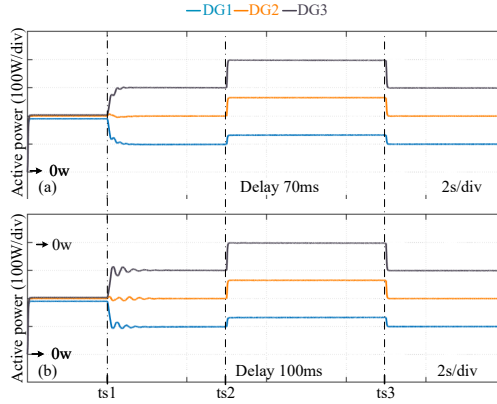


Figure 3.21: Active power sharing performance comparison with the proposed method under communication delay:(a) DMPC with $70ms$ delay. (b) DMPC with $100ms$ delay.

Moving on to Fig.3.22(a), (b), and (c), they describe the plug-and-play capacity of the methods in [65, 67], and the proposed DMPC, respectively, in scenarios where the communication network is disabled at $ts4$. These three approaches exhibit efficacy in power-sharing control when communication information is readily available. As these three figures depict the expected active power performance when the secondary control is enabled at $ts1$.

However, when the communication infrastructure is deactivated, the DMPC method expounded in [65], as shown in Fig.3.22(a), manifests ineffectiveness immediately, as well as the plug-and-play capacity. For the DMPC delineated in [67], as shown in Fig.3.22(b), the power-sharing during non-periodic communication can be guaranteed. However, the operational units' power-sharing ratio is not 1:2 during the stage between $ts5$ and $ts6$ where the $DG3$ is plugged out and re-plugged in, respectively. This observation indicates the dependency of existing methods on continuous communication and regular real-time calculations. Importantly, the proposed method derives advantages from the conservation of communication and computational resources, as evidenced in Fig.3.22(c). In the no-communication scenario, the microgrid can keep the plug-and-play capacity.

In addition, Table 3.4 compares the triggered number of the existing research and the proposed method. It should be noted that the complexity of computation and communication burden is generally considered the restriction of distributed model predictive control. The DMPC-based method for power sharing has been studied in [65, 67]. However, it necessitates periodic communication among the units. To reduce the communication pressure, event trigger control can be adopted in microgrid distributed control [61, 63, 70]. The triggered numbers of these methods for active and harmonic power sharing can be reduced to some extent. It is declared that combining the DMPC and event trigger method decreases the trigger numbers with the aperiodic communication. Moreover, with the proposed DMPC method, as shown in the experimental results, only a single trigger number

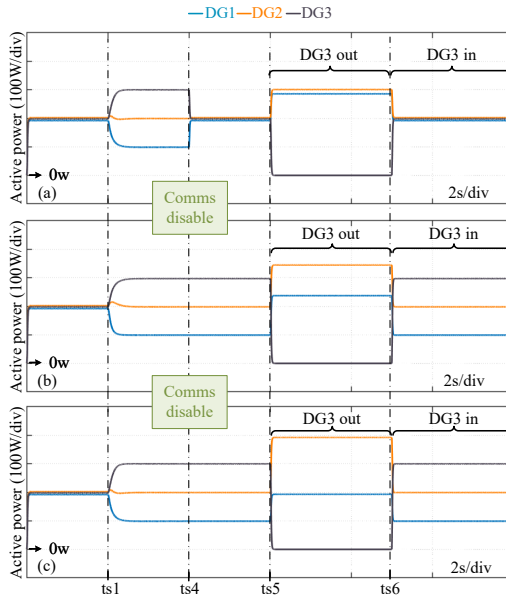


Figure 3.22: Active power performance of PnP test: (a) PnP test of DMPC in [65]. (b) PnP test of DMPC in [67]. (c) PnP test of the proposed DMPC.

is needed, significantly reducing the communication burden. As the proposed scheme does not need the predictive algorithm for control at this stage, the computation burden is also relaxed.

Table 3.4: Communication burden comparison

Ref	[33, 65, 67]	[58]	[61, 63, 70]	Proposed
Trigger way	Continually	Periodically	Event trigger	Single trigger
Comms burden	High	Medium	Medium	Low

EXPERIMENT RESULTS

The experiments, focusing on three critical scenarios, were conducted to evaluate the precision and effectiveness of the proposed DMPC method introduced in this section. The plant and control parameters of the microgrid are detailed in Table 3.3. Notably, the feeder impedance was varied from 2.2mH to 0.5Ω to validate the DMPC-based power control under a resistive feeder.

Case A): Performance in Active Power and Harmonic Power Sharing under Load Variations: We compare the power-sharing performance before and after the proposed method is activated and investigate its robustness by showing DMPC’s effective power distribution management when the load is changed.

Case B): Resilience Investigation to Communication Failures: We evaluate DMPC's ability to maintain resilient performance and grid stability despite communication disruptions, highlighting its reliability and fault-clear capacity.

Case C): Plug-and-Play Operation in AC Microgrids without Communication Dependencies: We assess the plug-and-play capacity of the DMPC, even if the communication is disabled, emphasizing its potential to function autonomously within AC Microgrids and relax the burden for communication and complex computation.

3

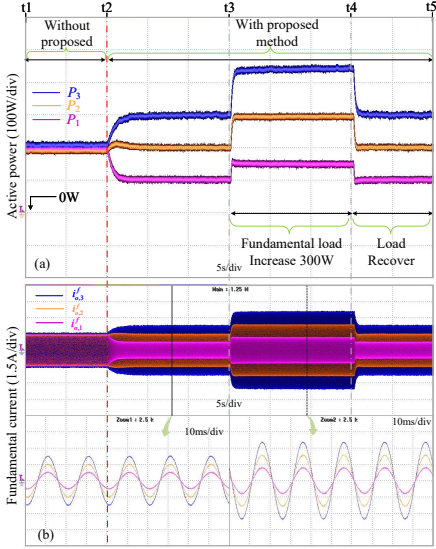


Figure 3.23: Performance of the designed controller: (a) Active power. (b) Fundamental current.

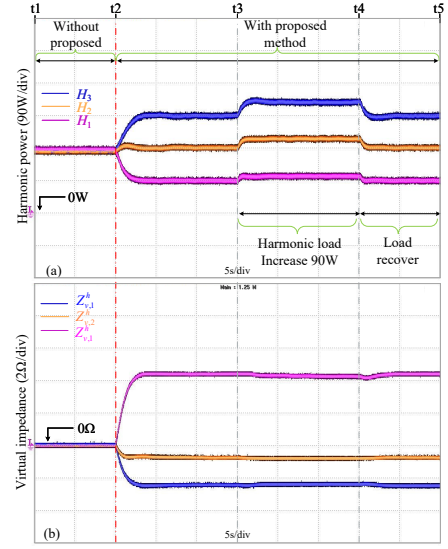


Figure 3.24: Performance of the proposed controller: (a) Harmonic power. (b) 3^{rd} harmonic virtual impedance.

PERFORMANCE IN ACTIVE POWER AND HARMONIC POWER SHARING UNDER LOAD VARIATIONS

The responses of the output active power of the involved inverters (P_1, P_2, P_3) and output fundamental current ($i_{0,1}^f, i_{0,2}^f, i_{0,3}^f$) are displayed in Fig.3.23(a),(b) respectively. As can be seen from Fig.3.23(a), at the start of the experiment procedure ($t1-t2$), the output active power of all DGs will exhibit almost the same because of the feeder impedance and the output impedance's joint influence. However, the expected sharing ratio of DG1:DG2:DG3 is 1:2:3, according to the maximum output capacity of the inverter of the experiment setup. At $t2$, the proposed DMPC-virtual impedance-based secondary control is activated, contributing to the active power-sharing ratio and the fundamental current sharing ratio in Fig.3.23(b) shift from 1:1:1 to 1:2:3, which proved the effectiveness of the proposed method. The load changes at $t3$, where the output active power increases by 300W. In the $t3-t4$ stage, the active power can still maintain 1:2:3; when it recovers to 600W at $t4$, the output active power of the inverters is changed to 100W, 200W, and 300W, respectively.

Fig.3.24(a),(b) demonstrate the harmonic power-sharing performance (H_1, H_2, H_3) and virtual impedance ($z_{v,1}^h, z_{v,2}^h, z_{v,3}^h$) in the same period, which shows the proposed method

also validates for harmonic power sharing. From $t1-t2$, each unit contributes the same harmonic power (180W).

At $t2$, the proposed DMPC is enabled, and the harmonic power-sharing ratio is shifted to 1:2:3 from 1:1:1. In this period, the virtual impedance is tuned to make the sum of virtual impedance, inverter output impedance, and feeder impedance proportionally set, which is inverse to the harmonic power-sharing ratio. The harmonic power is increased by 90W in the $t3-t4$ stage and restored to 540W at $t4$. In the load change case, after the proposed method is activated, the harmonic power-sharing ratio maintains 1:2:3, and the virtual impedance remains unchanged. This means that the proposed method will not affect the regular load change operation of the microgrid.

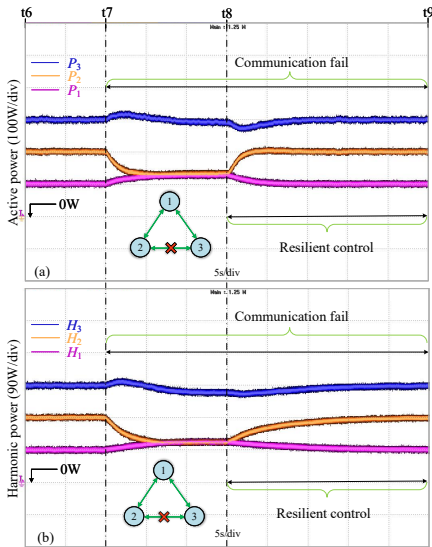


Figure 3.25: The resilience against communication failure: (a) Active power. (b) Harmonic power.

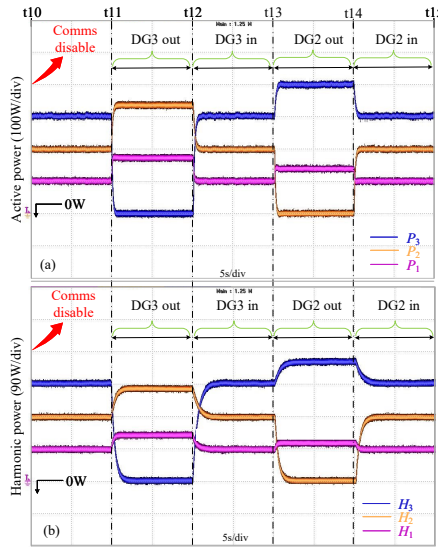


Figure 3.26: Communication independence verification: (a) Active power. (b) Harmonic power.

RESILIENCE INVESTIGATION TO COMMUNICATION FAILURES

Further, the control performance of the proposed DMPC approach in communication failure is evaluated on the experimental platform. Fig.3.25(a) and (b) show the performance of active power and harmonic power, respectively.

In the active power sharing scenario, the communication link 3-2 suffers a failure denoted in Fig.3.25(a), and the link 3-2 occurs a communication failure at $t7$ for harmonic power sharing as shown in Fig.3.25(b).

To be specific, in $t6-t7$, the propagated information is in regular communication, and the power-sharing ratio is 1:2:3. In $t7-t8$, the transmitted data is forced to be zero due to the communication failure, which may distort the reference of the DMPC since the local DMPC controller computes the reference based on the received information. As it can be seen, in the $t6-t7$ stage, the active power and harmonic power sharing are no longer 1:2:3. Fortunately, the DMPC considers the physical constraints of the system, which means the

virtual impedance can only be adjusted in an allowable range. This constraint can promise that the system will not oscillate and be unstable. At $t8$, the proposed resilient framework is activated, and the adjacent matrix A is replaced by A^e , the improved adjacency matrix, thus disregarding the corrupted communication link. In other words, with the modification adjacent term $a_{i,j}^e(k)$, as shown in (3.62), the corrupted propagated information will not be taken into account for power reference compute for the DMPC controller; Thus, it will not affect the output power. With the resilience method, the active power and harmonic power-sharing ratio return to 1:2:3. The results demonstrate the resilience of the proposed method against communication failure.

3

PLUG-AND-PLAY OPERATION IN AC MICROGRIDS WITHOUT COMMUNICATION DEPENDENCIES:

To investigate the communication independence of the proposed DMPC approach in terms of plug-and-play capability, we conduct the experimental scenarios as follows on the test platform established, where Fig.3.26(a) and (b) show the active power and harmonic power performance, respectively.

First, the whole communication network is deactivated at $t10$. It can be seen that both active power and harmonic power sharing performance can remain 1:2:3. Subsequently, $DG3$ is assumed to be inaccessible and plugged out at $t11$ and then be back and connected to the MG at $t=t12$. In contrast, $DG2$ is plugged out at $t12$ and reconnected at $t14$.

During $t11-t12$, as $DG3$ is de-plugged, its physical link connected to the inverter-connected system is lost. The tie lines from $DG3$ to $DG1$ and from $DG3$ to $DG2$ are regarded as open circuits. Meanwhile, the coordinated distributed predictive control scheme is inactive for $DG3$ during $t11-t12$. The proposed DMPC also does not need to be effective for the active power and harmonic power regulation of the remaining DGs in the microgrid since the virtual impedance has been appropriately set. In this period, the output active power and harmonic power of $DG3$ is 0W. Thanks to the pre-adjusted virtual impedance, the operational units $DG1$ and $DG2$ maintain a power-sharing ratio of 1:2, following the expected ratio. Similarly, during $t13-t14$, the $DG2$ is plugged out, thus outputting 0W active power and harmonic power. The operational $DG1$ and $DG3$ exhibit a power-sharing ratio of 1:3. During $t12-t13$ and $t14-t15$, the plugged-out unit is replugged in the microgrid, and the power-sharing proportion is recovered to 1:2:3 among the three inverters. The DMPC-based secondary control benefits plug-and-play capacity even if there is no communication since the virtual impedance has been pre-adjusted and fixed, thus independent of the communication network.

3.6 CONCLUSION

Communication-based virtual impedance, including consensus algorithm-based and distributed model predictive control methods, enables the effective sharing of active, reactive, and harmonic power in microgrids with both inductive and resistive feeders while ensuring PCC voltage quality through precise impedance design. However, dependence on communication networks introduces vulnerabilities to cyber-attacks and communication failures. To mitigate these risks, the proposed signal reconstruction and corrupted signal blocking methods are effective in countering cyber-attacks. The effect of the signal reconstruction approach further enhances resilience by allowing the communication network to

be deactivated once virtual impedance is established, reducing exposure to communication disruptions. This strategy requires only brief communication during the integration of new DG units, significantly lowering communication demands. Lyapunov stability analysis demonstrates that the system's power-sharing reliably converges even under communication failures, and experimental results validate the robustness and effectiveness of these approaches in improving microgrid performance and reliability.

4

MULTI-VSGs GRID: ACTIVE POWER OSCILLATION IN CIRCUIT PERSPECTIVE

4

Active power oscillation (APO) issues may arise during the deployment of multiple parallel converters with Virtual Synchronous Generator (VSG) control in both stand-alone (SA) mode and grid-connected (GC) mode. This chapter proposes two control methods to address APO issues in SA and GC modes, respectively. To that end, the equivalent circuit models of a converter with VSG control in both modes are proposed, which intuitively reveals the root cause of APOs. Accordingly, a graph-theory-based virtual impedance is introduced to harmonize parameters among involved VSGs, effectively eliminating APOs in SA mode. As for GC mode, the APOs are attenuated through the proposed adaptive inertial coefficient, which is dynamically tuned via a feedforward loop. Simulation and experimental results verify the improvements of the proposed control.

This chapter is based on:

-J. Xiao, L. Wang, P. Bauer and Z. Qin, "Active Power Oscillation in Paralleled VSGs," IEEE Transactions on Power Electronics, under review.

4.1 INTRODUCTION

The penetration of renewable energy resources has shown a significant increase in recent decades to address the escalating severity of the energy crisis [85–87]. In this context, distributed generation technology has garnered widespread attention. Nonetheless, the predominantly used droop control may degrade the system's frequency stability [88–92]. The transition from droop control to VSG control can enhance critical frequency indicators such as the rate of change of frequency (RoCoF), thereby benefiting grid stability [93, 94]. However, introducing oscillatory dynamics complicates the system, potentially leading to significant frequency and active power oscillations. These oscillations occur both in grid-connected (GC) mode and when multiple VSGs operate in stand-alone (SA) mode [95]. The large instantaneous currents associated with these oscillations can trigger overcurrent protection mechanisms, exacerbating system stability issues [96].

4

Various variants of VSG control have been proposed to suppress dynamic oscillations in converters' active power and output frequency. These methods can be broadly classified into two main categories: model-free and model-based approaches. The model-free methods include adaptive parameter tuning and feedback loop compensation. In contrast, model-based techniques typically involve optimal inertia and damping design, feedforward loop compensation, and virtual impedance.

For instance, the model-free approach, such as studies in [97, 98], detects deviations in VSG frequency from its nominal value and assigns different inertia at different situations to mitigate oscillations. Specifically, larger inertia is applied to counteract these deviations when the DG frequency deviates from the common frequency. In contrast, smaller inertia accelerates system convergence when DG frequencies align with the common frequency. This control strategy ensures that all DG frequencies promptly synchronize with the common frequency. Furthermore, [99] proposes a real-time self-adaptive inertia and damping combination control method to enhance frequency stability through an interleaving control technique. However, these adaptive tuning methods introduce a nonlinear element into the overall DG operation, potentially altering the carefully designed inertia settings.

An additional intuitive approach to mitigate oscillations involves incorporating an extra feedback loop into the original VSG framework. For instance, in [100], deviations between a DG's frequency and the system's common frequency are detected, leading to adjustments in the DG's inertia. Studies such as [37, 101] integrate variations in a DG's power, frequency, or phase during transients to establish feedback loops. These feedback loops input the oscillation element into the VSG decision process, achieving disturbance compensation. Moreover, graph theory-based secondary frequency control is applied to achieve frequency consensus of VSGs utilizing low-bandwidth communication. In studies such as [102, 103], the DG's frequency and active power are compared to those of neighboring DGs, with disparities typically used to compensate directly at the output frequency reference. In [104, 105], frequency disparities with neighboring DGs are employed to develop a mutual damping term for mitigating power oscillations.

Despite the technical effectiveness of these model-free methods, they become effective only after oscillations occur and have been detected. Consequently, VSGs inevitably experience power and frequency oscillations, particularly those with slow power loops. Additionally, the feedback loop's effectiveness is sensitive to the accuracy of oscillation detection.

In addition to model-free methods, model-based approaches are employed to mitigate power oscillations. For instance, [106] adjusts the damping and inertia coefficients simultaneously to determine and maintain the optimal damping ratio, thereby suppressing power and frequency oscillations throughout the operation. Similarly, [107] proposes an additional damping correction loop that adjusts the system damping ratio without affecting the steady-state frequency droop characteristic. However, this approach changes the preset inertial response of the VSG. In [108], the active power reference is feedforward to the VSG frequency to enhance damping. However, this feedforward controller is designed explicitly for changes in power reference, so it does not mitigate power allocation in SA mode. Notably, [109] utilizes a phase feedforward path to replace the traditional frequency compensation path; this can enhance the damping in both SA and GC modes. Furthermore, [110] analyzes the power oscillation mechanism and utilizes virtual impedance to suppress power oscillations caused by line mismatches. In [111], parameter design principles are defined to eliminate all transient circulating power theoretically. Nevertheless, an ideal parameter necessitates full knowledge of the system. Although these model-based methods provide effective damping for oscillation mitigation, they typically require foreknowledge of the system, such as feeder impedance. This cannot be assured in practical scenarios.

Table 4.1: Comparison of the methods for power oscillation mitigation.

Type	Method	Reference	Tuning	Description	Inertia	Oscillation relief
Mode free	Self-parameter	[97–99]	-inertia -damping	-introduces nonlinear -slowly response	degrades	
	Feedback	[37, 100–104]	-power reference -frequency	-continuous comms -slowly response	maintain	
	Proposed	/	-impedance -inertia	-feeder info free -fast response	maintain	
Mode based	Optimal Design	[106, 107]	-inertia -damping	-feeder info needed	degrades	
	Feed-forward	[108]	-frequency	-feeder info needed	degrades	
	Virtual impedance	[110, 111]	-impedance	-feeder info needed -voltage drop	maintain	

Apart from the challenges in the control method, another gap in the literature is seen, which is that the existing models explaining the APO issues induced by the VSG transfer function are overly complicated and absent physical meaning. Such hinders the discovery of the root cause of the APO issue. This article suggests a more intuitive modeling perspective that visualizes closed-loop VSG control as an impedance circuit with resistance, inductance, and capacitance. This approach highlights the characteristics of VSGs from a circuit perspective and illustrates their interactions and coupling effects. Additionally, it offers a circuit-based explanation and suppression method for the APO issue

in multiple VSG systems. Specifically, in GC mode, the oscillations can be understood as a second-order oscillation problem analogous to the existence of LC resonance from a circuit perspective. The solution involves appropriate adjustments to the different impedance elements to dampen the resonance peak. Conversely, in SA mode, oscillations arise due to parameter mismatches rather than the introduction of inertia and insufficient damping. From the impedance circuit perspective, this phenomenon is attributed to differences in the resonance of the VSG equivalent impedance circuit, which needs to be tuned. Based on the above analysis, this chapter proposes a distributed virtual impedance method to harmonize parameters in SA mode and eliminate oscillations. Notably, the well-designed inertia and damping coefficients can be maintained with the proposed method. In GC mode, a feed-forward loop is suggested to trigger an adaptive virtual inertia element, which can benefit quick oscillation mitigation without degrading the RoCoF when switching to SA mode. Tab.4.1 compares the proposed method and the latest research for VSG oscillation mitigation, where the larger the green ratio represents the better the oscillation suppression effect.

This chapter's main contributions are summarized as follows:

- 1) The equivalent circuit model of a converter with VSG control is proposed, which provides clear physical interpretations. In this model, inertia, damping, and feeder impedance are analogized to capacitance, resistance, and inductance, respectively. Active power reference changes and load switches are considered excitation sources that inject power into the VSG. The frequency and power oscillations are viewed as LC resonance phenomena.
- 2) A distributed virtual impedance method is proposed to attenuate oscillations in the SA mode. This method benefits from a faster response to load variations and less communication dependence.
- 3) Conventional VSG control is modified by adding a feed-forward loop to enable the adaptive inertia coefficient that helps to mitigate APOs in GC mode. One benefit is that when switching to SA mode, the feed-forward loop does not degrade the RoCoF.

The chapter is structured as follows: Section 4.2 details the active power oscillation induced by VSG. Section 4.3 proposes revisiting the VSG control from an impedance circuit perspective. Section 4.4 suggests a method to mitigate the oscillation based on the circuit. Section 4.5 verifies the effectiveness of the proposed methods by Simulink and experiment. Finally, Section 4.6 concludes the chapter.

4.2 VSG OSCILLATION ANALYSIS

This section reviews the two most discussed primary controls among n -distributed generators-tied microgrids, as shown in Fig.4.1.

This chapter assumes, first, that the dynamic response of the inner control loop is generally slower than that of the outer power loop. Second, it presumes that the line impedance is predominantly inductive. This chapter's assumption is typically valid in medium and high-voltage power systems due to transformers' leakage inductance and long cable distance.

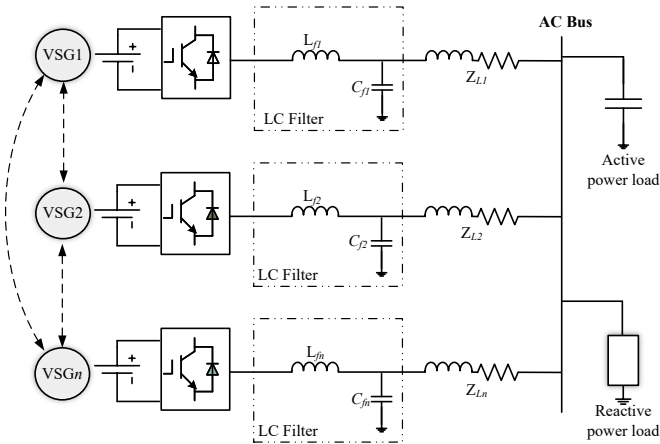


Figure 4.1: The microgrid configure with n VSG based converter.

4.2.1 REVIEW ON TRADITIONAL DROOP AND VSG CONTROL

The power control loops of droop and VSG control are shown in Fig.4.2. The difference between VSG and droop control mainly focuses on the active power control loops, and the reactive power loops are ignored here.

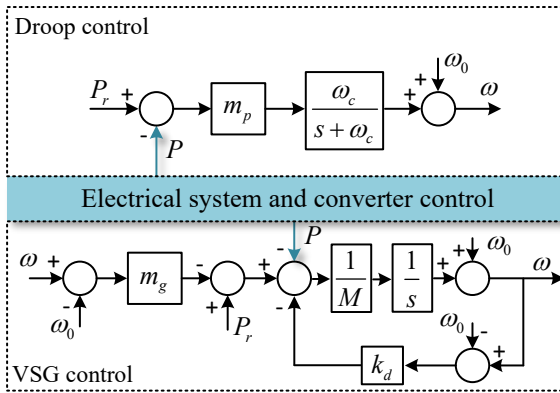


Figure 4.2: Active power loop implementation: droop control and VSG control.

The active power control equation for traditional droop control is shown in (4.1).

$$\omega = \omega_0 - m_p \frac{\omega_c}{s + \omega_c} (P - P_r) \tag{4.1}$$

where ω represents the generated angular frequency reference of the inverter output voltage, ω_0 is the nominal value of angular frequency, m_p is the droop coefficient of active power loop, P represents the inverter output active power, P_r is the nominal value of active power, and ω_c is the cutoff angular frequency of the low-pass filter.

The active power control equation for VSG is shown in (4.2).

$$P_r - m_g(\omega - \omega_0) - P - D(\omega - \omega_0) = M \frac{d(\omega - \omega_0)}{dt} \quad (4.2)$$

where m_g is the proportional coefficient of the governor, k_d is the damping factor, and M is the moment of inertia.

Accordingly, the small-signal model of droop control and VSG can be simplified, as shown in Fig.4.3 and Fig.4.4, respectively.

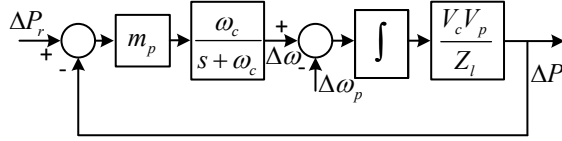


Figure 4.3: Small-signal model of droop control.

In Fig.4.3, ω_p is the angular frequency of the PCC point. V_c represents the unit output voltage, V_p is the PCC voltage, and Z_l denotes the feeder impedance.

Considering the RoCoF rule, the dynamic performance of angular frequency when the load changes is the main focus in the SA mode. For droop control, the small-signal transfer function of angular frequency change $\Delta\omega$ over loading transition ΔP is shown in (4.3).

$$G_{d,sa} = \frac{\Delta\omega}{\Delta P} = -m_p \frac{\omega_c}{s + \omega_c} = -m_p \frac{1}{s/\omega_c + 1} \quad (4.3)$$

In the GC mode, the converters are expected to track the power commands precisely. Therefore, the small-signal transfer function from active power reference ΔP_r to the actual output active power ΔP is considered as shown in (4.4), and $\Delta\omega_p$ is the PCC frequency disturbance. Here, $K = V_c V_p / Z_l$.

$$\Delta P = \frac{\omega_c m_p K}{s^2 + \omega_c s + \omega_c m_p K} \Delta P_r - \frac{(s + \omega_c) K}{s^2 + \omega_c s + \omega_c m_p K} \Delta\omega_p \quad (4.4)$$

For traditional VSG control in Fig.4.2, by simplifying the inertial and damping term in Fig.4.2 with $J = M$ and $D = k_d + m_g$. The small signal model of VSG in Fig.4.2 can be simplified as shown in Fig.4.4.

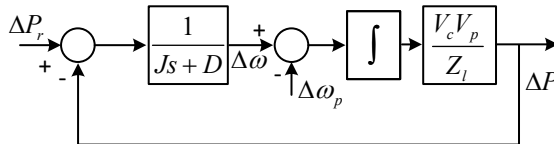


Figure 4.4: Small-signal model of VSG control.

The transfer functions of VSG control in stand-alone mode and grid-connected mode are shown in (4.5) and (4.6), respectively.

$$G_{v,sa} = \frac{\Delta\omega}{\Delta P} = -\frac{1}{Js+D} = -\frac{1}{D} \frac{1}{Js/D+1} \quad (4.5)$$

$$\Delta P = \frac{K}{Js^2+Ds+K} \Delta P_r - \frac{K(Js+D)}{Js^2+Ds+K} \Delta\omega_p \quad (4.6)$$

Combining (4.3)-(4.6), with $m_p = 1/D$, $\omega_c = D/J$, the droop control can be equivalent to VSG control. Subsequently, this chapter adopts VSG for the power converter control verification.

4.2.2 ACTIVE POWER OSCILLATION WITH VSG CONTROL

As VSG simulates the synchronous generator's inertia and damping characteristics, the synchronous generator's oscillation characteristics are inevitably introduced. This subsection investigates the mechanism of active power oscillation in SA and GC modes.

OSCILLATION IN SA MODE

The active power across the feeder can be obtained as shown in (4.7).

$$P_i = \frac{V_{c,i} V_p}{Z_i} \sin\delta_i = K_i \frac{\Delta\omega_i - \Delta\omega_p}{s} \quad (4.7)$$

where the subscript i of the variable represents the i -th converter, δ_i is the power angle difference of i -th converter and PCC power angle. Within a multi-unit system, the coupling of different units is caused by PCC frequency variation.

Based on the small signal diagram of VSG, the transfer function from the bus voltage fluctuates to i -th VSG output variation characteristics can be expressed as (4.8):

$$\begin{cases} \Delta P_i = \frac{-K_i(J_i s + D_i)}{J_i s^2 + D_i s + K_i} \Delta\omega_p \\ \Delta\omega_i = \frac{K_i}{J_i s^2 + D_i s + K_i} \Delta\omega_p \end{cases} \quad (4.8)$$

The output power of the involved DGs is equal to the load power P_L , which can be represented as in (4.9).

$$\sum_{i=1}^n \Delta P_i = \Delta P_L \quad (4.9)$$

By combining equations (4.8)-(4.9), the transfer function that describes the interrelationship between load changes and PCC frequency variations for VSGs operating in SA mode can be derived as shown in (4.10). This derivation facilitates calculating the PCC frequency responses of VSGs under varying load conditions.

$$\Delta\omega_p = -\frac{1}{\sum_{i=1}^n G_i(s)(J_i s + D)} \Delta P_L \quad (4.10)$$

where $G_i = -K_i/(J_i s^2 + D_i s + K_i)$. In the case of a single VSG-based converter, the system can smoothly transition to steady-state operation during load fluctuations. However, when multiple VSGs are connected in parallel, their dynamic responses can differ significantly due to variations in control parameters. Sudden load changes, which cause fluctuations in the system PCC frequency, exacerbate these dynamic differences in the frequency responses of each distributed generator. Consequently, this discrepancy leads to varying dynamic responses in active power among the DGs.

$$\begin{cases} \Delta\omega_i = -\frac{G_i(s)}{\sum_{k=1}^n G_k(s)(J_k s + D)} \Delta P_L \\ \Delta P_i = -\frac{G_i(s)(J_i s + D)}{\sum_{k=1}^n G_k(s)(J_k s + D)} \Delta P_L \end{cases} \quad (4.11)$$

Accordingly, the transfer function describes the dynamics and steady state of the converters when the load switch is shown as in (4.11).

Based on the analysis above, increasing the damping coefficient D or decreasing the inertia coefficient J within a certain range can suppress active power and frequency oscillations in multi-VSG systems during load changes. However, since D is coupled with the droop coefficient, representing the steady-state frequency deviation, modifying D will inevitably change the frequency deviation nadir. Additionally, decreasing J is undesirable for VSGs as it may violate the RoCoF rules. Consequently, a trade-off between the dynamic and steady-state performance of the VSG is unavoidable. Moreover, existing virtual impedance techniques may be ineffective, as exact parameter matching of parallel VSGs may not be fully achievable. While inserting substantial virtual impedance into the control loop can mitigate oscillations, it also leads to considerable and unexpected voltage drops.

OSCILLATION IN GC MODE

In the grid-connected mode, the active power is determined by the power reference ΔP_{ri} and PCC frequency $\Delta\omega_p$, which can be explained as in (4.12).

$$\Delta P_i = \frac{K_i}{J_i s^2 + D_i s + K_i} \Delta P_{ri} - \frac{K_i (J_i s + D_i)}{J_i s^2 + D_i s + K_i} \Delta\omega_p \quad (4.12)$$

Based on (4.7), the power support from the utility grid is (4.13).

$$\Delta P_g = -\frac{K_g}{s} \Delta\omega_p \quad (4.13)$$

Assuming the load remains unchanged, the sum of power flow change is zero.

$$\sum_{i=1}^n \Delta P_i + \Delta P_g = 0 \quad (4.14)$$

Based on (4.12)-(4.14), the transfer function from power reference to PCC frequency is as (4.15).

$$\Delta\omega_p = -\frac{\sum_{i=1}^n G_i(s)\Delta P_{ri}}{K_g/s + \sum_{i=1}^n G_i(s)(J_i s + D)} \quad (4.15)$$

The frequency and active power dynamics when power commands change is simplified as in (4.16)

$$\begin{cases} \Delta\omega_i = sG_i(s)\Delta P_{ri} + G_i(s)\Delta\omega_p \\ \Delta P_i = G_i(s)\Delta P_{ri} - G_i(s)(J_i s + D)\Delta\omega_p \end{cases} \quad (4.16)$$

Based on equations (4.15) and (4.16), the impact of the power reference on PCC frequency, and subsequently its interaction with the DG's power, is relatively minimal. Consequently, the transfer function from power reference (ΔP_r) to output power (ΔP_i) can be modeled as a second-order system, which is inherently prone to oscillations.

4

4.3 EQUIVALENT IMPEDANCE CIRCUIT OF VSG

An equivalent circuit model is developed in this section to understand the root cause of APO issues intuitively, which, in the end, leads to the proposed mitigation measures for APO issues in both SA mode and GC mode.

4.3.1 SINGLE-VSG EQUIVALENT

From the VSG small signal in Fig.4.4, the following equation can be rephrased as in (4.17) and (4.18):

$$\frac{1}{K_i} \frac{d\Delta P_i}{dt} = \Delta\omega_i - \Delta\omega_p \quad (4.17)$$

$$\Delta P_{ri} = \Delta P_i + J_i \frac{d\Delta\omega_i}{dt} + D_i \Delta\omega_i \quad (4.18)$$

Tab.4.2 shows the analogy relationships between the control and circuit variables.

Table 4.2: Correspondence between VSG and circuit variables.

Circuit	U_i	U_p	I_i	I_{ri}	I_L	R_i	C_i	L_i	L_g
VSG	$\Delta\omega_i$	$\Delta\omega_p$	ΔP_i	ΔP_{ri}	ΔP_L	$1/D_i$	J_i	$1/K_i$	$1/K_g$

In Tab.4.2, subscript i represents the DG's parameter, while subscript g represents those of the utility grid, and subscript p represents the PCC's parameter. ω_i is the equivalent to the voltage U_i , representing the frequency change. ΔP_i is the equivalent to the current I_i , representing the active power change. J_i is equivalent to a capacitance C_i , representing the inertia; $1/D_i$ is the resistance R_i , representing the damping factor; $1/K_i$ is equivalent to an inductance L_i , representing the term associate with feeder impedance. According to

Tab.4.2, (4.17) and (4.18), which denote the closed-loop small-signal control model of VSG, can be likened to the dynamic equivalent circuit model, as shown in (4.19) and (4.20).

$$L_i \frac{dI_i}{dt} = U_i - U_p \quad (4.19)$$

$$I_{ri} = I_i + C_i \frac{dU_i}{dt} + \frac{U_i}{R_i} \quad (4.20)$$

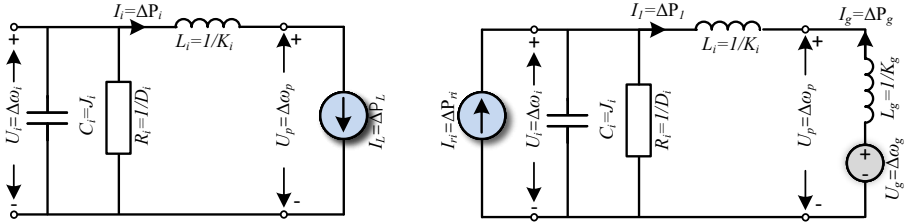
With the (4.9), the current follows the rule in (4.21).

$$\sum_{i=1}^n I_i = I_L \quad (4.21)$$

4

where I_r and I_L can also be viewed as two excitation sources in the circuit.

Combining (4.8)-(4.21), the VSG models in SA and GC modes can be analogized to the equivalent circuit in Fig.4.5. Accordingly, the power–frequency relationship in the VSG is analogous to the current–voltage relationship in a second-order RLC circuit. In this analogy, the inertia coefficient J_i suppresses frequency changes similarly to how the capacitor stabilizes circuit voltage. The damping coefficient D_i governs the angular frequency changes in output power, analogous to how resistance determines the voltage change relative to the current in the circuit.



(a) Equivalent in SA mode.

(b) Equivalent in GC mode.

Figure 4.5: Single VSG equivalent circuit.

In the SA mode, the current source I_L is enabled when the load switches. Consequently, the current I_i increases to match I_L . The capacitance C_i reduces the voltage change rate U_i , analogizing that VSG provides inertia and maintains the RoCoF. The steady-state value of U_i is determined by the resistance R_i , which acts as the droop coefficient that dictates the frequency deviation. As the comparison in Section II, a key distinction between traditional droop control and VSG control is the inclusion of capacitance in the latter.

In the GC mode, the current I_i tracks the current reference I_{ri} , indicating that the VSG's output power follows the active power reference. Assuming the utility power grid is ideal, we ignore grid frequency variation, denoted as $U_g = 0$. When I_{ri} increases, the current I_i may oscillate initially before aligning with the reference. This oscillation results from RLC resonance, which is characteristic of a standard second-order system. The voltage across the capacitor U_i will dynamically adjust and eventually converge to zero, ensuring that the

PCC frequency aligns with the grid frequency. In contrast, traditional droop control does not experience this oscillation because, without C_i , no RLC resonance, the output current I_i can smoothly transition to the reference value.

4.3.2 MULTI-VSG EQUIVALENT

In this section, the transient behavior of a VSG in a multi-converter system operating in SA mode is intuitively analyzed through the resonance in its equivalent impedance circuits. The current expression for each branch can be obtained by establishing nodal voltage equations for circuit analysis. Subsequently, the resonance in the equivalent circuit can be quantitatively analyzed, providing insights for deriving circuit parameter configuration rules. Similarly, VSG parameters can be configured to eliminate power oscillations during the VSG's transient. Combined with system frequency stability requirements, the selection of VSG parameters gains physical significance.

SA MODE

Based on Fig.4.5(a), the multi-VSG equivalent circuit can be derived. In this section, a two-VSG system is considered for analysis, and it can be extended to a n VSG-connected system. They can be equivalent to the impedance circuit perspective as shown in Fig.4.6.

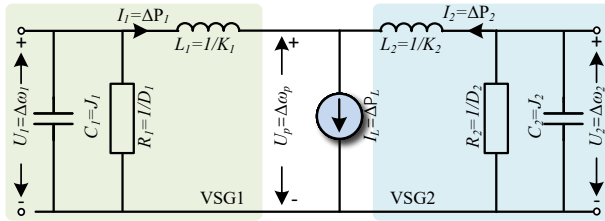


Figure 4.6: Multi-VSG's equivalent circuit perspective in SA mode.

Herein, I_L represents a current source that models a step change in load, contributing to variations in voltage and current. As expressed in (4.21), the relationship $I_1 + I_2 = I_L$ holds throughout the entire operation. This indicates that the circuit operates in parallel, and thus the current sharing ratio $I_1:I_2$ is determined by the equivalent impedance of each branch.

Accordingly, the equivalent impedance of the circuit Z_{ei} is as (4.22) in the circuit perspective.

$$Z_{ei} = \frac{U_p}{I_i} = \frac{1}{C_i s + R_i} + sL_i \quad (4.22)$$

With a given current source, the current I_i is demonstrated by the impedance, where the resonance may occur. The resonance frequency $\omega_{re,i}$ and amplitude of the equivalent circuit impedance at this frequency $Z_{ere,i}$ is shown as in (4.23).

$$\omega_{re,i} = \sqrt{\frac{1}{L_i C_i} - \frac{1}{R_i^2 C_i^2}}, Z_{ere,i} = \frac{L_i}{R_i C_i} \quad (4.23)$$

The analysis of the circuit current I_i sharing reveals two primary components: 1) steady-state active power sharing and 2) dynamic active power sharing. The steady-state active power sharing is characterized by the proportional setting of the resistors R_i , consistent with the damping coefficients D_i . Moreover, accurate dynamic current sharing means no current oscillation is within the system. This requires that the circuit model's impedance Z_{ei} remains proportional throughout the dynamic process. It should be noted that the resonance inconsistency leads to disproportional current sharing, implying that the resonance frequency of each inverter must be the same. Moreover, the impedance at the resonance frequency must remain proportional to the maximum capacity to ensure proportional current during the dynamics.

Accordingly, the circuit elements are tuned proportionally to avoid oscillation. Converting to the VSG control variable in Tab.4.2, the VSG parameters are set as in (4.24). Here, $P_{i,m}$ denotes the maximum output active power capacity of i -th converter.

$$\frac{P_{i,m}}{P_{j,m}} = \frac{J_i}{J_j} = \frac{D_i}{D_j} = \frac{K_i}{K_j} = \frac{Z_j}{Z_i} \quad (4.24)$$

GC MODE

Based on Fig.4.5(b), the two-VSG system in GC mode can be equivalent to the impedance circuit perspective as shown in Fig.4.7.

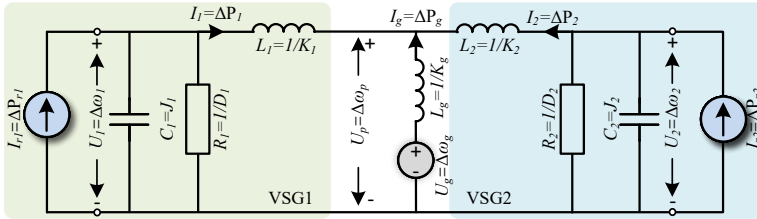


Figure 4.7: Multi-VSG's equivalent circuit perspective in GC mode.

In this mode, the sum of the power support is a constant, the same as the load consumption, denoted as (4.25). The reference of DG1 and DG2, $\Delta I_{r1}(\Delta P_{r1})$ and $I_{r2}(\Delta P_{r2})$ are changed as an example for verification.

$$\sum_{i=1}^n I_i + I_g = 0 \quad (4.25)$$

Based on Fig.4.5(b), the power flow across each DG can be intuitively shown. When the current reference step, its influence on current and voltage variation can be shown in (4.26). when the L_g is small, the change of $I_{r,1}$ is less likely to influence on I_2 .

$$\begin{cases} U_p = I_g \cdot sL_g \\ I_i = \frac{1/(L_i + L_g)}{C_i s^2 + s/R_i + 1/(L_i + L_g)} \cdot I_{ri} \end{cases} \quad (4.26)$$

This indicates that the oscillation caused by reference change is mainly determined by the DGs' self-resonance but not the interconnection with other DGs. The I_{ri} of i th DG changes only affect its own output current and voltage. From the perspective of VSG control, when the feeder impedance of the utility power grid is small, the interactions between different VSGs are decoupled, making the PCC frequency dominated by the utility grid frequency. Therefore, the reference change of VSG i only impacts itself.

Therefore, it can be derived that the oscillation of the current across the inductor, which represents the power oscillation in VSG control, is caused by the resonance between the capacitor and the inductance shown in Fig.4.7. When the resonance occurs, the RLC parallel is equivalent to the resistor, which means $1/[C_i s + 1/R_i + 1/s(L_i + L_g)] = R_i$. In this case, the resonant frequency is $\omega_{re} = 1/\sqrt{(L_i + L_g)C_i}$. Under the resonance frequency, the inductor current is associated with the current reference, shown in (4.27).

$$\frac{I_i}{I_{ri}} = -jR_i \sqrt{\frac{C_i}{L_i + L_g}} \quad (4.27)$$

An intuitive method is to increase the L_i , mitigating the resonance. However, it may cause a sizeable equivalent impedance of the feeder. Another way is to reduce the capacitance C_i , which is a possible way to minimize the oscillation; however, it may degrade the RoCoF in SA mode.

4.4 PROPOSED CONTROL DESIGN

4.4.1 POWER OSCILLATION MITIGATION IN SA MODE

With the parameter design proposed in the previous Section, the transient circulating current in a multi-VSG system can be theoretically eliminated. While the inertia and damping coefficient settings can be satisfied by configuring J to maintain the same ratio as D across multiple VSGs, achieving the ideal impedance ratio between different units is often impractical due to uncertainties in actual line inductances. To address this limitation, this Section derives a new VSG control strategy based on the transfer function of a two-VSG system. The oscillations can be mitigated by suitably harmonizing the virtual impedance and tuning the equivalent impedance.

Mismatched equivalent output impedance can lead to uneven sharing of reactive power. This indicates that the equivalent impedance has been well adjusted if the reactive power is proportionally distributed. This adjustment can help mitigate active power oscillations when the load is switched.

As the feeder is assumed to be inductive in this chapter for clarification, the power flowing through the feeder impedance results in a voltage drop ΔV_i , which can be expressed as:

$$\Delta V_i \approx \frac{X_{e,i} Q_i}{V_{c,i}} \quad (4.28)$$

where $X_{e,i}$ is the equivalent impedance of i -th VSG. In [73], it is demonstrated that proper design of the virtual impedance enables modification of the equivalent feeder impedance $X_{e,i}$. This adjustment, in turn, facilitates control of the voltage drop among the units, thereby promoting proportional sharing of reactive power.

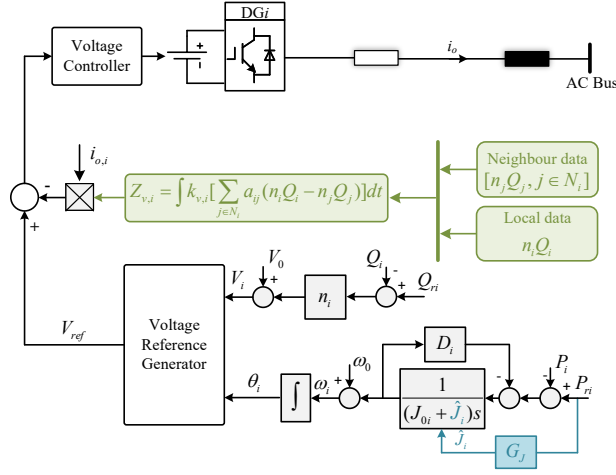


Figure 4.8: Control structure of the proposed method.

GRAPH THEORY-BASED VIRTUAL IMPEDANCE IMPLEMENTATION

The proposed method is shown in Fig.4.8, the inverters exchange information related to reactive power ($n_1 Q_1, \dots, n_n Q_n$) with their adjacent units to achieve a reactive power consensus, when the impedance has been appropriately adjusted. The reshaped consensus algorithm-based virtual fundamental impedances are expressed as (4.29).

$$Z_{v,i} = \int k_{v,i} \left[\sum_{j \in N_i} a_{ij} (n_i Q_i - n_j Q_j) \right] dt \quad (4.29)$$

where the parameter $k_{v,i}$ determines the bandwidth of the virtual impedance loop. The adaptively adjusted impedance $Z_{v,i}$ is influenced by neighboring information and the local unit's state. When reactive power sharing is uneven, the consensus algorithm prompts the controller to adjust the virtual impedance. This modification aims to achieve balanced reactive power distribution, ensuring proportional sharing across equivalent impedances.

4.4.2 POWER OSCILLATION MITIGATION IN GC MODEL

An excessively large moment of inertia J can reduce the frequency fluctuations; however, it also leads to increased power oscillations. Conversely, selecting a moment of inertia J that is too small degrades frequency stability and inertia response. Similarly, improper selection of the damping coefficient D negatively impacts oscillation and frequency deviation.

In conclusion, a more significant moment of inertia J is preferred in standalone mode to maintain the RoCoF, but it increases the oscillation among multi-VSGs. A smaller inertia J is necessary to mitigate oscillations in grid-connected mode, particularly in scenarios involving reference changes. Accordingly, the choice of inertia coefficient can be shown as in (4.30).

$$J_i = J_{0i} - \frac{\mu s}{\tau s + 1} |P_{ri}| \quad (4.30)$$

In Fig.4.8, G_j represents a high-pass filter with the transfer function $\mu s/(\tau s + 1)$. This filter extracts the high-frequency components of the power reference signal, specifically the rapidly changing parts, and feeds them forward to the inertia adjustment link. The parameters μ and τ define the characteristics of the filter and determine its bandwidth, which covers the dynamic response process of the power when the reference changes. The parameters selection is shown in Section.V. Since the microgrid dynamics are influenced by all the elements in Fig.4.4, the values of μ and τ are selected based on the VSG parameters. This method maintains the RoCoF in the SA mode because it allows the inertia to change only when the power reference changes in GC mode, thereby mitigating the associated oscillations. From the impedance circuit perspective in Fig.4.7, it can be viewed as changing the capacitance C_i in real time under GC mode. Notably, in this context, we assume that $|P_{ri}| \leq J_{oi}$ for simplicity of expression. If this requirement is not satisfied, a limiter can be introduced to constrain $|P_{ri}|$ within the allowable range.

4.5 VERIFICATION

The proposed strategy has been tested in Simulink to validate its effectiveness, where three inverters connected in parallel are considered. In this microgrid system, the output side of the inverters is connected to the AC bus through an LC filter and line impedance. The expected active power-sharing ratio is assumed to be 1:2:3.

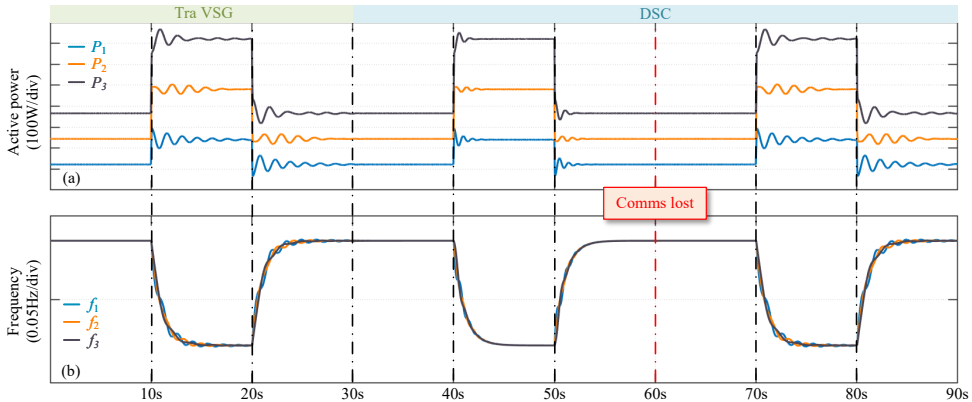


Figure 4.9: Dynamics with the distributed secondary control in [103].

4.5.1 SIMULATION RESULT

Fig.4.1 shows the simulation structure, $n = 3$. Fig.4.9 compares traditional VSG control and the distributed secondary control proposed in [103]. The output active power and frequency are displayed in Figure 4.9(a) and Figure 4.9(b), respectively.

Initially, the conventional VSG control is used to regulate the microgrids after the system starts, resulting in a proportional steady-state active power-sharing ratio of 1:2:3, as expected. At 10 seconds, a 700W load is added, which, according to the droop law, leads to an increase in active power and a decrease in frequency. However, the active power

and frequency experience severe oscillations due to the mismatched feeder impedance. When the load is suddenly switched off, the system recovers to its original power level, but oscillations persist in the dynamics. At 30 seconds, the distributed secondary control (DSC) proposed in [103] is activated, providing extra damping for the VSG system. As seen at 40 and 50 seconds, where the load is stepped on and off, the oscillations are relatively smaller than the conventional VSG control. Since DSC necessitates a communication network, it is reasonable to consider the scenario of communication loss. Therefore, the DSC performance without communication under a load switch scenario is tested. At 60 seconds, the communication is removed, indicating that the inverters can no longer receive information from each other. In this case, when the load increases and decreases at 70 and 80 seconds, respectively, the active power and frequency oscillations are equivalent to those observed under traditional VSG control, indicating that DSC loses its effectiveness in mitigating oscillations. This demonstrates that DSC is not robust against communication disruptions.

4

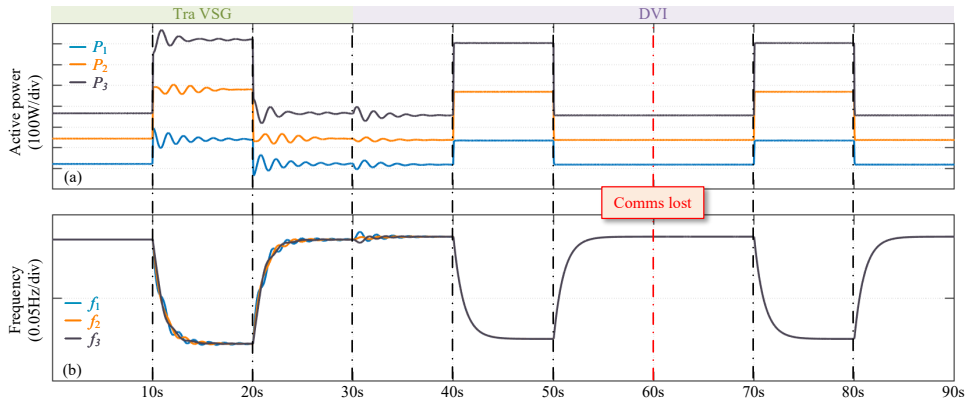


Figure 4.10: Dynamics with the proposed distributed virtual impedance.

Fig.4.10 compares the proposed distributed virtual impedance (DVI) control and the conventional VSG control. Similarly, the load increases and decreases at 10 seconds and 20 seconds, respectively, leading to active power and frequency oscillations. At 30 seconds, the distributed virtual impedance control is activated. While a slight oscillation occurs due to the tuned impedance affecting the active power slightly, the system demonstrates improved stability. When the load is switched at 40 and 50 seconds, the active power and frequency smoothly transition to their steady state without significant oscillations. This illustrates the effectiveness of the proposed DVI control method. At 60 seconds, the communication is removed. The DVI has been fixed and not changed anymore, therefore the parameters can remain matched for the rest of the operation. Consequently, even with load changes at 70 and 90 seconds under the no-communication scenario, the active power and frequency do not experience oscillations. This procedure suggests that the proposed DVI control method is more immune to communication delays and interruptions than the distributed secondary control.

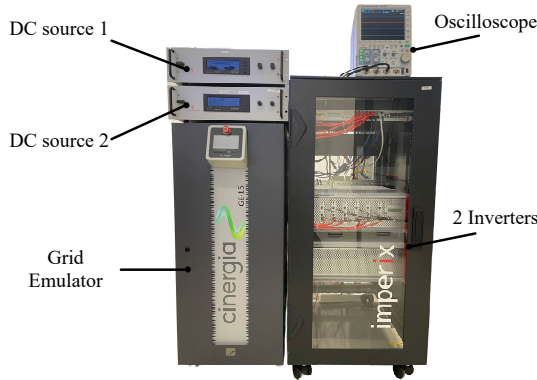


Figure 4.11: Experiment setup.

4.5.2 EXPERIMENT RESULT

The proposed adaptive control strategy has also been tested in experiments, consisting of two VSG-based inverters and an ideal grid emulator, and the experiment setup is shown in Fig.4.11.

OSCILLATION IN SA MODE

The experimental results for active power, frequency, and reactive power under different control methods are shown in Fig.4.12. In the scenario employing conventional virtual synchronous generator control, the system first undergoes a loading phase followed by an unloading phase to test its performance under varying conditions. During these transitions, significant oscillations are observed in the output active power and system frequency. These oscillations are primarily caused by the inability of conventional VSG control to effectively manage the dynamic interactions between distributed generation units, especially under changing load conditions. Moreover, the reactive power sharing among the DG units is found to be disproportionate, reflecting suboptimal coordination in the system. This disparity in reactive power distribution indicates mismatched equivalent impedances of the DG units, which can further exacerbate stability issues.

A particularly concerning observation is the poor frequency dynamic performance exhibited by the system with VSG control. Large frequency deviations not only disrupt the synchronization of DG units but also increase the likelihood of unintended load-shedding. If such deviations persist, they could escalate into system-wide instability, potentially causing extensive blackouts. This underscores the limitations of traditional VSG approaches in maintaining system resilience, especially in scenarios with high penetration of renewable energy sources.

In contrast, the proposed distributed virtual impedance method demonstrates remarkable effectiveness in mitigating these issues, as illustrated in Fig.4.13. After the system transitions and DVI control is activated, oscillations in active power and frequency are significantly reduced. The DVI method facilitates dynamic adjustments in reactive power, enabling Q_1 and Q_2 to converge toward their expected values. This improvement is at-

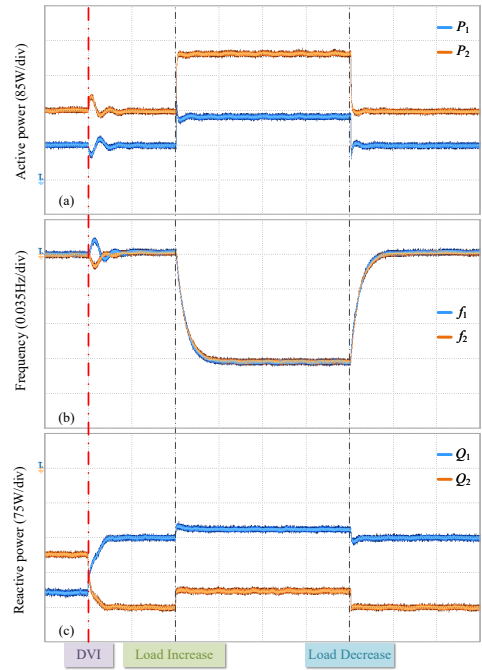
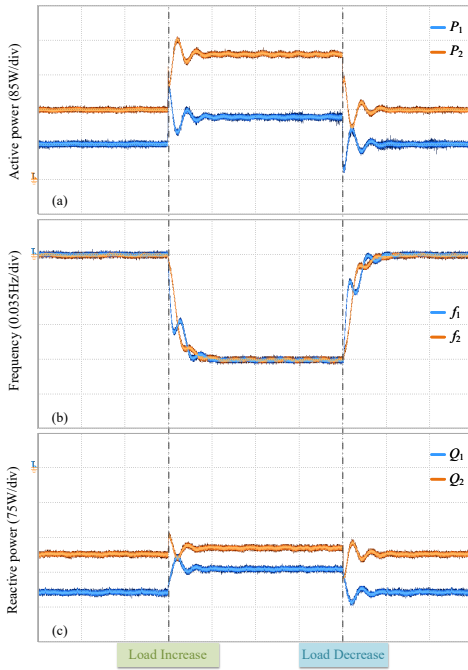


Figure 4.12: Dynamic of the VSG control in SA mode. Figure 4.13: Dynamic of the proposed control in SA mode.

tributed to the proportional adjustment of the equivalent impedance for each DG unit, ensuring accurate reactive power sharing at a ratio of 1:2.

The enhanced performance of the system is also linked to the proportional tuning of inertia and damping coefficients based on each DG's maximum output capacity and rate of change of frequency requirements. Such harmonization ensures a balanced response among all DG units, effectively eliminating the oscillatory behavior seen under VSG control. This is clearly evident in Fig.4.13, where load variations post-DVI activation do not induce oscillations in the active power or frequency. Additionally, the frequency change rate adheres to the expected trajectory, reinforcing the stability and reliability of the system under DVI control. These findings highlight the potential of DVI as a superior alternative to conventional VSG methods, particularly in modern microgrids with dynamic and variable operating conditions.

OSCILLATIONS IN GC MODE

Initially, the DG1 and DG2 output active power is 0W, while the utility grid supports an active power of 228W. Consequently, a step change of 100W is applied to the power reference of DG1 in the active power set point of the grid-tied VSG to demonstrate power oscillations. As depicted in Fig.4.14, following the increase in the power set point, significant oscillations occur in the active power outputs of both DG1 and the grid. Subsequently, similar oscillations in active power are observed when the power set point reverts to zero. Notably, the active power of DG2 remains relatively small and can be disregarded,

as discussed in the previous section. Fig.4.15 illustrates the dynamic performance of the proposed adaptive inertia method. It is evident that, under the same power reference change, the adaptive inertia method enables the involved converters and the grid power to adjust smoothly to the reference without any overshoot oscillations. The power reference change actively engages the adaptive inertia, ensuring a smooth transition in the active power outputs.

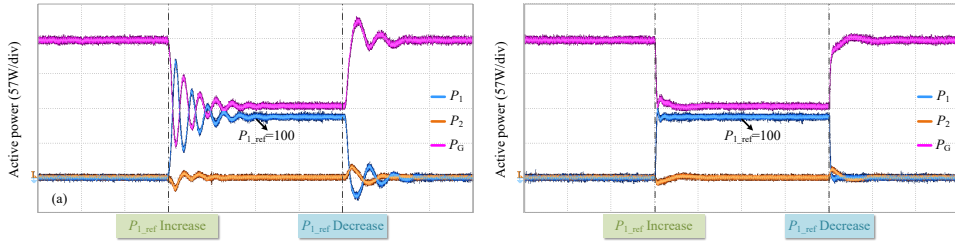


Figure 4.14: Dynamic of the VSG control in GC mode. Figure 4.15: Dynamic of the proposed in GC mode.

4.6 CONCLUSION

The VSG control can be revisited from an impedance circuit perspective, where VSG oscillations are analogous to LC resonance for an intuitive understanding of the power oscillations issue. A distributed virtual impedance is proposed to harmonize the parameters and attenuate oscillations in SA mode to address these oscillations. Additionally, a power reference feedforward-based alternative inertia control is proposed to mitigate oscillations in GC mode. The application of the proposed method yields several benefits: 1) In SA mode, power oscillations can be precisely and quickly attenuated without requiring prior knowledge of the feeder impedance. 2) In GC mode, the adaptive inertia algorithm is activated only when necessary, effectively mitigating oscillations caused by reference changes. This ensures that the adaptive inertia control is not coupled with SA mode, thereby preventing any degradation in RoCoF.

5

RESILIENCE-ORIENTED COMMUNICATION NETWORK DESIGN

5

The communication network used in distributed secondary control (DSC) for microgrid power and voltage regulation is vulnerable to cyber-attacks. While the predominantly resilient research on secondary control employs passive defense strategies, this chapter presents a proactive defense mechanism by designing the communication graph for secure microgrid operation. This approach involves developing the communication network to enhance security before attacks occur, thus allowing for a timely response. First, new metrics are introduced to quantify the impact of various cyber-attacks effectively. It then employs a multiobjective optimization method to design the communication network, considering the quantified attack impacts, convergence, time-delay robustness, and communication costs. To validate the proposed methodology, OPAL-RT simulation tests are conducted on a microgrid with ten inverter units under different scenarios.

This chapter is based on:

-J. Xiao, L. Wang, P. Bauer and Z. Qin, "Resilience-Oriented Communication Network Design for Secondary Control of Microgrids," IEEE Transactions on Industrial Informatics, under review.

5.1 INTRODUCTION

Microgrids, which manage the power flow of distributed generators, are evolving into cyber-physical systems [112]. The distributed generators, integrating renewable energy sources and energy storage devices, offer a promising solution for significant economic and environmental benefits.

For MGs control, the P - f and Q - V droop law are commonly used in the primary layer [36]. However, the droop control lacks support for reactive power sharing, primarily due to the joint influence of mismatched feeder impedance and various controller parameters [73]. Additionally, the droop control contributes to deviations in both frequency and voltage from their respective reference values [33]. To this end, the distributed secondary control has been proposed using the communication network [33]. In this way, the microgrid consensus can be reached, regardless of the initial configuration induced by different units' properties.

As a typical example of complex networks demonstrating controlled synchronization, the DSC necessitates the support of robust communication networks. In practice, communication networks are subject to constraints. For example, communication delays represent an inevitable constraint, expected to affect system performance adversely [113]. Therefore, developing time-delay robustness DSC schemes for MGs becomes critical. Recent research has investigated the impact of communication delays on DSC in [114]. In [115], a multiagent-based distributed active power controller has been designed to improve time delay robustness. Moreover, the situation becomes even more precarious since the communication networks deployed can expose microgrid components to cyber-attacks.

The cyber attack could result in deviations in bus voltages, inaccuracies in output current/power allocation, and ultimately, jeopardizing the system's stability and posing significant risks to MGs. Current researches primarily focus on three types of attacks: false-data injection attacks (FDIA) [35], denial-of-service (DoS) attacks [27], and multiple deliberate attacks (MDA) [116]. FDIA aims to manipulate transmitted information to disrupt system operation by injecting false data alongside actual transmitted data. DoS attacks can impair specific communication channels, rendering neighboring data inaccessible and consequently disrupting the connectivity of the communication system topology. Notably, DoS attacks have been stated as the most prevalent cause of cyber incidents [117]. Unlike strategically planned FDIA, DoS attacks often occur randomly, are relatively straightforward to execute, and require minimal system information. With the knowledge of the communication topology, MDA targets crucial agents [116], posing a heightened risk to system integrity. Such attacks may subject targeted inverters to sustained and aggressive assaults, potentially resulting in unplanned unit plug-out.

It is imperative to develop effective defense mechanisms to ensure the secure operation of MG systems under potential cyber threats. Current research efforts in this area are predominantly focused on developing a resilience-enhanced controller equipped with an attack detector for cyber attack mitigation. For example, a model-based detector proposed in [15, 16] identifies FDIA in power systems for attack detection. However, it is acknowledged that the malicious cyber-attacker possessing deep state information is likely to impede the state estimation [19, 21]. Model-free methods using AI-based algorithms [20] also proved an effective way to detect cyber-attacks. Nevertheless, such techniques place an extra computing load on the involved devices. Consequently, relying on sophisticated detection

algorithms can lead to delayed controller responses during attacks, which is untenable in demanding scenarios [22, 23].

The resilience scheme can be integrated into the DSC framework, with its philosophy summarized as follows: 1) isolation of corrupted links, 2) adaptive tuning of consensus gains, 3) counteraction of attack effects, and 4) reconstruction of corrupted signals. Specifically, in [27, 28], the corrupted information from neighbors is discarded by managing the connectivity of communication graphs. Besides, in [30, 35], the adaptive law-based method is introduced to enhance the resilience of the distributed system by dynamically altering the consensus gain across the associated agents. Moreover, mitigation strategies after identifying a cyber attack involve counteracting the losses caused by estimated false signals [18, 118, 119]. An event-driven mitigation strategy is proposed, replacing attacked signals with reconstructed signals [29, 120]. Reconstructing corrupted data from healthy channel sources is an effective strategy, but its effectiveness is significantly diminished in scenarios where more channels are attacked.

Despite these efforts, current strategies cannot provide microgrids sufficient resilience against attacks. This deficiency becomes apparent when the prevailing detection methods struggle to ensure system recovery under severe conditions [22, 23]. Moreover, the resilience scheme proves inadequate when faced with combined attacks [24, 25]. Furthermore, existing approaches are limited by their tendency to restrict the number of affected entities [30, 31], and the mentioned method operates only after the attack.

Based on the existing literature and our previous research [121], this chapter investigates secure communication networks for MGs as a proactive approach to preventing cyber-attacks. These networks can also integrate schemes for cyber-attack detection and resilience enhancement, thereby improving overall security. However, designing such networks requires a careful trade-off between convergence, time delay robustness, and communication cost in multi-agent systems, as explored in [122]. In particular, the DSC communication scheme, represented as an undirected graph within the microgrid control layer, highlights the importance of considering these factors to effectively regulate voltage and power dynamics [27, 123]. Moreover, while addressing the challenges posed by MDA, a novel optimal network optimization method is presented in [116]. This method balances time delay robustness and convergence while accounting for potential cyber threats. Nevertheless, its applicability may be limited in scenarios involving more aggressive MDA. Additionally, it is important to note that these network design approaches often fail to consider the adverse effects of FDIAs, which can severely disrupt power-sharing dynamics and hinder voltage recovery processes.

As summarized in Table 5.1, the existing literature highlights a notable research gap: current studies predominantly focus on passive defense mechanisms against cyber-attacks, while proactive design strategies for resilient communication networks remain underexplored. Consequently, there is a pressing need to develop secure communication graphs specifically tailored for DSC in microgrids. The primary contributions of this study are outlined below:

- A communication network topology is designed using a multi-objective optimization approach, considering factors such as convergence behavior, delays robustness, communication costs, and vulnerability to DoS, FDIA, and MDA.

Table 5.1: Comparison of the methods for enhancing MG cyber security.

Type	Defence	Method	Reference	Description	DoS	FDIA	MDA
Passive	Detection	-model based	[15, 16]	-model inaccuracy	\	\	\
		-data driven	[20, 21]	-computational burden	\	\	\
	Resilience	-isolate corrupted	[27, 28]	-degrade connectivity	\	\	\
		-adaptive gain	[30, 35]	-hybrid attack ineffective	\	\	\
		-counteract attack	[18, 118, 119]	-time consuming	\	\	\
	-reconstruct signal	[29, 120]	-limit infected sets	\	\	\	
Proactive	Prevention	-optimal graph design	[122, 123]	-converge, delay, cost	×	×	×
			[116]	-prone to severe MDA	✓	×	✗
	Prevention	-optimal graph design	proposed	-resilience oriented design	✓	✓	✓

5

- Opposed to the passive schemes in [15, 16, 18, 20, 21, 27–30, 35, 118–120], the proposed communication network design is proactive, demonstrating a faster resilience and enhancing the privacy.
- The proposed method ensures that microgrids are less affected by FDIA and MDA attacks, compared to the latest communication graph design methods introduced in [116, 122, 123].

The chapter is structured as follows: Section 5.2 derives the distributed secondary control. Section 5.3 quantifies the cyber attack and gives the communication graph design principle. Section 5.4 verifies the effectiveness of the proposed methods through simulation. Finally, Section 2.6 gives the conclusion of this chapter.

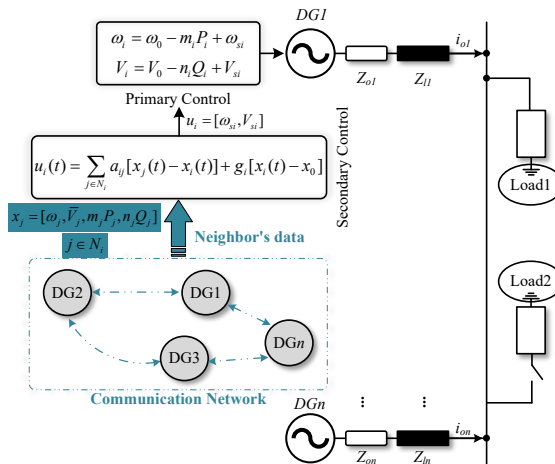


Figure 5.1: Configuration of the AC microgrid with DSC.

5.2 DISTRIBUTED SECONDARY CONTROL IN MICROGRID

In islanded MGs, as shown in Fig.5.1, the use of diverse loads necessitates proper regulation of active and reactive power and effective voltage recovery. This chapter employs communication-based distributed secondary control to coordinate the converters and achieve these objectives. The communication network connecting the participants ensures the propagation of reference information, enabling optimal operation.

The primary control investigated in this chapter is shown in (2.1) and (2.2) since the feeder characters are assumed to be inductive in this chapter. The microgrid consensus can be reached by modifying the droop control with the secondary control compensation term ω_{si} and V_{si} in (2.5) and (2.6), respectively.

The potential energy describes the disagreement of the participating units can be shown as in (5.1):

$$\Phi_G(x) = \frac{1}{2}x^T Lx + \frac{1}{2}(x - x_0)^T G(x - x_0) \quad (5.1)$$

where x represents the frequency and voltage amplitude. G is the pinning gain matrix, and $G = \text{diag}(g_1, \dots, g_n)$. Specifically, in frequency and voltage recovery control scenarios, $g_i = 1$, implying the system state is targeted to approach the reference value x_0 . Conversely, in controllers such as active power and reactive power-sharing control, $g_i = 0$.

A gradient-based feedback loop is built for compensation, $u_i(t) = -\nabla\Phi_G(x)$, as shown in (5.2). The involved units are assumed to propagate information through the prescribed communication graph \hat{G} for DSC.

$$u_i(t) = \sum_{j \in N_i} a_{ij}[x_j(t) - x_i(t)] + g_i[x_i(t) - x_0] \quad (5.2)$$

where N_i is the set of i th DG's neighbor. x_i represents the the local unit's state, ω_i , \bar{V}_i , $m_i P_i$, $n_i Q_i$. \bar{V}_i denotes the estimated global average voltage [123], which can be obtained by the dynamic average algorithm in (5.3). To compensate for the voltage deviations from the droop control, the average voltage through the MG is expected to be regulated to the rated value by a voltage restoration loop. Under the regulation, the real output voltages of all DGs lie within an acceptable range.

$$\bar{V}_i = V_i(t) + \int \sum_{j \in N_i} a_{ij}(\bar{V}_j - \bar{V}_i) dt \quad (5.3)$$

5.3 COMMUNICATION NETWORK DESIGN

Fig.5.1 illustrates an n -DG AC microgrid with secondary control, where the voltage and power control performance depends on information exchanged with neighboring units. This performance is highly influenced by the design of the communication network, which is the focus of this chapter.

This section presents six optimization criteria for designing an optimal communication network: convergence performance, resistance to communication delays, communication costs, and the negative impacts of three types of cyber attacks.

5.3.1 CONVERGENCE PERFORMANCE

1). *For active power and reactive power sharing:* The network can be modeled as an undirected graph with balanced information flow, where g_i equals zero. With the consensus law, the sum of the output of all units is invariant, and DSC adjusts the output power of each DG.

As shown in (5.4), the state x can be decomposed.

$$x = \alpha 1 + \xi \quad (5.4)$$

where $\alpha 1 = Ave(x)$ is an invariant quantity [122], $\alpha 1 = \sum_i^n x_i(0)/n$. The disagreement vector ξ satisfies $\sum_i^n \xi_i = 0$, and its dynamics is given by $\dot{\xi} = -L\xi$.

The solution to the disagreement is given by:

$$\xi \leq \xi(0)exp(-\kappa t) \quad (5.5)$$

where $\kappa = \lambda_2(L)$, representing the second smallest eigenvalues, defined as the algebraic connectivity of the connected graph [122]. A well-known observation regarding the Fiedler eigenvalue of an undirected graph is that for dense graphs, $\lambda_2(L)$ is relatively large. In contrast, for sparse graphs, $\lambda_2(L)$ is relatively small in \hat{G} . As the disagreement converges to zero, the consensus value equals the average of its initial value.

2). *For frequency and voltage recovery controllers:* The $g_i[x_i(t) - x_0]$ term is employed, the global disagreement becomes $e(t) = x(t) - x_0$. By injecting references into specific nodes, the interconnected nature of the underlying network drives the remaining nodes to converge toward the reference state.

Consider the Lyapunov function as:

$$V(t) = \frac{1}{2}e(t)^T e(t) \quad (5.6)$$

The derivative of the Lyapunov is stated as:

$$\begin{aligned} \dot{V}(t) &= -e(t)^T(L + G)e(t) \\ &\leq -\lambda_{min}(L + G)e(t)^T e(t) \\ &\leq -2\lambda_{min}(L + G)V(t) \end{aligned} \quad (5.7)$$

where $2\lambda_{min}(L + G)$ represents the corresponding convergence rate [28]. Since the minimum eigenvalue $(L + G)$ is positive-definite and inevitable, the disagreement e would eventually converge to zero, which means x_i will ultimately converge to x_0 . So, the control objectives are reached.

In this scenario, a higher convergence rate indicates that pinned DGs communicate more effectively with unpinned units. As a result, external information travels faster through the communication network within the microgrid. Therefore, selecting pinning nodes usually aims to maximize the minimum eigenvalue of the matrix $(L + G)$ to increase the convergence rate. However, as noted in [124], this upper bound is constrained by the second smallest eigenvalue of L , denoted as $\lambda_2(L)$. Given these considerations, we fix the number of pinning nodes while ensuring convergence to a reference state. Consequently, the primary focus for improving convergence performance lies in the design of the Laplacian matrix L . Therefore, we establish $F_1(\hat{G}) = -\lambda_2(L)$ as the cost function representing the convergence rate.

5.3.2 ROBUSTNESS TO COMMUNICATION DELAY

Incorporating a communication network introduces time delays in MGs' control. A detailed examination of these time delays in the coordinated operation of microgrids is provided in [125]. Such delays can potentially delay the convergence of system states and degrade the system's dynamic performance, even resulting in instability.

To gain further insight into the relation between robustness to delay and connection, we ignore the pinning node since only a few nodes are selected for pinning control, and we assume that the transmission time-delay of communication links is equal and $\tau_{ij} > 0$ [116, 122, 123]. The dynamic of the consensus protocol in (5.2) with time delay can be described as follows:

$$\dot{x}_i(t) = u_i = \sum_{j \in N_i} a_{ij} [x_j(t - \tau_{ij}) - x_i(t - \tau_{ij})] \quad (5.8)$$

The Laplace transform of both sides of (5.8) is denoted as (5.9).

$$sX_i(s) - x_i(0) = \sum_{j \in N_i} a_{ij} e^{-\tau_{ij}s} (X_j(s) - X_i(s)) \quad (5.9)$$

The Laplace transform of the above formula is:

$$X(s) = (sI + e^{-\tau_{ij}s}L)^{-1}x(0) \quad (5.10)$$

From Gregorian theorem, we know that $\lambda_{\max}(L) \leq 2d_{\max}(\hat{G})$. Where $d_{\max}(\hat{G})$ is the maximum degree of the nodes of \hat{G} . Therefore, a sufficient condition for protocol convergence is shown in (5.11). When the following condition is met, (5.8) can realize global asymptotic stability with time-delay τ_{ij} , and the state of x_i converges to the average value:

$$\tau_{ij} \in [0, \tau^*], \tau^* \leq \frac{\pi}{2\lambda_{\max}(L)} \quad (5.11)$$

where $\lambda_{\max}(L)$ is the greatest eigenvalue of L . τ^* is the maximum tolerable communication time delay of the DSC. One concludes that the upper bound on the admissible channel time delay in the network is inversely proportional to the largest eigenvalue of the Laplacian matrix.

This means that networks with nodes with relatively large degrees cannot tolerate high communication time delays. Therefore, we set the cost function as: $F_2(\hat{G}) = 4d_{\max}(\hat{G})/\pi$.

5.3.3 COMMUNICATION COST

A crucial consideration in distributed multi-agent systems involves minimizing communication expenses. We define the communication cost, denoted as C , about the total count of edges within the graph \hat{G} , as detailed in (5.12):

$$C = \sum_{i=1}^n d_i/2 \quad (5.12)$$

In general, more edges mean higher communication costs. Based on the graph, the optimal objective is to minimize the required edges, denoted as $F_3(\hat{G}) = \sum_{i=1}^n d_i/2$.

5.3.4 INVULNERABILITY DESIGN OF COMMUNICATION NETWORK

The proposed DSC framework heavily depends on exchanging parameters $x_i = \{\omega_i, \bar{V}_i, m_i P_i, n_i Q_i\}$ among distributed generators, thereby rendering the cyber-physical system susceptible to cyber-attacks. The cyber attacks considered in this chapter, DoS and FDIA, are shown in (2.11). If a converter is severely compromised by multiple deliberate attacks, it is forced to drop out, resulting in a loss of connection to the rest of the microgrid.

METRIC OF DoS ATTACK EFFECT

Based on the above discussions, the DoS attack metric $F_4(\hat{G})$, is defined as (5.13).

$$F_4(\hat{G}) = 1/[1 + \lambda_2(L)] \quad (5.13)$$

The connection relationship of the participating units is different for various graph structures. When a DoS attack challenges the communication link, the information propagation is interrupted, resulting in a low convergence rate [27]. Notably, with a more extensive convergence connectivity of the original graph, the system features a minor effect of the DoS attack. For connected systems, the attack metric negatively correlates with the algebraic connectivity $\lambda_2(L)$.

5

METRIC OF FDIA EFFECT

With the pinning control in [115], we first reframe the frequency/voltage recovery into a pinning synchronization problem. This approach allows a subset of DGs, or even a single DG, to access predefined reference values while all other units synchronize via communication links among the participating DGs. The FDIA can be considered a modification of these reference values, so its effect depends on the number of pinning nodes. Consequently, we transform the active/reactive power-sharing problem into an undirected graph consensus problem, where each DG adjusts its power outputs based on the outputs of its neighbors. Here, the influence of the FDIA on power sharing is mainly shaped by the differences in frequency/voltage propagation rates throughout the graph.

Herein, the active power-frequency loop (P - f) is considered as an example for verification, and the secondary control can be written as (5.14).

$$\dot{\omega}_{si} = \sum_{j \in N_i} a_{ij}(\omega_j - \omega_i) + g_i(\omega_0 - \omega_i) + \sum_{j \in N_i} a_{ij}(\delta_j - \delta_i) \quad (5.14)$$

where $\delta_i = m_i P_i$ is the power sharing coefficient. Considering FDIA, the global auxiliary control input is written as:

$$-[\dot{\omega} + \dot{\delta}] = (L + G)(\omega - \omega_0) + L\delta + B\varepsilon \quad (5.15)$$

where $B = \text{diag}\{b_1, \dots, b_n\}$, b_i is the corresponding matrix of FDIA. In a power system, all the DGs' frequencies synchronize to the common microgrid frequency in the steady state. Therefore, one can obtain.

$$L\omega = 0 \quad (5.16)$$

Setting the left side of (5.15) equal to zero, and considering (5.16) yields:

$$L\delta + G(\omega - \omega_0) + B\varepsilon = 0 \quad (5.17)$$

Without any limitation, it is assumed that if $g_i = 1$, the unit has access to the reference. $b_i \varepsilon_i \neq 0$ means the neighbor of selected i th-DG is under FDIA. Therefore, the commensurate form of (5.17) can be written as (5.18):

$$\begin{aligned} & \begin{bmatrix} \sum_{j=1}^n a_{1j} & -a_{12} & \cdots & -a_{1n} \\ -a_{21} & \sum_{j=1}^n a_{2j} & \cdots & -a_{2n} \\ \vdots & \vdots & \ddots & \vdots \\ -a_{n1} & -a_{n2} & \cdots & \sum_{j=1}^n a_{nj} \end{bmatrix} \begin{bmatrix} \delta_1 \\ \delta_2 \\ \vdots \\ \delta_n \end{bmatrix} \\ & + \begin{bmatrix} g_1(\omega_1 - \omega_0) \\ g_2(\omega_2 - \omega_0) \\ \vdots \\ g_n(\omega_n - \omega_0) \end{bmatrix} + \begin{bmatrix} b_1 \varepsilon_1 \\ b_2 \varepsilon_2 \\ \vdots \\ b_n \varepsilon_n \end{bmatrix} = 0 \end{aligned} \quad (5.18)$$

To make a determinant transformation on (5.18), add the elements of the first $(n-1)$ rows to the elements of the n th row to obtain (5.19).

$$\begin{aligned} & \begin{bmatrix} \sum_{j=1}^n a_{1j} & -a_{12} & \cdots & -a_{1n} \\ -a_{21} & \sum_{j=1}^n a_{2j} & \cdots & -a_{2n} \\ \vdots & \vdots & \ddots & \vdots \\ 0 & 0 & \cdots & 0 \end{bmatrix} \begin{bmatrix} \delta_1 \\ \delta_2 \\ \vdots \\ \sum_{i=1}^n \delta_i \end{bmatrix} \\ & + \begin{bmatrix} g_1(\omega_1 - \omega_0) \\ g_2(\omega_2 - \omega_0) \\ \vdots \\ \sum_{i=1}^n g_i(\omega_i - \omega_0) \end{bmatrix} + \begin{bmatrix} b_1 \varepsilon_1 \\ b_2 \varepsilon_2 \\ \vdots \\ \sum_{i=1}^n b_i \varepsilon_i \end{bmatrix} = 0 \end{aligned} \quad (5.19)$$

We can obtain the relationship between the attack element and frequency by solving the matrix of (5.19). It is reasonable to assume that the frequency of each inverter among the microgrid is the same in the steady state, which in turn yields:

$$\omega_i = \omega_0 + \sum_{i=1}^N b_i \varepsilon_i / 1_N^T G 1_N \quad (5.20)$$

where $N=\{1, \dots, n\}$ is the DG set. Without the loss of generality, we assume that all n DGs are selected to be pinned. The state error e_i , expected to be 0, is the error between the i -th inverter's frequency and the reference frequency, i.e., $e_i = \omega_i - \omega_0$. If no cyber attacks exist in the microgrid system, $e(t)$ will gradually reduce to a value close to zero. When FDIA exists, we assume the attack signal can be expressed as ε_i as discussed. The effect of FDIA on frequency performance is $\sum_{i=1}^N b_i \varepsilon_i / (1_N^T G 1_N)$. As observed, the FDIA concerning frequency is independent of the communication matrix L . Attack elements and the reference node determine the frequency converge error.

In addition, in an inverter-connected system, we have the output active power of each DG can be written as (5.21):

$$P_i \approx V_{c,i} V_p \int (\omega_i - \omega_p) / X_i \quad (5.21)$$

where X_i denotes the feeder impedance, the relationship between the output power of DGs and their angular frequency, and the bus angular frequency is established (5.21). Moreover, the frequencies of all DGs have been known to synchronize to a common value, even under FDIA [28]. However, the frequency adjustment will cause phase differences in the dynamic process, and this may result in improperly shared output power.

Based on the discussion above, one can establish an index to quantify the FDIA effect on active power and reactive power sharing performance as (5.22), (5.23).

$$\Lambda(i) = \{l(i, 1), l(i, 2) \dots l(i, j)\}, j \in N_i \quad (5.22)$$

where $l_{i,j}$ denotes the length of links directed from the node j to node i . $\Lambda(i)$ represents a vector composed of the length of the communication path from all other nodes in the graph to node i .

$$F_5(\hat{G}) = \max_Var\{\Lambda(i)\}, i \in N \quad (5.23)$$

$F_5(\hat{G})$ denotes the global propagation rate from one DG to the remaining per unit time. $Var\Lambda(i)$ represents the variance of the vector, signifying the difference in time consumption for the error information transmitted from unit i to other units. This variance significantly influences power-sharing performance, as it causes power changes to be abnormal, as discussed. The \max function selects the maximum variance to account for the worst-case scenario.

METRIC OF MDA EFFECT

Deliberate attacks occur when hackers indiscriminately target each unit to force it offline, thereby disrupting power regulation. In such cases, the probability of each DG being attacked is equal. However, hackers typically resort to random attacks when they lack knowledge of the communication topology. Conversely, if they gain information about the topology through specific means, they selectively attack critical communication units. Under MDA in MGs, the attacked inverter is disconnected, and the compromised communication unit becomes inoperable, unable to send or receive interaction information [116].

In this case, the remaining DGs are expected to strive to maintain power-sharing performance to the greatest extent possible. In this context, there should be as few independent units as possible, ensuring the continuity of power-sharing capabilities among the operational inverters. $F_6(\hat{G})$ denotes the survivability of the MGs when it is under MDA.

$$F_6(\hat{G}) = \sum_{m=1}^n [n_m - rank(L_m)] / m^2 \quad (5.24)$$

where m represents the number of DGs plugged out from the microgrid due to the deliberate cyber attack. n_m represents the remain DGs which are in operation after m DGs are attacked,

$n_m = n - m$. L_m is the Laplacian matrix of the graph where m units are out from the graph. The attack metric is nearly inversely proportional to $rank(L_m)$ for a given MDA. Lower $rank(L_m)$ represents more isolated units and higher attack metrics. The worst case is that the attack metric reaches the upper limit m when $rank(L_m) = 0$. At this time, no available DGs exist in cyber topology.

5.3.5 OPTIMAL COMMUNICATION GRAPH DESIGN

To balance the cyber attacks' effect and dynamic performance requirements, we formulate an optimization problem aimed at reconfiguring the network's topology to balance the cyber attacks' effect and general dynamic requirements. This formulation considers six key performance indices: cyber converge rate, robustness to communication delays, communication cost, resilience to Dos, resilience to FDIA, and resilience to MDA, as summarised in Tab.5.2. Then, a multi-objective optimization method that considers the developed indexes is developed in this chapter. The optimize goal is to minimize cost function for n -DGs, therefore capturing the optimal network as shown in (5.25):

$$\begin{aligned} \min F = & (\vartheta_1 \frac{F_1 - F_{1,min}}{F_{1,max} - F_{1,min}} + \vartheta_2 \frac{F_2 - F_{2,min}}{F_{2,max} - F_{2,min}} \\ & + \vartheta_3 \frac{F_3 - F_{3,min}}{F_{3,max} - F_{3,min}} + \vartheta_4 \frac{F_4 - F_{4,min}}{F_{4,max} - F_{4,min}} \\ & + \vartheta_5 \frac{F_5 - F_{5,min}}{F_{5,max} - F_{5,min}} + \vartheta_6 \frac{F_6 - F_{6,min}}{F_{6,max} - F_{6,min}}) \end{aligned} \quad (5.25)$$

where F_1 - F_6 denote distinct objective functions aligned with specific performance criteria, encompassing convergence performance, robustness to time delays, and cost-effectiveness, metrics of DoS, FDIA, and MDA, respectively. ϑ_1 - ϑ_6 are the weights corresponding to $F_1(\hat{G})$ - $F_6(\hat{G})$. $F_{i,min}$ and $F_{i,max}$ are the *minimum* and *maximum* values, which can be obtained by solving the corresponding single-objective optimization problem. Notably, we normalized each objective function to minimize the impact of magnitude differences between objectives on weight assignment. Since there is no preference for this chapter, assigning equal weights is reasonable. Moreover, the weight design can be adapted based on the specific requirements of the grid operator.

Table 5.2: The quantification of the involved indexes.

Controller	Dynamic	Decision	Convergence	Delay-bound	Comms-cost	DoS-metric	FDIA-metric	MDA-metric
V&f	$\dot{\xi} = -L\xi$	$\sum_{i=1}^n \frac{x_i(0)}{n}$	$\kappa = -\lambda_2(L)$	$\frac{4d_{max}(\hat{G})}{\pi}$	$\sum_{i=1}^n \frac{d_i}{2}$	$\frac{1}{1 + \lambda_2(L)}$	$\sum_{i=1}^n \frac{b_i \varepsilon_i}{1_N^T G 1_N}$	$\sum_{m=1}^n \frac{n_m - rank(L_m)}{m^2}$
P&Q	$\dot{e} = -(L + G)e$	x_0	$\kappa = -\lambda_{min}(L + G)$	$\frac{4d_{max}(\hat{G})}{\pi}$	$\sum_{i=1}^n \frac{d_i}{2}$	$\frac{1}{1 + \lambda_2(L)}$	$\max_Var\{\Lambda(i)\}$	$\sum_{m=1}^n \frac{n_m - rank(L_m)}{m^2}$

The comprehensive procedure for optimal network design includes the selection of the feasible communication graph, determining Pareto bounds for multiobjective optimization,

and selecting the optimal topology. The determination of Pareto frontiers for different DG configurations is performed as follows:

1). Map all possible networks: For each MG system size, the possible range of possible networks must be determined. Essentially, a sequential series of $1 \sim n$ DG units can form $(n - 1)n/2$ networks.

2). Selection of feasible networks: Considering that these interconnected networks typically yield some homogeneous counterparts with identical eigenvalues and algebraic connectivity, further investigation is required based on graph unit degree. In addition, the feasible network is expected to have an even degree due to the need for plug-and-play capability, thus limiting the candidate networks to $n - 2$ types.

3). Optimal network selection: Scanning the candidate DG set for operational MG case and searching the related Pareto optimal networks according to the performance indices. In particular, the emphases correspond to different evaluation functions, leading to various optimal networks.

5

5.4 VERIFICATION

The efficiency of the proposed optimal design algorithm for distributed secondary control is evaluated using a real-time simulator, OPAL-RT. The simulation structure is shown in Fig.4.1. Specifically, the study focuses on a test microgrid configuration consisting of 10 DGs, and the method is scalable for larger microgrids. The basic parameters are as follows: $V_0 = 190\text{ V}$, $\omega_0 = 314\text{ rad/s}$, and $m_1 = n_1 = 1/400$. The other droop coefficients are configured to ensure the active and reactive power sharing ratios follow $DG1 : DG2 : DG3 : DG4 : DG5 : DG6 : DG7 : DG8 : DG9 : DG10 = 1 : 1.5 : 2 : 2.5 : 3 : 3.5 : 4 : 4.5 : 5 : 5.5$. The LC filter parameters are the same for all DGs, with capacitance $C_f = 12\ \mu\text{F}$, inductance $L_f = 2.2\text{ mH}$, and feeder impedance $Z_f = 2.2\text{ mH}$. As we enable the secondary control as shown in (5.2), the active power and reactive power can be facilitated to be proportionally shared, and frequency and global voltage amplitude can be restored to reference.

Based on the previous description, we optimize the communication topology of the tested MG with 10 DGs. The network's edge count must fall within the range of 9 to 45, as specified. Furthermore, it is noteworthy that multiple network configurations can arise from a given set of communication links. For instance, there are $C_{45}^{10} + C_{45}^{11} + \dots + C_{45}^{45}$ kinds of communication connection methods with the 10 units case. The optimization burden is exponentially increased with the explosion of the involved units.

In MGs, ensuring robustness in both plug-and-play capabilities is essential. This necessitates an evenly distributed degree of connectivity among units within the communication topology, ensuring uniformity in communication links across all units. Such uniformity serves to mitigate the impact of a single DG shutdown on the remaining units. Consequently, achieving this uniform degree distribution becomes a prerequisite for selecting a feasible network configuration. Nevertheless, various communication graph structures may still exist even with uniform degrees among units. As shown in comparative studies in this section, symmetrical communication graphs have been shown to be effective in increasing resilience against deliberate cyber-attacks. Consequently, identifying an optimal communication graph involves prioritizing symmetry. In light of these considerations, the candidate optimal graph can be determined by analyzing \hat{G}_1 to \hat{G}_8 as shown in Fig.5.2.

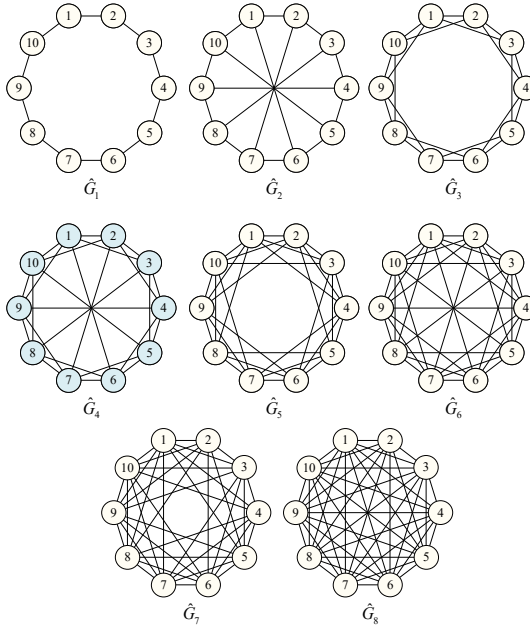


Figure 5.2: The optimal communication network candidates.

To compromise the proposed six indexes, including the dynamics and cyber attack effect of the consensus-based secondary voltage control strategy, and select the optimal performance point. This study adopts the normalization method for the optimization results of the objective function $F_1(\hat{G}) - F_6(\hat{G})$, with each weighting coefficient set as $\vartheta_1 = \vartheta_2 = \vartheta_3 = \vartheta_4 = \vartheta_5 = \vartheta_6 = 1/6$ [123]. The values of the objective functions are summed as a performance evaluation index.

Table 5.3: Optimal communication graph selection.

Graph	F_1	F_2	F_3	F_4	F_5	F_6	F
\hat{G}_1	-0.38	2.55	10	0.72	1.94	2.00	0.667
\hat{G}_2	-1.38	3.82	15	0.42	0.61	1.47	0.410
\hat{G}_3	-1.76	5.09	20	0.36	0.50	1.25	0.389
\hat{G}_4	-3.76	6.37	25	0.21	0.28	1.19	0.332
\hat{G}_5	-4.38	7.64	30	0.19	0.25	1.10	0.345
\hat{G}_6	-6.38	8.91	35	0.14	0.19	1.08	0.335
\hat{G}_7	-8	10.19	40	0.11	0.11	1.06	0.338
\hat{G}_8	-10	11.46	45	0.09	0	1.04	0.333

The index values corresponding to $\hat{G}_1 - \hat{G}_8$ are presented in Tab 5.3. Notably, the computed index value for \hat{G}_4 is the smallest among the alternatives. Consequently, the communication network associated with \hat{G}_4 is taken as optimal.

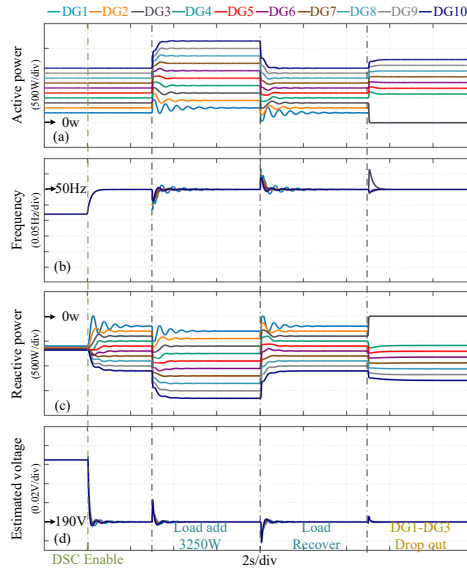


Figure 5.3: Dynamics of optimal graph \hat{G}_4 under 100ms delay.

OPTIMAL COMMUNICATION NETWORK VALIDATION

To demonstrate that the optimized communication topology has good dynamic performance, we test the \hat{G}_4 under communication delay, load switch, and plug-and-play operation. The optimal communication topology has 10 DGs and 25 communication links proposed in this chapter, and the unit degree of each DG is equal to 5.

Fig.5.3 shows the performance of the optimal graph. The output active power, frequency, reactive power, and global of the involved inverters are displayed in the subfigure of Fig.5.3- Fig.5.10, respectively. 100ms time delay is tested in the system, as it is claimed that the communication technologies used in MGs have a latency of less than 100ms [83].

As seen at the start of the simulation procedure, the active power is synchronized among the participating DGs, as frequency is a global variable. After the distributed secondary control is enabled at 2s, the reactive power can be proportionally shared while the frequency and global voltage amplitude are recovered to its reference. Then, a load increase and decrease (3250W) for both active and reactive power at 5s and 10s, respectively. At 15s, DG1, DG2, and DG3 drop out, while the remaining inverters DG4-DG10 can keep synchronization.

It should be noted that, even with the communication delay, the optimal graph can reach the consensus. The decaying fluctuation observed at the dynamic switch point is caused by the imposed communication delay. The ultimate convergence validates the effectiveness of the proposed optimization method.

COMPARATIVE STUDY I

A comparative analysis is performed among the existing communication networks to demonstrate the validity of the proposed network design methodology. The first optimal graph, defined in [123] and shown in Fig.5.4(a), consists of 14 edges. To ensure a fair

comparison, the second optimal network is constructed using the proposed optimization method, where the communication cost is also constrained to 14 edges, as shown in Fig.5.4(b).

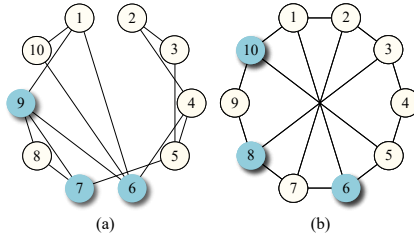


Figure 5.4: Communication network of the MG with 14 edges: (a) Optimal network in [123]. (b) Proposed optimal network.

2.1) Comparison study against FDIA: To begin with, we provide a comprehensive investigation of the dynamics of DSC when the system is under FDIA. Fig.5.5 and (b) showcase the active power sharing coefficient ($m_i P_i$), frequency (f_i), reactive power sharing coefficient ($n_i Q_i$) and estimated global voltage (\bar{V}_i) of each graph.

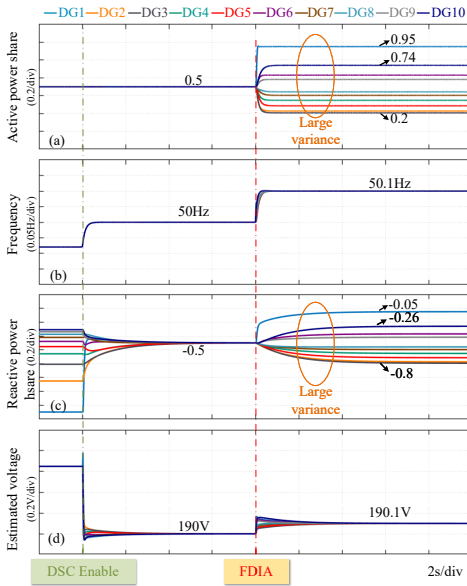


Figure 5.5: Optimal graph in [123] under FDIA.

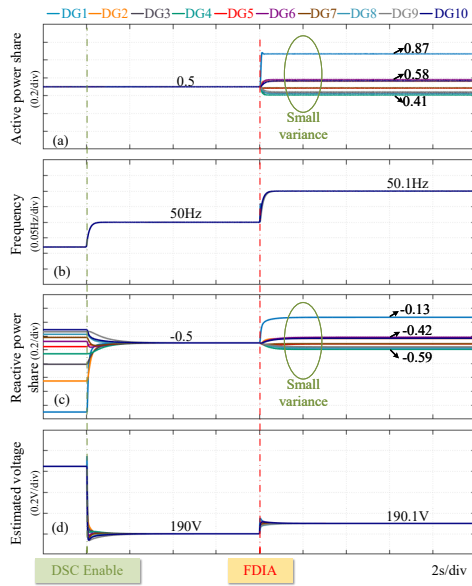


Figure 5.6: Proposed optimal graph under FDIA.

Following the established protocol, for both two graphs, the secondary control is initiated at 2s. Synchronization is gradually researched, where $m_1 P_1 = m_2 P_2 = \dots = m_{10} P_{10} = 0.5$ and $n_1 Q_1 = n_2 Q_2 = \dots = n_{10} Q_{10} = -0.5$ At 10s, an FDIA is introduced, targeting the communication link from DG_{10} to DG_1 , wherein a falsified power value of 2200W is

inserted into the original data for both active and reactive power. As a result, the frequency is driven to 50.1 Hz, while the global voltage is altered to 190.1.

When FDIA occurs in the MGs, the power-sharing coefficient exhibits considerable variance with the graph in [123]. This variance is illustrated through the wide distribution of the power-sharing coefficients among the 10 DGs, as depicted in Fig.5.5. The power-sharing coefficients span from $m_4P_4 = 0.2$ to $m_1P_1 = 0.95$ for active power, deviating significantly from the anticipated value of 0.5. Likewise, the minimum coefficient recorded for reactive power is $n_4Q_4 = -0.8$, while the maximum coefficient stands at $n_1Q_1 = -0.05$.

Conversely, employing the proposed optimal graph, as depicted in Fig.5.6, mitigates the impact of FDIA, resulting in a reduced variance of the power-sharing coefficients. Comparative analysis reveals that in contrast to the communication graph from [123], the power-sharing coefficients of each DG align more closely with the expected value of 0.5. This observation underscores the efficacy of the proposed optimal network in mitigating the effects of FDIA. Importantly, it is noteworthy that the deviations observed in the frequency and voltage steady states remain consistent between the two graphs, as both utilize the same number of pinning DGs.

5

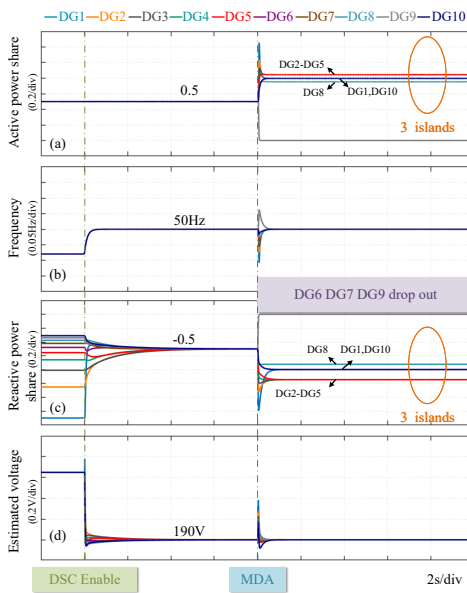


Figure 5.7: Optimal graph in [123] under MDA.

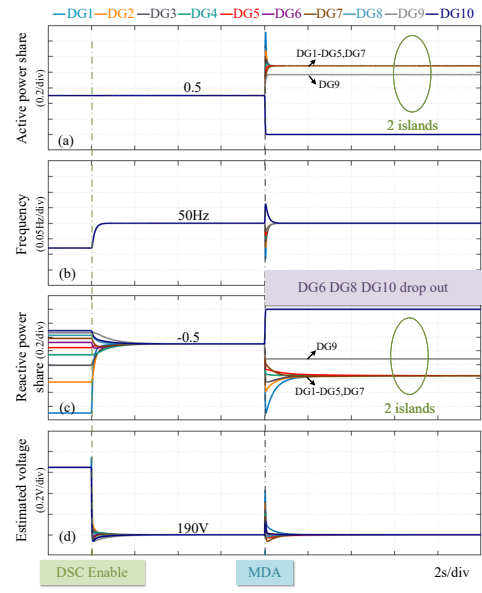


Figure 5.8: Proposed optimal graph under MDA.

2.2) Comparison study against MDA: Then, the resilience of the graph against deliberate attacks is studied. Fig.5.7 and Fig.5.8 show the dynamic performance of the different communication graphs described in Fig.5.4 when challenged by multiple deliberate cyber-attacks. Similarly, the distributed activated at 2s contributes to synchronization among the participating inverters. At 10s, The MDA occurs, which can lead to DG dropping out one by one. It is assumed that 3 DGs dropped out because of the attack. Considering the worst case, the hacker tempts to disrupt the overall synchronization by making the

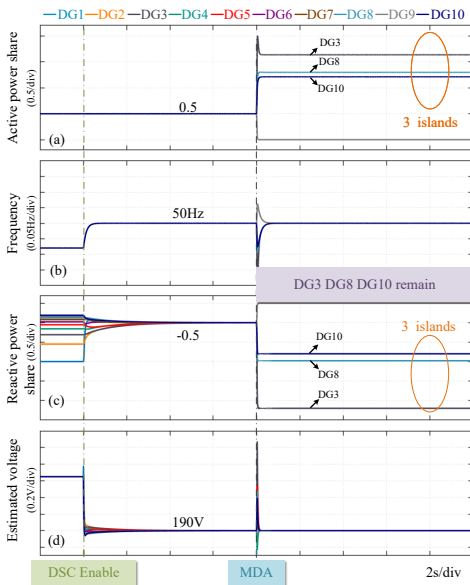


Figure 5.9: Optimal graph in [116] under MDA.

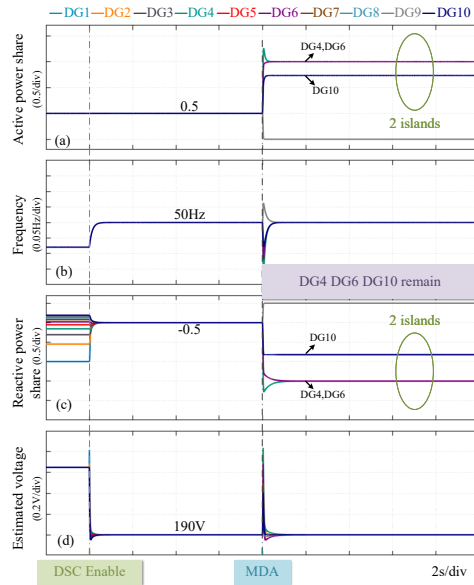


Figure 5.10: Proposed optimal graph under MDA.

operational MG system feature as many isolated nodes as possible. With the MDA, the optimal graph developed in [123] has 3 isolated island, $\{8\}$, $\{1, 10\}$, $\{2, 3, 4, 5\}$ in worst case, where DG6, DG7, and DG9 are assumed to be dropped out. However, for the worst case in the proposed optimal graph, there are only two isolated islands at most, $\{9\}$, and $\{1, 2, 3, 4, 5, 7\}$ where DG6, DG8, and DG10 are plugged out. This illustrates the benefits against MDA of the proposed optimization over the graph in [123].

COMPARATIVE STUDY II

Another comparative study is conducted to assess further the efficacy of the proposed design methodology in enhancing resilience against cyber-attacks. For the research in [116], each DG communicates with four other DGs, as depicted in Fig.5.11(a). To ensure a fair comparison, a 30-edge communication graph is constructed utilizing the proposed optimization method, as illustrated in Fig.5.11(b). The dynamic response to multiple deliberate attacks of the communication graph proposed in [116] and the proposed optimized graph are presented in Fig.5.9 and Fig.5.10, respectively.

The DSC is activated from the interval from 2s, and the active power and reactive power is proportionally shared among the DGs, as well as ensuring synchronization of frequency and voltage. At 10s, the MDA is instigated, leading to the malicious disabling of certain DGs. The attacker aims to disrupt synchronization within the DSC communication graph to the maximum extent possible. Based on pre-existing knowledge of the graph, it is reasonably assumed that the MDA targets seven units, resulting in their deactivation.

Observing Fig.5.9, it becomes evident that, under MDA, adopting the graph configuration described in [116] leaves DG3, DG8, and DG10 operational within the microgrid. Consequently, three isolated islands $\{3\}$, $\{8\}$, and $\{10\}$ emerge. Conversely, as illustrated in

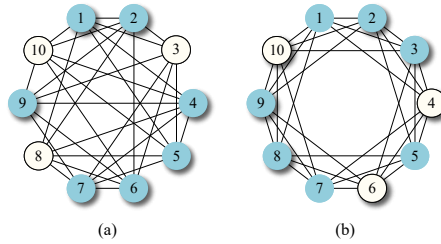


Figure 5.11: Communication network of the MG with 30 edges: (a) Optimal network in [116]. (b) Proposed optimal network.

Fig.5.10, utilizing the proposed optimal graph leads to the continued operation of DG4, DG6, and DG10 even under the most adverse conditions. Specifically, only two isolated islands form, namely $\{4, 6\}$ and $\{10\}$. This marked discrepancy underscores the superior resilience of the proposed optimal graph in maintaining synchronization across the entire MG in the face of MDA. Notably, while the number of units subjected to disconnection could range from 1 to 9, selecting 7 units for the attack lies in the negligible differences in dynamic performance resulting from other choices, owing to the inherent similarity of communication graph configurations.

5

5.5 CONCLUSION

The present study proposes an approach to optimize the communication graph for DSC, focusing on enhancing resilience against attacks. The method aims to minimize the impact of attacks on power and voltage regulation. To achieve this, novel metrics are developed to quantitatively assess the effects of DoS, FDIA, and MDA. Subsequently, a multiobjective optimization technique is employed to develop the communication graph, considering the quantified attacks, convergence, time-delay robustness, and communication cost. Unlike real-time cyber attack detection and counteraction, the proposal is microgrid planning, which is implemented during the development stage of the microgrid and remains unchanged, preparing resilience before the attacks go to the secondary control layer. Consequently, the proactive design approach makes the microgrid less affected by these attacks.

6

CONCLUSION

This thesis explores the resilient coordinated control of AC microgrids, offering practical tools and theoretical insights for grid operators, researchers, policymakers, and equipment manufacturers. It addresses key challenges in voltage and power regulation by focusing on five critical research questions essential for ensuring the reliable and efficient operation of microgrids. The work is organized into four chapters, each examining a specific aspect: frequency and voltage restoration, power sharing and voltage quality, active power dynamic management, and communication network design for enhanced cyber resilience. The key contributions and findings for each question are summarized below:

Q1 *What are the key design and implementation strategies for distributed secondary control to achieve effective frequency and voltage restoration in microgrids?*

The AC microgrid benefits flexibility, efficiency, and reliability. It can operate in grid-connected mode or be isolated from the utility grid when necessary. In the stand-alone mode, the droop control provides voltage support. However, it can lead to frequency and voltage amplitude deviations.

Chapter 2 introduces a distributed secondary control method to correct these deviations. This approach does not require prior knowledge of the converter's design details, such as control parameter values and circuit parameters. Instead, each converter adjusts its state based on the information from its neighbors. By treating each converter as an autonomous node and leveraging communication technology, all nodes involved can eventually reach a consensus, regardless of initial state differences. Furthermore, for precise control decisions, it is emphasized that the secondary loop should be designed based on the primary loop's bandwidth. Consequently, the proposed secondary control accurately restores both frequency and voltage.

Q2 *How to achieve power-sharing without degrading the AC bus voltage quality in the absence of prior system knowledge?*

The key performance indicators of microgrids include proportional power sharing and PCC voltage. Due to mismatched feeder impedances in AC microgrids, it is challenging to accurately share active, reactive, and harmonic power while ensuring PCC voltage

quality. Frequency and voltage amplitude compensation can achieve power-sharing goals. However, this method requires continuous communication, which increases the communication burden. Virtual impedance can compensate for the feeder impedance difference. Nevertheless, it causes a significant voltage drop, which degrades the PCC voltage. Because of the conflicts between these performance indicators, it is essential to consider these two indicators in the distributed controller.

Chapter 3 proposes a virtual impedance based on distributed philosophy to solve this power sharing and voltage quality problem. The proposed method regulates the fundamental and harmonic impedance to the desired values by exchanging information with neighboring inverters. In addition, distributed model predictive control-based virtual impedance is investigated, which benefits from better dynamic performance. Furthermore, the different feeder characteristics are studied, as the different characteristics significantly affect the controller design. This distributed approach eliminates the need for a central controller and reduces the communication burden. The experiments validate the effectiveness of the proposed method for power sharing and voltage quality improvement.

Q3 How to enhance the resilience of secondary control of microgrids against cyber attacks?

Communication-based distributed secondary control is essential for achieving consensus in islanding AC microgrids. However, these microgrids become susceptible to cyber-attacks with limited global information. Such attacks can falsify communication signals, disrupt power dispatch, or even induce blackouts by pushing the microgrids beyond their safe operational limits and triggering protective mechanisms. Among various types of cyber-attacks, False Data Injection Attacks and Denial-of-Service attacks are the two most widely discussed in the context of microgrids. FDIA can be modeled as the injection of false data, while DoS attacks involve the failure to receive information from neighboring converters. These attacks compromise the confidentiality, integrity, and availability of information within the microgrid, disrupt control objectives, and destabilize the system.

Chapters 2 and 3 investigate resilient algorithms to counter these threats. One approach involves blocking corrupted signals to prevent false data from affecting the entire system, though this may degrade convergence. Another method reconstructs the attacked signal from normal data, limiting the impact on infected units. Additionally, optimally weighting the signal ensures that corrupted signals are exponentially attenuated when they deviate from the norm, even under multiple attacks. Experimental results demonstrate that these resilience strategies do not adversely affect normal microgrid operation.

Q4 How can oscillations be dampened for multiple virtual synchronous generators?

The transition from droop control to VSG control can introduce oscillatory dynamics that complicate the system, potentially leading to significant frequency and active power oscillations. These oscillations occur in grid-connected mode and when multiple VSGs operate in stand-alone mode. The large instantaneous currents associated with these oscillations can trigger overcurrent protection mechanisms, exacerbating system stability issues. Consequently, the design of active power dynamics must be approached with caution. In the stand-alone mode, the interaction among the involved converters causes oscillation because of the difference between the VSG's control parameter and feeder impedance. When connected to the utility grid, the output active power must accurately

track the power reference. Therefore, the VSG can be modeled as a second-order system to explain the oscillations in grid-connected mode.

Chapter 4 proposes the equivalent circuit models of a converter with VSG control in both modes, which intuitively reveals the root cause of active power oscillations. Accordingly, a graph-theory-based virtual impedance is introduced to harmonize parameters among involved VSGs, effectively eliminating oscillations in SA mode. As for the grid-connected mode, the APOs are attenuated through the proposed adaptive inertial coefficient, which is dynamically tuned via a feedforward loop. Simulation and experimental results verify the improvements of the proposed control.

Q5 How to optimize the communication network for distributed control?

The communication network used in distributed secondary control for microgrid power and voltage regulation is vulnerable to cyber-attacks. The cyber attack could result in deviations in bus voltages, inaccuracies in output current/power allocation, and ultimately, jeopardizing the system's stability and posing significant risks to MGs. Unlike strategically planned FDIA, DoS attacks often occur randomly and require minimal system information. Moreover, with the knowledge of the communication topology, MDA targets crucial agents, posing a heightened risk to system integrity. The predominantly resilient research on secondary control employs passive defense strategies that take effect after the attack occurs.

Chapter 5 presents a proactive defense mechanism by designing the communication graph for secure microgrid operation. This approach involves developing the communication network to enhance security before attacks occur, while the existing network design ignores it. New metrics are introduced to quantify the impact of various cyber-attacks effectively. It then employs a multiobjective optimization method to design the communication network, considering the quantified attack impacts, convergence, time-delay robustness, and communication costs. Simulation tests are conducted on a microgrid under different scenarios to validate the proposed design method of the communication network.

BIBLIOGRAPHY

REFERENCES

- [1] R. L. Singh and P. K. Singh, "Global environmental problems," *Principles and applications of environmental biotechnology for a sustainable future*, pp. 13–41, 2017.
- [2] M. Derks and H. Romijn, "Sustainable performance challenges of rural microgrids: Analysis of incentives and policy framework in indonesia," *Energy for Sustainable Development*, vol. 53, pp. 57–70, 2019.
- [3] T. Adefarati and G. Obikoya, "Assessment of renewable energy technologies in a standalone microgrid system," *International Journal of Engineering Research in Africa*, vol. 46, pp. 146–167, 2020.
- [4] G. B. Kumar and K. Palanisamy, "A review of energy storage participation for ancillary services in a microgrid environment," *Inventions*, vol. 5, no. 4, p. 63, 2020.
- [5] C. Wei, Z. Shen, D. Xiao, L. Wang, X. Bai, and H. Chen, "An optimal scheduling strategy for peer-to-peer trading in interconnected microgrids based on ro and nash bargaining," *Applied Energy*, vol. 295, p. 117024, 2021.
- [6] T. L. Hardy, *Software and System Safety*. AuthorHouse, 2012.
- [7] D. U. Case, "Analysis of the cyber attack on the ukrainian power grid," *Electricity information sharing and analysis center (E-ISAC)*, vol. 388, no. 1-29, p. 3, 2016.
- [8] A. Bidram, A. Davoudi, and F. L. Lewis, "A multiobjective distributed control framework for islanded ac microgrids," *IEEE Transactions on Industrial Informatics*, vol. 10, no. 3, pp. 1785–1798, 2014.
- [9] J. Xiao, L. Wang, Z. Qin, and P. Bauer, "An adaptive cyber security scheme for ac micro-grids," in *2022 IEEE Energy Conversion Congress and Exposition (ECCE)*, pp. 1–6, IEEE, 2022.
- [10] O. A. Beg, T. T. Johnson, and A. Davoudi, "Detection of false-data injection attacks in cyber-physical dc microgrids," *IEEE Transactions on Industrial Informatics*, vol. 13, no. 5, pp. 2693–2703, 2017.
- [11] S. Liu, Z. Hu, X. Wang, and L. Wu, "Stochastic stability analysis and control of secondary frequency regulation for islanded microgrids under random denial of service attacks," *IEEE Transactions on Industrial Informatics*, vol. 15, no. 7, pp. 4066–4075, 2019.

- [12] M. Shahidehpour, F. Tinney, and Y. Fu, "Impact of security on power systems operation," *Proceedings of the IEEE*, vol. 93, no. 11, pp. 2013–2025, 2005.
- [13] H. S. Sánchez, D. Rotondo, T. Escobet, V. Puig, and J. Quevedo, "Bibliographical review on cyber attacks from a control oriented perspective," *Annual Reviews in Control*, vol. 48, pp. 103–128, 2019.
- [14] A. Cecilia, S. Sahoo, T. Dragičević, R. Costa-Castelló, and F. Blaabjerg, "On addressing the security and stability issues due to false data injection attacks in dc microgrids—an adaptive observer approach," *IEEE Transactions on Power Electronics*, vol. 37, no. 3, pp. 2801–2814, 2022.
- [15] K. Manandhar, X. Cao, F. Hu, and Y. Liu, "Detection of faults and attacks including false data injection attack in smart grid using kalman filter," *IEEE Transactions on Control of Network Systems*, vol. 1, no. 4, pp. 370–379, 2014.
- [16] J. Xiao, L. Wang, Z. Qin, and P. Bauer, "Detection of cyber attack in smart grid: A comparative study," in *2022 IEEE 20th International Power Electronics and Motion Control Conference (PEMC)*, pp. 48–54, IEEE, 2022.
- [17] J. Zhao, L. Mili, and M. Wang, "A generalized false data injection attacks against power system nonlinear state estimator and countermeasures," *IEEE Transactions on Power Systems*, vol. 33, no. 5, pp. 4868–4877, 2018.
- [18] Y. Jiang, Y. Yang, S.-C. Tan, and S. Y. Hui, "Distributed sliding mode observer-based secondary control for dc microgrids under cyber-attacks," *IEEE Journal on Emerging and Selected Topics in Circuits and Systems*, vol. 11, no. 1, pp. 144–154, 2021.
- [19] M. H. Ranjbar, M. Kheradmandi, and A. Pirayesh, "Assigning operating reserves in power systems under imminent intelligent attack threat," *IEEE Transactions on Power Systems*, vol. 34, no. 4, pp. 2768–2777, 2019.
- [20] Y. Wan and T. Dragičević, "Data-driven cyber-attack detection of intelligent attacks in islanded dc microgrids," *IEEE Transactions on Industrial Electronics*, vol. 70, no. 4, pp. 4293–4299, 2023.
- [21] A. S. Musleh, G. Chen, and Z. Y. Dong, "A survey on the detection algorithms for false data injection attacks in smart grids," *IEEE Transactions on Smart Grid*, vol. 11, no. 3, pp. 2218–2234, 2020.
- [22] L. Che, X. Liu, Z. Li, and Y. Wen, "False data injection attacks induced sequential outages in power systems," *IEEE Transactions on Power Systems*, vol. 34, no. 2, pp. 1513–1523, 2018.
- [23] Q. Zhou, M. Shahidehpour, A. Alabdulwahab, and A. Abusorrah, "Flexible division and unification control strategies for resilience enhancement in networked microgrids," *IEEE Transactions on Power Systems*, vol. 35, no. 1, pp. 474–486, 2020.

- [24] J. Liu, X. Lu, and J. Wang, "Resilience analysis of dc microgrids under denial of service threats," *IEEE Transactions on Power Systems*, vol. 34, no. 4, pp. 3199–3208, 2019.
- [25] J. Liu, Y. Du, S.-i. Yim, X. Lu, B. Chen, and F. Qiu, "Steady-state analysis of microgrid distributed control under denial of service attacks," *IEEE Journal of Emerging and Selected Topics in Power Electronics*, vol. 9, no. 5, pp. 5311–5325, 2021.
- [26] S. Sahoo, T. Dragičević, Y. Yang, and F. Blaabjerg, "Adaptive resilient operation of cooperative grid-forming converters under cyber attacks," in *2020 IEEE CyberPELS (CyberPELS)*, pp. 1–5, 2020.
- [27] W. Yao, Y. Wang, Y. Xu, and C. Deng, "Cyber-resilient control of an islanded microgrid under latency attacks and random dos attacks," *IEEE Transactions on Industrial Informatics*, vol. 19, no. 4, pp. 5858–5869, 2023.
- [28] Q. Zhou, M. Shahidehpour, A. Alabdulwahab, and A. Abusorrah, "A cyber-attack resilient distributed control strategy in islanded microgrids," *IEEE Transactions on Smart Grid*, vol. 11, no. 5, pp. 3690–3701, 2020.
- [29] S. Sahoo, T. Dragičević, and F. Blaabjerg, "An event-driven resilient control strategy for dc microgrids," *IEEE Transactions on Power Electronics*, vol. 35, no. 12, pp. 13714–13724, 2020.
- [30] S. Abhinav, H. Modares, F. L. Lewis, F. Ferrese, and A. Davoudi, "Synchrony in networked microgrids under attacks," *IEEE Transactions on Smart Grid*, vol. 9, no. 6, pp. 6731–6741, 2018.
- [31] S. Sahoo, Y. Yang, and F. Blaabjerg, "Resilient synchronization strategy for ac microgrids under cyber attacks," *IEEE Transactions on Power Electronics*, vol. 36, no. 1, pp. 73–77, 2021.
- [32] Z. Wang, Y. Chen, X. Li, Y. Xu, W. Wu, S. Liao, H. Wang, and S. Cao, "Adaptive harmonic impedance reshaping control strategy based on a consensus algorithm for harmonic sharing and power quality improvement in microgrids with complex feeder networks," *IEEE Transactions on Smart Grid*, vol. 13, no. 1, pp. 47–57, 2022.
- [33] J. W. Simpson-Porco, Q. Shafiee, F. Dörfler, J. C. Vasquez, J. M. Guerrero, and F. Bullo, "Secondary frequency and voltage control of islanded microgrids via distributed averaging," *IEEE Transactions on Industrial Electronics*, vol. 62, no. 11, pp. 7025–7038, 2015.
- [34] C. Deng, Y. Wang, C. Wen, Y. Xu, and P. Lin, "Distributed resilient control for energy storage systems in cyber-physical microgrids," *IEEE Transactions on Industrial Informatics*, vol. 17, no. 2, pp. 1331–1341, 2021.
- [35] J. Xiao, L. Wang, Z. Qin, and P. Bauer, "A resilience enhanced secondary control for ac micro-grids," *IEEE Transactions on Smart Grid*, 2023.

- [36] X. Meng, J. Liu, and Z. Liu, "A generalized droop control for grid-supporting inverter based on comparison between traditional droop control and virtual synchronous generator control," *IEEE Transactions on Power Electronics*, vol. 34, no. 6, pp. 5416–5438, 2019.
- [37] Z. Wang, Y. Chen, X. Li, Y. Xu, C. Luo, Q. Li, and Y. He, "Active power oscillation suppression based on decentralized transient damping control for parallel virtual synchronous generators," *IEEE Transactions on Smart Grid*, vol. 14, no. 4, pp. 2582–2592, 2023.
- [38] H. Liu, Y. Chen, S. Li, and Y. Hou, "Improved droop control of isolated microgrid with virtual impedance," in *2013 IEEE Power & Energy Society General Meeting*, pp. 1–5, 2013.
- [39] K. De Brabandere, B. Bolsens, J. Van den Keybus, A. Woyte, J. Driesen, and R. Belmans, "A voltage and frequency droop control method for parallel inverters," *IEEE Transactions on Power Electronics*, vol. 22, no. 4, pp. 1107–1115, 2007.
- [40] H. Mahmood, D. Michaelson, and J. Jiang, "Accurate reactive power sharing in an islanded microgrid using adaptive virtual impedances," *IEEE Transactions on Power Electronics*, vol. 30, no. 3, pp. 1605–1617, 2015.
- [41] J. Guerrero, L. G. de Vicuna, J. Matas, M. Castilla, and J. Miret, "Output impedance design of parallel-connected ups inverters with wireless load-sharing control," *IEEE Transactions on Industrial Electronics*, vol. 52, no. 4, pp. 1126–1135, 2005.
- [42] J. Xiao, Y. Jia, B. Jia, Z. Li, Y. Pan, and Y. Wang, "An inertial droop control based on comparisons between virtual synchronous generator and droop control in inverter-based distributed generators," *Energy Reports*, vol. 6, pp. 104–112, 2020.
- [43] Z. Qin, L. Wang, and P. Bauer, "Review on power quality issues in ev charging," in *2022 IEEE 20th International Power Electronics and Motion Control Conference (PEMC)*, pp. 360–366, 2022.
- [44] L. Wang, Z. Qin, T. Slangen, P. Bauer, and T. van Wijk, "Grid impact of electric vehicle fast charging stations: Trends, standards, issues and mitigation measures - an overview," *IEEE Open Journal of Power Electronics*, vol. 2, pp. 56–74, 2021.
- [45] P. Sreekumar and V. Khadkikar, "A new virtual harmonic impedance scheme for harmonic power sharing in an islanded microgrid," *IEEE Transactions on Power Delivery*, vol. 31, no. 3, pp. 936–945, 2015.
- [46] Y. Zhu, F. Zhuo, F. Wang, B. Liu, and Y. Zhao, "A wireless load sharing strategy for islanded microgrid based on feeder current sensing," *IEEE Transactions on Power Electronics*, vol. 30, no. 12, pp. 6706–6719, 2015.
- [47] Z. Li, K. W. Chan, J. Hu, and J. M. Guerrero, "Adaptive droop control using adaptive virtual impedance for microgrids with variable pv outputs and load demands," *IEEE Transactions on Industrial Electronics*, vol. 68, no. 10, pp. 9630–9640, 2021.

- [48] J. Chen, L. Wang, L. Diao, H. Du, and Z. Liu, "Distributed auxiliary inverter of urban rail train—load sharing control strategy under complicated operation condition," *IEEE Transactions on Power Electronics*, vol. 31, no. 3, pp. 2518–2529, 2016.
- [49] T. Vandoorn, B. Meersman, J. De Kooning, and L. Vandevelde, "Controllable harmonic current sharing in islanded microgrids: Dg units with programmable resistive behavior toward harmonics," *IEEE Transactions on Power Delivery*, vol. 27, no. 2, pp. 831–841, 2012.
- [50] J. He, Y. W. Li, and M. S. Munir, "A flexible harmonic control approach through voltage-controlled dg-grid interfacing converters," *IEEE Transactions on Industrial Electronics*, vol. 59, no. 1, pp. 444–455, 2012.
- [51] F. Deng, W. Yao, X. Zhang, Y. Tang, and P. Mattavelli, "Review of impedance-reshaping-based power sharing strategies in islanded ac microgrids," *IEEE Transactions on Smart Grid*, vol. 14, no. 3, pp. 1692–1707, 2023.
- [52] E. Hammad, A. Farraj, and D. Kundur, "On cyber-physical coupling and distributed control in smart grids," *IEEE Transactions on Industrial Informatics*, vol. 15, no. 8, pp. 4418–4429, 2019.
- [53] M.-D. Pham and H.-H. Lee, "Effective coordinated virtual impedance control for accurate power sharing in islanded microgrid," *IEEE Transactions on Industrial Electronics*, vol. 68, no. 3, pp. 2279–2288, 2021.
- [54] T. V. Hoang and H.-H. Lee, "Virtual impedance control scheme to compensate for voltage harmonics with accurate harmonic power sharing in islanded microgrids," *IEEE Journal of Emerging and Selected Topics in Power Electronics*, vol. 9, no. 2, pp. 1682–1695, 2021.
- [55] Z. Wang, Y. Chen, X. Li, S. Liao, Y. Xu, W. Wu, H. Wang, and S. Cao, "Impedance-based adaptively reshaping method for enhancing nonlinear load sharing and voltage quality in islanded microgrids with virtual synchronous generator," *IEEE Transactions on Smart Grid*, vol. 13, no. 4, pp. 2568–2578, 2022.
- [56] S. Sahoo and S. Mishra, "A distributed finite-time secondary average voltage regulation and current sharing controller for dc microgrids," *IEEE Transactions on Smart Grid*, vol. 10, no. 1, pp. 282–292, 2017.
- [57] T. Zhao, Z. Li, and Z. Ding, "Consensus-based distributed optimal energy management with less communication in a microgrid," *IEEE Transactions on Industrial Informatics*, vol. 15, no. 6, pp. 3356–3367, 2019.
- [58] T. Yang, S. Sun, and G.-P. Liu, "Distributed discrete-time secondary cooperative control for ac microgrids with communication delays," *IEEE Transactions on Industrial Electronics*, vol. 70, no. 6, pp. 5949–5959, 2023.
- [59] L. Ding, Q.-L. Han, X. Ge, and X.-M. Zhang, "An overview of recent advances in event-triggered consensus of multiagent systems," *IEEE Transactions on Cybernetics*, vol. 48, no. 4, pp. 1110–1123, 2018.

- [60] L. Ding, Q.-L. Han, and X.-M. Zhang, "Distributed secondary control for active power sharing and frequency regulation in islanded microgrids using an event-triggered communication mechanism," *IEEE Transactions on Industrial Informatics*, vol. 15, no. 7, pp. 3910–3922, 2019.
- [61] J. Lu, M. Savaghebi, B. Zhang, X. Hou, Y. Sun, and J. M. Guerrero, "Distributed dynamic event-triggered control for accurate active and harmonic power sharing in modular on-line ups systems," *IEEE Transactions on Industrial Electronics*, vol. 69, no. 12, pp. 13045–13055, 2022.
- [62] C. Bordons, F. Garcia-Torres, M. A. Ridaio, C. Bordons, F. Garcia-Torres, and M. A. Ridaio, "Model predictive control fundamentals," *Model Predictive Control of Microgrids*, pp. 25–44, 2020.
- [63] P. Ge, B. Chen, and F. Teng, "Event-triggered distributed model predictive control for resilient voltage control of an islanded microgrid," *International Journal of Robust and Nonlinear Control*, vol. 31, no. 6, pp. 1979–2000, 2021.
- [64] A. N. F., J. S. Gómez, J. Llanos, E. Rute, D. Sáez, and M. Sumner, "Distributed predictive control strategy for frequency restoration of microgrids considering optimal dispatch," *IEEE Transactions on Smart Grid*, vol. 12, no. 4, pp. 2748–2759, 2021.
- [65] Q. Yang, J. Zhou, X. Chen, and J. Wen, "Distributed mpc-based secondary control for energy storage systems in a dc microgrid," *IEEE Transactions on Power Systems*, vol. 36, no. 6, pp. 5633–5644, 2021.
- [66] E. Rute-Luengo, A. Navas-Fonseca, J. S. Gómez, E. Espina, C. Burgos-Mellado, D. Sáez, M. Sumner, and D. Muñoz-Carpintero, "Distributed model-based predictive secondary control for hybrid ac/dc microgrids," *IEEE Journal of Emerging and Selected Topics in Power Electronics*, vol. 11, no. 1, pp. 627–642, 2023.
- [67] A. Navas-Fonseca, C. Burgos-Mellado, J. S. Gómez, E. Espina, J. Llanos, D. Sáez, M. Sumner, and D. E. Olivares, "Distributed predictive secondary control with soft constraints for optimal dispatch in hybrid ac/dc microgrids," *IEEE Transactions on Smart Grid*, pp. 1–1, 2023.
- [68] Y. Yu, G.-P. Liu, and W. Hu, "Coordinated distributed predictive control for voltage regulation of dc microgrids with communication delays and data loss," *IEEE Transactions on Smart Grid*, vol. 14, no. 3, pp. 1708–1722, 2023.
- [69] G. Lou, W. Gu, Y. Xu, M. Cheng, and W. Liu, "Distributed mpc-based secondary voltage control scheme for autonomous droop-controlled microgrids," *IEEE Transactions on Sustainable Energy*, vol. 8, no. 2, pp. 792–804, 2017.
- [70] X. Chen, H. Yu, and F. Hao, "Prescribed-time event-triggered bipartite consensus of multiagent systems," *IEEE Transactions on Cybernetics*, vol. 52, no. 4, pp. 2589–2598, 2022.

- [71] J. Xiao, L. Wang, Z. Qin, and P. Bauer, "Virtual impedance control for load sharing and bus voltage quality improvement," in *2023 25th European Conference on Power Electronics and Applications (EPE'23 ECCE Europe)*, pp. 1–8, 2023.
- [72] J. Xiao, L. Wang, Z. Qin, and P. Bauer, "An adaptive virtual impedance control for reactive power sharing in microgrids," in *2023 IEEE Energy Conversion Congress and Exposition (ECCE)*, pp. 584–589, 2023.
- [73] J. Xiao, L. Wang, P. Bauer, and Z. Qin, "Virtual impedance control for load sharing and bus voltage quality improvement in low voltage ac microgrid," *IEEE Transactions on Smart Grid*, pp. 1–1, 2023.
- [74] L. B. Larumbe, Z. Qin, L. Wang, and P. Bauer, "Impedance modeling for three-phase inverters with double synchronous reference frame current controller in the presence of imbalance," *IEEE Transactions on Power Electronics*, vol. 37, no. 2, pp. 1461–1475, 2022.
- [75] P. Rodríguez, A. Luna, I. Candela, R. Mujal, R. Teodorescu, and F. Blaabjerg, "Multiresonant frequency-locked loop for grid synchronization of power converters under distorted grid conditions," *IEEE Transactions on Industrial Electronics*, vol. 58, no. 1, pp. 127–138, 2011.
- [76] T. V. Hoang and H.-H. Lee, "Accurate power sharing with harmonic power for islanded multibus microgrids," *IEEE Journal of Emerging and Selected Topics in Power Electronics*, vol. 7, no. 2, pp. 1286–1299, 2019.
- [77] "Ieee standard definitions for the measurement of electric power quantities under sinusoidal, nonsinusoidal, balanced, or unbalanced conditions," *IEEE Std 1459-2010 (Revision of IEEE Std 1459-2000)*, pp. 1–50, 2010.
- [78] W. Yao, M. Chen, J. Matas, J. M. Guerrero, and Z.-M. Qian, "Design and analysis of the droop control method for parallel inverters considering the impact of the complex impedance on the power sharing," *IEEE Transactions on Industrial Electronics*, vol. 58, no. 2, pp. 576–588, 2011.
- [79] "Ieee standard for interconnection and interoperability of distributed energy resources with associated electric power systems interfaces," *IEEE Std 1547-2018 (Revision of IEEE Std 1547-2003)*, pp. 1–138, 2018.
- [80] I. F II, "Ieee recommended practices and requirements for harmonic control in electrical power systems," *New York, NY, USA*, pp. 1–1, 1993.
- [81] V. Nasirian, S. Moayedi, A. Davoudi, and F. L. Lewis, "Distributed cooperative control of dc microgrids," *IEEE Transactions on Power Electronics*, vol. 30, no. 4, pp. 2288–2303, 2015.
- [82] X. Chen, J. Zhou, M. Shi, Y. Chen, and J. Wen, "Distributed resilient control against denial of service attacks in dc microgrids with constant power load," *Renewable and Sustainable Energy Reviews*, vol. 153, p. 111792, 2022.

- [83] C. Kalalas, L. Thrybom, and J. Alonso-Zarate, "Cellular communications for smart grid neighborhood area networks: A survey," *IEEE Access*, vol. 4, pp. 1469–1493, 2016.
- [84] R. Olfati-Saber, J. A. Fax, and R. M. Murray, "Consensus and cooperation in networked multi-agent systems," *Proceedings of the IEEE*, vol. 95, no. 1, pp. 215–233, 2007.
- [85] J. Rocabert, A. Luna, F. Blaabjerg, and P. Rodríguez, "Control of power converters in ac microgrids," *IEEE Transactions on Power Electronics*, vol. 27, no. 11, pp. 4734–4749, 2012.
- [86] G. C. Kryonidis, E. O. Kontis, A. I. Chrysochos, K. O. Oureilidis, C. S. Demoulias, and G. K. Papagiannis, "Power flow of islanded ac microgrids: Revisited," *IEEE Transactions on Smart Grid*, vol. 9, no. 4, pp. 3903–3905, 2018.
- [87] E. D. Coyle and R. A. Simmons, *Understanding the global energy crisis*. Purdue University Press, 2014.
- [88] Q.-C. Zhong, "Virtual synchronous machines: A unified interface for grid integration," *IEEE Power Electronics Magazine*, vol. 3, no. 4, pp. 18–27, 2016.
- [89] J. Fang, H. Li, Y. Tang, and F. Blaabjerg, "Distributed power system virtual inertia implemented by grid-connected power converters," *IEEE Transactions on Power Electronics*, vol. 33, no. 10, pp. 8488–8499, 2018.
- [90] J. Zhu, C. D. Booth, G. P. Adam, A. J. Roscoe, and C. G. Bright, "Inertia emulation control strategy for vsc-hvdc transmission systems," *IEEE Transactions on Power Systems*, vol. 28, no. 2, pp. 1277–1287, 2013.
- [91] J. Fang, R. Zhang, H. Li, and Y. Tang, "Frequency derivative-based inertia enhancement by grid-connected power converters with a frequency-locked-loop," *IEEE Transactions on Smart Grid*, vol. 10, no. 5, pp. 4918–4927, 2019.
- [92] J. Liu, X. Liu, J. Liu, X. Li, and J. Wang, "Adaptive-droop-coefficient vsg control for cost-efficient grid frequency support," *IEEE Transactions on Power Systems*, vol. 39, no. 5, pp. 6768–6771, 2024.
- [93] G. Delille, B. Francois, and G. Malarange, "Dynamic frequency control support by energy storage to reduce the impact of wind and solar generation on isolated power system's inertia," *IEEE Transactions on Sustainable Energy*, vol. 3, no. 4, pp. 931–939, 2012.
- [94] J. O'Sullivan, A. Rogers, D. Flynn, P. Smith, A. Mullane, and M. O'Malley, "Studying the maximum instantaneous non-synchronous generation in an island system—frequency stability challenges in ireland," *IEEE Transactions on Power Systems*, vol. 29, no. 6, pp. 2943–2951, 2014.
- [95] Q.-C. Zhong and G. Weiss, "Synchronverters: Inverters that mimic synchronous generators," *IEEE Transactions on Industrial Electronics*, vol. 58, no. 4, pp. 1259–1267, 2011.

- [96] S. Chen, Y. Sun, H. Han, Z. Luo, G. Shi, L. Yuan, and J. M. Guerrero, "Active power oscillation suppression and dynamic performance improvement for multi-vsg grids based on consensus control via coi frequency," *International Journal of Electrical Power & Energy Systems*, vol. 147, p. 108796, 2023.
- [97] X. Hou, Y. Sun, X. Zhang, J. Lu, P. Wang, and J. M. Guerrero, "Improvement of frequency regulation in vsg-based ac microgrid via adaptive virtual inertia," *IEEE Transactions on Power Electronics*, vol. 35, no. 2, pp. 1589–1602, 2020.
- [98] M. Li, W. Huang, N. Tai, L. Yang, D. Duan, and Z. Ma, "A dual-adaptivity inertia control strategy for virtual synchronous generator," *IEEE Transactions on Power Systems*, vol. 35, no. 1, pp. 594–604, 2020.
- [99] D. Li, Q. Zhu, S. Lin, and X. Y. Bian, "A self-adaptive inertia and damping combination control of vsg to support frequency stability," *IEEE Transactions on Energy Conversion*, vol. 32, no. 1, pp. 397–398, 2017.
- [100] L. Li, Y. Sun, Y. Liu, P. Tian, and S. Shen, "A communication-free adaptive virtual inertia control of cascaded-type vsGs for power oscillation suppression," *International Journal of Electrical Power & Energy Systems*, vol. 149, p. 109034, 2023.
- [101] M. Chen, D. Zhou, and F. Blaabjerg, "Active power oscillation damping based on acceleration control in paralleled virtual synchronous generators system," *IEEE Transactions on Power Electronics*, vol. 36, no. 8, pp. 9501–9510, 2021.
- [102] S. Fu, Y. Sun, L. Li, Z. Liu, H. Han, and M. Su, "Power oscillation suppression in multi-vsg grid by adaptive virtual impedance control," *IEEE Systems Journal*, vol. 16, no. 3, pp. 4744–4755, 2022.
- [103] M. Shi, X. Chen, J. Zhou, Y. Chen, J. Wen, and H. He, "Frequency restoration and oscillation damping of distributed vsGs in microgrid with low bandwidth communication," *IEEE Transactions on Smart Grid*, vol. 12, no. 2, pp. 1011–1021, 2021.
- [104] X. Gao, D. Zhou, A. Anvari-Moghaddam, and F. Blaabjerg, "An adaptive control strategy with a mutual damping term for paralleled virtual synchronous generators system," *Sustainable Energy, Grids and Networks*, vol. 38, p. 101308, 2024.
- [105] Y. Yu, S. K. Chaudhary, G. D. A. Tinajero, L. Xu, J. C. Vasquez, and J. M. Guerrero, "Active damping for dynamic improvement of multiple grid-tied virtual synchronous generators," *IEEE Transactions on Industrial Electronics*, vol. 71, no. 4, pp. 3673–3683, 2024.
- [106] F. Wang, L. Zhang, X. Feng, and H. Guo, "An adaptive control strategy for virtual synchronous generator," *IEEE Transactions on Industry Applications*, vol. 54, no. 5, pp. 5124–5133, 2018.
- [107] S. Dong and Y. C. Chen, "Adjusting synchronverter dynamic response speed via damping correction loop," *IEEE Transactions on Energy Conversion*, vol. 32, no. 2, pp. 608–619, 2017.

- [108] Y. Yu, S. K. Chaudhary, G. D. A. Tinajero, L. Xu, N. N. B. A. Bakar, J. C. Vasquez, and J. M. Guerrero, "A reference-feedforward-based damping method for virtual synchronous generator control," *IEEE Transactions on Power Electronics*, vol. 37, no. 7, pp. 7566–7571, 2022.
- [109] M. Li, P. Yu, W. Hu, Y. Wang, S. Shu, Z. Zhang, and F. Blaabjerg, "Phase feedforward damping control method for virtual synchronous generators," *IEEE Transactions on Power Electronics*, vol. 37, no. 8, pp. 9790–9806, 2022.
- [110] Z. Shuai, W. Huang, Z. J. Shen, A. Luo, and Z. Tian, "Active power oscillation and suppression techniques between two parallel synchronverters during load fluctuations," *IEEE Transactions on Power Electronics*, vol. 35, no. 4, pp. 4127–4142, 2020.
- [111] B. Yang, H. Li, S. Xu, H. Liu, and S. Lu, "Systematic methods to eliminate the transient circulating powers in the multi-vsgs system," *IEEE Transactions on Smart Grid*, vol. 15, no. 1, pp. 179–190, 2024.
- [112] X. Yu and Y. Xue, "Smart grids: A cyber–physical systems perspective," *Proceedings of the IEEE*, vol. 104, no. 5, pp. 1058–1070, 2016.
- [113] D. E. Olivares, A. Mehrizi-Sani, A. H. Etemadi, C. A. Cañizares, R. Iravani, M. Kaz-erani, A. H. Hajimiragha, O. Gomis-Bellmunt, M. Saeedifard, R. Palma-Behnke, G. A. Jiménez-Estévez, and N. D. Hatziargyriou, "Trends in microgrid control," *IEEE Transactions on Smart Grid*, vol. 5, no. 4, pp. 1905–1919, 2014.
- [114] J. Lai, H. Zhou, X. Lu, X. Yu, and W. Hu, "Droop-based distributed cooperative control for microgrids with time-varying delays," *IEEE Transactions on Smart Grid*, vol. 7, no. 4, pp. 1775–1789, 2016.
- [115] G. Lou, W. Gu, X. Lu, Y. Xu, and H. Hong, "Distributed secondary voltage control in islanded microgrids with consideration of communication network and time delays," *IEEE Transactions on Smart Grid*, vol. 11, no. 5, pp. 3702–3715, 2020.
- [116] L. Sheng, G. Lou, W. Gu, S. Lu, S. Ding, and Z. Ye, "Optimal communication network design of microgrids considering cyber-attacks and time-delays," *IEEE Transactions on Smart Grid*, vol. 13, no. 5, pp. 3774–3785, 2022.
- [117] C. Deng, F. Guo, C. Wen, D. Yue, and Y. Wang, "Distributed resilient secondary control for dc microgrids against heterogeneous communication delays and dos attacks," *IEEE Transactions on Industrial Electronics*, vol. 69, no. 11, pp. 11560–11568, 2022.
- [118] J. Duan and M.-Y. Chow, "A resilient consensus-based distributed energy management algorithm against data integrity attacks," *IEEE Transactions on Smart Grid*, vol. 10, no. 5, pp. 4729–4740, 2019.
- [119] H. Wang, Z. Yan, M. Shahidehpour, X. Xu, and Q. Zhou, "Quantitative evaluations of uncertainties in multivariate operations of microgrids," *IEEE Transactions on Smart Grid*, vol. 11, no. 4, pp. 2892–2903, 2020.

- [120] J. Zhang, S. Sahoo, J. C.-H. Peng, and F. Blaabjerg, "Mitigating concurrent false data injection attacks in cooperative dc microgrids," *IEEE Transactions on Power Electronics*, vol. 36, no. 8, pp. 9637–9647, 2021.
- [121] J. Xiao, L. Wang, P. Bauer, and Z. Qin, "Cyber secure-oriented communication network design for microgrids," in *2024 IEEE 15th International Symposium on Power Electronics for Distributed Generation Systems (PEDG)*, pp. 1–6, 2024.
- [122] R. Olfati-Saber and R. Murray, "Consensus problems in networks of agents with switching topology and time-delays," *IEEE Transactions on Automatic Control*, vol. 49, no. 9, pp. 1520–1533, 2004.
- [123] G. Lou, W. Gu, J. Wang, W. Sheng, and L. Sun, "Optimal design for distributed secondary voltage control in islanded microgrids: Communication topology and controller," *IEEE Transactions on Power Systems*, vol. 34, no. 2, pp. 968–981, 2019.
- [124] S. Manaffam, M. Talebi, A. K. Jain, and A. Behal, "Intelligent pinning based cooperative secondary control of distributed generators for microgrid in islanding operation mode," *IEEE Transactions on Power Systems*, vol. 33, no. 2, pp. 1364–1373, 2018.
- [125] Y. Han, K. Zhang, H. Li, E. A. A. Coelho, and J. M. Guerrero, "Mas-based distributed coordinated control and optimization in microgrid and microgrid clusters: A comprehensive overview," *IEEE Transactions on Power Electronics*, vol. 33, no. 8, pp. 6488–6508, 2018.

LIST OF PUBLICATIONS

Journal:

1. **J. Xiao**, L. Wang, Z. Qin and P. Bauer, "A Resilience Enhanced Secondary Control for AC Micro-Grids," IEEE Transactions on Smart Grid, vol. 15, no. 1, pp. 810-820, 2024.
2. **J. Xiao**, L. Wang, P. Bauer and Z. Qin, "A Consensus Algorithm-Based Secondary Control with Low Vulnerability in Microgrids," IEEE Transactions on Industrial Informatics, Early Access, 2024.
3. **J. Xiao**, L. Wang, P. Bauer and Z. Qin, "Virtual Impedance Control for Load Sharing and Bus Voltage Quality Improvement in Low-Voltage AC Microgrid," IEEE Transactions on Smart Grid, vol. 15, no. 3, pp. 2447-2458, 2024.
4. **J. Xiao**, L. Wang, Y. Wan, P. Bauer and Z. Qin, "Distributed Model Predictive Control-Based Secondary Control for Power Regulation in AC Microgrids," IEEE Transactions on Smart Grid, vol. 15, no. 6, pp. 5298-5308, 2024.
5. L. Wang, **J. Xiao**, P. Bauer and Z. Qin, "Analytic Design of an EV Charger Controller for Weak Grid Connection," IEEE Transactions on Industrial Electronics, vol. 71, no. 12, pp. 15268-15279, 2024.
6. **J. Xiao**, L. Wang, P. Bauer and Z. Qin, "Active Power Oscillation in Paralleled VSGs," IEEE Transactions on Power Electronics, under review.
7. **J. Xiao**, L. Wang, P. Bauer and Z. Qin, "Resilience-Oriented Communication Network Design for Secondary Control of Microgrids," IEEE Transactions on Industrial Informatics, under review.

Conference:

1. **J. Xiao**, L. Wang, P. Bauer, and Z. Qin, "Cyber Secure-Oriented Communication Network Design for Microgrids," in 2024 IEEE 15th International Symposium on Power Electronics for Distributed Generation Systems (PEDG), 2024, pp. 1-6.
2. **J. Xiao**, L. Wang, P. Bauer, and Z. Qin, "Distributed Model Predictive Control for Active Power Regulation in AC Microgrids," in 2024 IEEE 10th International Power Electronics and Motion Control Conference (IPEMC2024-ECCE Asia), 2024, pp. 2756-2761.
3. **J. Xiao**, L. Wang, Z. Qin, and P. Bauer, "An Adaptive Virtual Impedance Control for Reactive Power Sharing in Microgrids," in 2023 IEEE Energy Conversion Congress and Exposition (ECCE), 2023, pp. 584-589.
4. **J. Xiao**, L. Wang, Z. Qin, and P. Bauer, "Virtual Impedance Control for Load Sharing and Bus Voltage Quality Improvement," in 2023 25th European Conference on Power Electronics and Applications (EPE'23 ECCE Europe), 2023, pp. 1-8.

5. **J. Xiao**, L. Wang, Z. Qin, and P. Bauer, "An Adaptive Cyber Security Scheme for AC Micro-grids," in 2022 IEEE Energy Conversion Congress and Exposition (ECCE), 2022, pp. 1–6.
6. **J. Xiao**, L. Wang, Z. Qin, and P. Bauer, "Detection of Cyber Attack in Smart Grid: A Comparative Study," in 2022 IEEE 20th International Power Electronics and Motion Control Conference (PEMC), 2022, pp. 48–54.

ACKNOWLEDGMENTS

Achieving this milestone has been a challenging yet rewarding journey, and I am grateful to everyone who supported me along the way. Your encouragement, insightful guidance, and genuine kindness played an essential role in helping me overcome obstacles and reach this significant achievement.

First and foremost, I would like to express my heartfelt gratitude to my promoter, Prof. Bauer, for your invaluable guidance and support throughout my PhD journey. Your wisdom, leadership, and dedication to this field have been a constant source of inspiration. Your trust in me has been instrumental in shaping my research and fostering my personal growth. I am deeply thankful for the opportunities, encouragement, and insights you have so generously provided.

Dear Zian, I want to sincerely thank you for being my supervisor throughout this journey—it has truly been my good fortune. Your guidance and support have been invaluable, from technical skills to shaping my research perspective and life lessons. The way you think and pursue your goals has deeply influenced me and inspired me to keep moving forward. Your encouragement during tough times and your leadership by example has been a source of strength for me. I am truly grateful for everything you have done. To me, you are a role model in both your career and your life.

Thank you, Jianning, Wenli, Gautham, Qobad, and Aditya, for the great lunch and coffee chats. Your insights, creative talk, and support have guided and inspired me to keep learning. I was impressed by your experience, knowledge, and passion for research. The lessons from our time together will always motivate me.

Dear Sharmila, I am grateful for your unwavering kindness and support in addressing kinds of issues. Your remarkable patience, understanding, and efficiency in managing my numerous requests have made a significant difference. Thank you for always being supportive, even amidst your busy schedule. I also want to thank Hitesh, Mladen, Joris, Bart, and Harrie for the experiment problem. Your technical skills, problem-solving abilities, and dedication were invaluable.

If I had not been at TU Delft, my PhD life would definitely not have been as enjoyable, as I would not have had you, my lovely friends, by my side. Lu, I feel lucky to have had you by my side throughout this experience. Thank you for your tacit understanding, for being there when I felt lost in my research, and for all the wonderful memories we've shared in Gaeta, Aalborg, and Nashville. Your support has meant so much to me, and being around you has truly been a source of strength. Zhengzhao, I sincerely wish you success in achieving everything you are striving for—I know you will. And please don't forget to recommend me! Ruijun and Yawen, you're both amazing and bright. I hope your PhD journeys are smooth and rewarding and that you always stay as radiant as you are. Tianming and Yang, thank you for your kindness and for all the memorable conversations. Wishing you both success in all your future endeavors. Yang, thank you again for your care when I was sick in Brasov. Guangyao, I always look forward to your views—they

are so inspiring and thought-provoking. Jundong and Heshi, fitness experts, thank you for the fun and lively chats over lunch and coffee. Fan and Haoyuan, it has been a real pleasure working with you. Thank you for your support and kindness. I hope our efforts lead to the great results we're aiming for. Gangwei, I hope you achieve success in your academic journey. I miss your humorous storytelling. To Sohrab, you are so active, always the very first to answer questions, and you make the group welcoming and warm. Many introverts, including myself, have benefited from your kindness. Miad, your positivity is truly contagious—everyone around you can feel your energy and optimism. It's inspiring, and I wish you all the best in your next chapter. To Faezeh, a kind, delicate girl, I hope you can fix everything to reach your dream life; you deserve it.

I would like to extend my heartfelt thanks to my conference companions—Ibrahim, Rohan, Francesca, Reza, Calvin, and Sachin—traveling together to conferences and summer schools have created lasting memories with all of you. Special thanks to Calvin for the intense, full-throttle driving during our ECCE trip in the U.S. To Sachin, thank you for organizing everything and for your thoughtful care in Italy.

The DCES group has been a big, supportive team where everyone cares for and helps each other. I am genuinely grateful to have been part of this warm and inspiring group. My heartfelt thanks to Hani, Sebastián, Laura, Lyu, Gautam, Joel Felipe, Abdourahim, István, Zichen, Carina, Yongpeng, Koen, Alvaro, Margo, Marco, Farshid, Bagas, Julian, Robin, Manfredo, Leila, Sourabh, Darío, Shibo, Nikos, and Adnan. Each of you has contributed to creating a welcoming and motivating environment. The bonds we formed and the moments we shared—whether through discussions or teamwork—are something I will always treasure.

To Yuqing, your patience, understanding, and support have been the foundation that got me here. You've been by my side through the ups and downs, and I'm so grateful to have you with me.

I could not have completed this journey without the unconditional love and unwavering support of my family. To my mom, dad, and sister: your belief in me, constant encouragement, and countless sacrifices have been the foundation of my success. Your faith in me and endless support have been a source of comfort and motivation throughout this journey. I am forever grateful for everything you have done to help me pursue my dreams. This achievement is as much yours as it is mine.

There are too many people for me to list them all, but I believe that when you see this, you will know that I am expressing my gratitude to you. Your kindness, guidance, and encouragement have left an indelible mark on my life.

Junjie
Delft, Nov 2024